MONSTERS IN THE DARK: SUPERMASSIVE BLACK HOLE MASSES AND AGN FEEDBACK IN THE WISDOM PROJECT

by

Eve Victoria North

A THESIS SUBMITTED TO CARDIFF UNIVERSITY
FOR THE DEGREE OF DOCTOR OF PHILOSOPHY

JULY 2020

Now you understand

Just why my head's not bowed.

I don't shout or jump about

Or have to talk real loud.

When you see me passing,

It ought to make you proud.

I say,

It's in the click of my heels,

The bend of my hair,

the palm of my hand,

The need for my care.

'Cause I'm a woman

Phenomenally.

Phenomenal woman,
That's me.

Maya Angelou

Acknowledgements

Friends dont let friends do stupid things. Alone.

Unknown

How to acknowledge the last eight years? It is definitely a story of friends don't let friends do stupid things, alone, for which I am eternally grateful. This is especially true with Elizabeth, Franziska and Katie, without whom I would not be the woman I am today.

I will start with Team Grand my immediate PhD family. To our team leader and my supervisor Tim Davis who has put up with 4 years of my quiet scatter-brained ways and always supported and encouraged me. Thank you Tim you have allowed me my teenage dream of conducting research on galaxies, been patient when my stressed brain forgot even simple physics and sent me on incredible trips in the name of science. With your guidance I have become a better researcher and more confident person and have achieved things I didn't think I could (a PhD for starters). As a first PhD supervision I think you did grand! To Nikki and James, you brought a lot of laughter, insightful questions and moral support to my PhD. I have loved working with you and better yet being your friend, the grandest trio-in-crime *party blower*. I look forward to watching your continued adventures and I hope Team Grand can reunite for a round of beers soon.

From my first day as an undergraduate, to examining my PhD, Steve Eales has been there with wise guidance and funny stories. Thank you Steve for your supportive tutorials. Also thank you to both Steve and Elias Brinks for making me feel comfortable in my viva and asking great questions.

My PhD has been supported by so many fellow PhD students, post-docs and staff, mostly by sharing cake and rounds of beer. I am so thankful for that. Right from undergraduate I have shared the ups and downs of research with Amber, Dan, Hannah, Jeni and Zoe, 2016 class rocked and I feel humble to be your friend and colleague. To Alex, Andrew M., Connor and Tom W. who also endured the PhD journey with me, thank you all for the shared celebrations and commiserations. I will always cherish your friendship and fondly remember our adventures in research and life. I already miss my office and puzzling with Ali, Ed, Gayathri and Rhys, thank you quiet office! The therapy session that is coffee, cake, special tea and pub was essential to me keeping some form of sanity, special thanks to Andrew H., Dan L., Matt B., Rhiannon*. To the galaxies/AIG post-docs Chris C., Frederico, Matt S., Phil C. and Tom B. thank you for your wisdom, tea and friendship.

The welcome I received from the staff at Cardiff University and their continued loveliness is the reason I have stayed for eight years, thank you I have grown so much in your care. Special mentions to Annabel, Chris N., Dan R., Dave B. W., Egor, Georgina, Glesni, Haley, Jane, Jess, Mattia, Matt G., Mark, Mikako, Nadia, Nic, Nicola H., Nicolas, Paul C., Paul R., Patrick, Phil B., Richard L., Sam, Sarah R., Steve F. and Steve B., you are all wonderful and I thank you for your encouragement. Also to the wonderful people I have met through outreach, Abi, Alice, Becky, Brychan, Dave, Matt A., Sarah and Wendy, I have had so much fun doing various events with you and I thank you for encouraging my confidence. I hope that catches my thanks to everyone in Cardiff.

Further afield I send a massive thank you to the WISDOM team; Iguchi, Kyoko, Liji, Martin, Marc, Mark, Michelle, your advice, expertise and general science enthusiasm was indispensable in my PhD. I can't wait to see what WISDOM does next.

I have never felt alone during my PhD, but found a group of wonderful, kind, like-minded people. I have grown in confidence, happiness and worldy knowledge, and now, maybe, feel ready for the world of work. I must also thank Andy and the Flute and Tankard and Maddie and the Bandeoke Band, my bank account and liver would disagree but I love these establishments and miss them immensely.

To my whole family, but especially Mum, Dad, Nicola and Henry thank you for your unwavering love and support. You have encouraged me to pursue my love of science, soothed my stressed brain and even acted interested in monsters in the dark! I only hope I show my gratitude enough, especially *when* all this education pays off and I am a rich lady.

Caerdydd, diolch yn fawr!

*Not forgetting Adam B., Andy R., Aris, Arjen, Bradley, Cameron, Camilo, Charlie, Chinmay, Danni, Dave Y., Emily, Felix, Freeke, Gerwyn, Gwen, Hame, Iain, Ilaria, Jess W., Kennet, Lottie, Lydia, Max, Michael, Olivia, Ollie L., Paul M., Penny, Peter, Phil W., Rachael S., Rosie, Ruth, Ryan, Sarah J., Sarah B., Seamus, Suzie, Tom A., Tom B., Valeriu, Vassilis, Virginia and Zoltan

ABSTRACT

In this thesis I present high resolution interferometric observations of molecular gas in nearby galaxies, observed as part of the mm-Wave Interferometric Survey of Dark Object Masses (WISDOM) project. I demonstrate the ability of these observations to resolve the kinematics of the molecular gas, and then show what these observations reveal about galaxy evolution.

The molecular gas in galaxies provides the fuel from which stars form, and as such understanding this phase of the interstellar medium is clearly crucial if we wish to understand how galaxies quench as they evolve. Until the recent arrival of (sub-)millimetre interferometers with long baselines we have lacked information on the resolved properties of this gas on small scales in galaxies. As part of this thesis I will show the power of such high resolution observations to reveal some of the processes that drive galaxy evolution. Simulations in particular, have shown that understanding of the regulation of gas reservoirs by active galactic nuclei (AGN) is key to deciphering how galaxies live and evolve. The co-evolution of supermassive black holes (SMBHs) and their host galaxies is also thought to be a crucial process in maturing galaxies. The observations needed to address how SMBH co-evolve with their host galaxies are those of the SMBH mass, which can then be compared to various host galaxy properties (e.g. stellar velocity dispersion or mass). Accordingly the measurement of SMBH masses and the observation of AGN feedback is essential to astrophysics. In this thesis I will detail the molecular gas method for measuring SMBH masses. This method is the the foundation of the WISDOM project, of which I am an active member. I will introduce the aims of the project, the work we do and the additional research we are able to do with the data obtained.

I present Atacama Large Millimeter/sub-millimeter Array (ALMA) ^{12}CO(2–1) emission observations of NGC 0383 at $58 \times 32\,\mathrm{pc}^2$ ($0\farcs18 \times 0\farcs1$) resolution. These observations clearly resolve the Keplerian rise in velocity due to the central SMBH. I use the molecular gas method to measure the SMBH mass as $(4.2 \pm 0.7) \times 10^9\,\mathrm{M}_\odot$. This measurement is

consistent with predictions using the $M_{\mathrm{BH}} - \sigma_*$ relation.

The molecular gas method, and in particular the work of the WISDOM project, is exploring new areas of the parameter space for SMBH masses; for instance low mass galaxies. Using a simulated galaxy I perform a comprehensive test of the observational constraints of the molecular gas method. This leads to a list of recommendations of observational parameters, e.g. inclination of the galaxy or number of channels across the linewidth, for accurate SMBH mass recovery.

As mentioned above, feedback from black holes is thought to be important in quenching galaxies. In the penultimate chapter of this thesis I present high resolution ALMA observations of brightest cluster galaxy NGC 0708. This galaxy was observed with the aim of measuring it's SMBH mass, however the data reveal a high velocity, blue-shifted feature in the molecular gas $0\farcs4$ from the centre of the galaxy. I argue, by considering the geometry and quantitative analysis of the kinetic power, that this is evidence of a jet powered molecular gas outflow. I estimate the mass outflow rate to be $0.82 \pm 0.28\,\mathrm{M_\odot\,yr^{-1}}$ (1σ uncertainty), assuming a CO-to-H_2 conversion factor $\alpha_{\mathrm{CO}} = 0.8\,\mathrm{M_\odot\,(K\ km\,s^{-1})^{-1}\,pc^{-2}}$ and a CO(2–1)/CO(1–0) line ratio of 1. This is evidence for small-scale regulation of a galaxy's gas reservoir by an AGN. NGC 0708 also shows evidence of large-scale cooling flow disruption also by the AGN, making it the second galaxy with evidence of both small- and large-scale AGN feedback.

In summary the work presented in this thesis will aide in the expansion of the SMBH mass sample, and therefore the exploration of the co-evolution of SMBHs and their host galaxies. The work will also help add evidence for the importance of AGN in regulating the growth and quiescence of their host galaxy.

PUBLICATIONS

Because no matter how small an act of kindness or generosity or simple positivity you put out into the world, it will make a difference.

Wonder Woman

FIRST AUTHOR

North, Eve V.; Davis, Timothy A.; Bureau, Martin; Cappellari, Michele; Iguchi, Satoru; Liu, Lijie; Onishi, Kyoko; Sarzi, Marc; Smith, Mark D.; Williams, Thomas G., *WISDOM project – V. Resolving molecular gas in Keplerian rotation around the supermassive black hole in NGC 0383*, MNRAS, Volume 490, Issue 1, November 2019, Pages 319-330, https://doi.org/10.1093/mnras/stz2598

North, Eve V.; Davis, Timothy A.; Bureau, Martin; Cappellari, Michele; Iguchi, Satoru; Liu, Lijie; Onishi, Kyoko; Sarzi, Marc; Smith, Mark D.; Williams, Thomas G., *WISDOM project – VII. Multiscale feedback in the brightest cluster galaxy NGC 0708: evidence for a molecular outflow*, MNRAS submitted

CO-AUTHOR

Davis, Timothy A.; Bureau, Martin; Onishi, Kyoko; van de Voort, Freeke; Cappellari, Michele; Iguchi, Satoru; Liu, Lijie; North, Eve V.; Sarzi, Marc; Smith, Mark D., *WISDOM Project – III. Molecular gas measurement of the supermassive black hole mass in the barred lenticular galaxy NGC 4429*, MNRAS, Volume 473, Issue 3, January 2018, Pages 3818-3834, https://doi.org/10.1093/mnras/stx2600

Smith, Mark D.; Bureau, Martin; Davis, Timothy A.; Cappellari, Michele; Liu, Lijie; North, Eve V.; Onishi, Kyoko; Iguchi, Satoru; Sarzi, Marc, *WISDOM project – IV. A molecular gas dynamical measurement of the supermassive black hole mass in NGC 524, MNRAS*, Volume 485, Issue 3, May 2019, Pages 4359-4374, https://doi.org/10.1093/mnras/stz625

Davis, Timothy A.; Nguyen, Dieu D.; Seth, Anil C.; Greene, Jenny E.; Nyland, Kristina; Barth, Aaron J.; Bureau, Martin; Cappellari, Michele; den Brok, Mark; Iguchi, Satoru; Lelli, Federico; Liu, Lijie; Neumayer, Nadine; North, Eve V.; Onishi, Kyoko; Sarzi, Marc; Smith, Mark D.; Williams, Thomas G., *Revealing the intermediate-mass black hole at the heart of the dwarf galaxy NGC 404 with sub-parsec resolution ALMA observations*, MNRAS accepted, doi:10.1093/mnras/staa1567

Liu, Lijie; Bureau, Martin; Blitz, Leo; Cappellari, Michele; Davis, Timothy A.; Smith, Mark D.; Onishi, Kyoko; North, Eve V.; Iguchi, Satoru; Sarzi, Marc, *WISDOM Project – VI. Giant Molecular Clouds in the Lenticular Galaxy NGC 4429: Effects of Shear and Tidal Forces on Clouds*, MNRAS submitted

Smith, Mark D.; Bureau, Martin; Davis, Timothy A.; Cappellari, Michele; Liu, Lijie; Onishi, Kyoko; Iguchi, Satoru; North, Eve V.; Sarzi, Marc, *WISDOM project – VII. Exploring the relation between supermassive black hole mass and galaxy rotation with molecular gas*, MNRAS submitted

Smith, Mark D.; Bureau, Martin; Davis, Timothy A.; Cappellari, Michele; Liu, Lijie; Onishi, Kyoko; Iguchi, Satoru; North, Eve V.; Sarzi, Marc; Williams, Thomas G., *WISDOM project – VIII. Molecular gas measurement of the supermassive black hole mass in the elliptical galaxy NGC 7052*, MNRAS submitted

CONTENTS

Acknowledgements **v**

Abstract **vii**

Publications **ix**

List of Tables **xiv**

List of Figures **xvi**

1 Introduction **1**

1.1 Galaxy evolution 2

1.1.1 Morphological transformation 4

1.2 The interstellar medium 7

1.2.1 Observing molecular gas 9

1.3 SMBH-galaxy co-evolution 12

1.4 Measuring SMBH masses 17

2 The WISDOM project **21**

2.1 Figure of merit 24

2.1.1 Velocity error 25

2.1.2 Figure of merit predictions 25

2.2 Target selection 26

2.2.1 Observing strategy 29

2.2.2 Analysis tools 30

2.3 More than SMBH masses 32

3 SMBH mass measurement in NGC 0383 **37**
3.1 Introduction 37
3.2 Target: NGC 0383 39
3.2.1 ALMA observations 40
3.2.2 Line emission 42
3.2.3 Continuum emission 46
3.3 Dynamical modelling 47
3.3.1 Mass model 48
3.3.2 Bayesian analysis 50
3.4 Discussion 52
3.4.1 Uncertainties 52
3.4.2 Mass-to-light ratio influence 55
3.4.3 Estimating M_{BH} from the observed R_{SOI} 57
3.4.4 Comparison to the literature 57
3.4.5 Comparison of spatial scales probed by molecular gas and mega-masers 59
3.5 Conclusions 62

4 Simulated WISDOM **63**
4.1 Introduction 63
4.2 Simulation and methods 64
4.2.1 Simulation 66
4.2.2 Creating simulated data 67
4.2.3 Method of MCMC analysis 68
4.3 Results and discussion 70
4.3.1 Inclination 71
4.3.2 Beam size 72
4.3.3 Channel width 74
4.3.4 Signal to noise ratio 77
4.3.5 Surface brightness modelling 78
4.3.6 Repeated fitting 78
4.4 Conclusions 79

5 Evidence for AGN feedback in NGC 0708 **81**

5.1 Introduction 81

5.2 Observations 86

5.2.1 ALMA observations 86

5.2.2 e-MERLIN 5 GHz continuum emission 88

5.3 Results 93

5.3.1 Blue-shifted feature properties 95

5.3.2 SMBH mass 98

5.4 Discussion 99

5.4.1 Kinetic power comparison 101

5.4.2 Comparison with other molecular outflows 103

5.4.3 Comparison with ULIRG outflows 104

5.5 Conclusions 110

6 Conclusion **111**

6.1 Key result 1: The ALMA era 112

6.2 Key result 2: SMBH masses across $M_{\mathrm{BH}} - \sigma_*$ 113

6.3 Key result 3: SMBHs role in galaxy evolution 115

6.4 Future work 117

6.4.1 Matching maser SMBH mass accuracy 117

6.4.2 Further investigation of the outflow in NGC 0708 117

6.4.3 Further expansion of the SMBH mass sample 118

6.4.4 Expanding the ETG GMC catalogue 118

6.4.5 Determining α_{CO} in ETGs 119

6.5 Final remarks 119

Bibliography **120**

List of Tables

3.1 NGC 0383 MGE best-fitting Gaussians 50
3.2 Best-fitting paramters from the NGC 0383 MCMC fit 52

4.1 Simulated galaxy intial conditions 67
4.2 Ranges of observational parameters investigated 68
4.3 MCMC variables for the simulated galaxy 70

5.1 NGC 0708 outflow properties 98

List of Figures

1.1 The Hubble tuning fork . . . 3
1.2 Benson et al. (2003) luminosity function . . . 14
1.3 Bower et al. (2012) stellar mass function . . . 15
1.4 $M_{\mathrm{BH}} - M_{\mathrm{bulge}}$ and $M_{\mathrm{BH}} - \sigma_*$ relations . . . 17

2.1 Example CO kinematic models and data . . . 23
2.2 Figure of merit predictions of minimum detectable SMBH mass . . . 27
2.3 Examples of WISDOM project observations . . . 31
2.4 Example of gas flow observations . . . 33

3.1 NGC 0383 Hubble and ALMA imaging . . . 41
3.2 NGC 0383 moment maps . . . 43
3.3 NGC 0383 position velocity diagram . . . 44
3.4 NGC 0383 ^{12}CO(2–1) integrated spectrum . . . 45
3.5 NGC 0383 spectral energy distribution . . . 47
3.6 NGC 0383 stellar mass model . . . 49
3.7 NGC 0383 likelihood plots . . . 53
3.8 NGC 0383 model position velocity diagrams . . . 54
3.9 NGC 0383 moment 1 data minus model residiuals . . . 56
3.10 NGC 0383 radial mass profile . . . 58
3.11 $M_{\mathrm{BH}} - \sigma_*$ relation . . . 60

4.1 Simulated galaxy moment maps . . . 69
4.2 Simulated galaxy position velocity diagram . . . 69
4.3 Inclination variation SMBH recovery . . . 73
4.4 Beam variation SMBH recovery . . . 75
4.5 Channel width variation SMBH recovery . . . 76

4.6 Signal-to-noise ration variation SMBH recovery 77

5.1 NGC 0708 Hubble and ALMA imaging 85
5.2 NGC 0708 moment maps 89
5.3 NGC 0708 position velocity diagram 90
5.4 NGC 0708 integrated spectrum 91
5.5 NGC 0708 moment two map, with 236 GHzcontinuum imaging and the intgrated spectrum of the outflow area 92
5.6 Molecular gas fraction of inflows 100
5.7 Comparison of ULIRG and NGC 0708 outflow mass rates and depletion times 107
5.8 Comparison of ULIRG and NGC 0708 outflow kinetic powers 108
5.9 Comparison of ULIRG and NGC 0708 outflow momentum rates 109

6.1 $M_{\rm BH}-\sigma_{*}$ and $M_{\rm BH}-M_{\rm bulge}$ relations 116

Chapter 1
Introduction

All my life through, the new sights of Nature made me rejoice like a child.

Marie Curie

Galaxies are probably the most easily recognisable cosmic structure. Renowned for their beauty, galaxies captured the imagination despite appearing as unchanging in our short lifetimes. Although initially observed as islands of stars, criss-crossed with dust we now know them to also contain exotic objects for instance black holes and dark matter. Now attention has turned to the function that each component of the galaxy plays in the evolution of its host. Disentangling how this cause and effect manifests is still largely unknown and an area of active investigation.

Of particular importance is the life cycle of gas within galaxies, as the amount of cool gas dictates how many stars can form. How this cycle links to the relatively small but powerful supermassive black hole (SMBH), found near the centre of nearly all galaxies, is becoming an important area of astrophysics. This thesis aims to investigate the black hole's role in its host galaxy's evolution by accurately measuring SMBH masses in a diverse range of galaxies. I will also put forward evidence for feedback on gas within a galaxy by a SMBH.

In Chapter 2 I will introduce the mm-Wave Interferometric Survey of Dark Object Masses (WISDOM) project and give some background on our work. I will also highlight some of the tools developed for the project and work beyond the original aims. In Chapter 3 I will demonstrate the molecular gas method for measuring SMBH masses by estimating the mass of the SMBH at the centre of NGC 0383, (as I presented in North et al. 2019). Then in Chapter 4 I present work using a simulated galaxy of known parameters to assess and demonstrate the ability of the WISDOM project's analysis to recover the correct SMBH mass.

Chapter 5 then moves on to look at the effect of the SMBH on the gas within a galaxy by presenting evidence for Active Galactic Nuclei (AGN) feedback in NGC 0708. Finally in Chapter 6 I will summarise, conclude and explore potential future extensions of my work. Each chapter has its own specific introduction; here I will introduce the physics of galaxy evolution as it pertains to the co-evolution (or not) of SMBHs and their host galaxies.

1.1 GALAXY EVOLUTION

Defined as a gravitationally bound system of gas, dust, stars, dark matter and stellar remnants galaxies are the most well-known structure in the universe. Galaxy's have many observable features, most simply their shape, brightness and dust features. Further to these a galaxy's colour, mass, star formation rate and stellar velocity dispersion give insight into the conditions within the galaxy and to the physics governing it all. For instance colour can be used to infer the age of stars and therefore the age of the galaxy, or a high stellar velocity dispersion can imply a history of mergers.

It was Hubble who most famously divided galaxies into two main classifications, those dominated by spiral structures and those more elliptical in shape (Hubble, 1926). This classification uses only the optical shape or morphology of a galaxy (namely the stars) to group and so infer its properties. Around this time it was commonly thought that the evolutionary sequence of galaxies was for elliptical galaxies to collapse into spiral discs (Hubble, 1926).

The theory has since been revised and reversed, so blue disc, dusty star forming galaxies merge and quench to become elliptical and red. This hierarchical merging has created the universe we see today, the largest structures of clusters and superclusters are still forming via this process (Rees & Ostriker 1977; White & Rees 1978). Hierarchical merging is a product of the Λ-Cold Dark Matter (Λ-CDM) cosmology, and currently the best predictor of the observations we have (e.g White & Frenk 1991; Lacey & Silk 1991; Lacey & Cole 1993; Cole et al. 2000; Benson et al. 2003). The main ideas about galaxy evolution stem from their morphology and colour, which have been used to classify and group galaxies and hence disentangle their story. This classification system is determined at current time (i.e. z=0) but often extrapolated and used at higher redshifts. Galaxies classified by morphology distinguish by the dominance of the bulge over the disc, and then whether that disc has spiral arms and/or a bar. The Hubble tuning fork, Fig. 1.1 (Hubble 1926), shows this classification system.

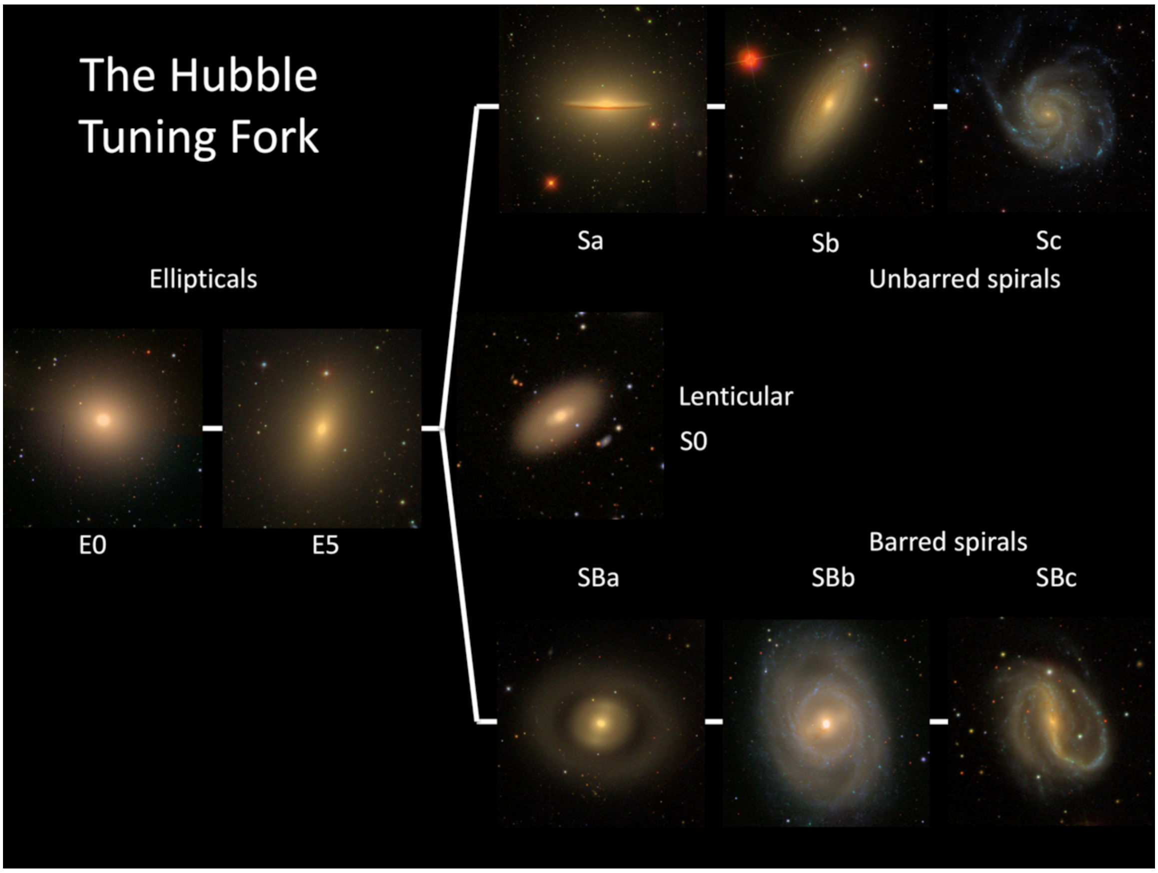

Figure 1.1. Reproduced from Masters et al. (2019): The Hubble tuning fork illustrated with examples suggested by Hubble (1926) with images by the Sloan Digital Sky Survey (York et al., 2000).

Galaxies lacking a stellar disc are called Ellipticals whose ‘only claim to structure is that the luminosity fades smoothly from bright nuclei to indefinite edges’ (Hubble, 1926). Elliptical (‘E’) classification numbers range from 0, completely round, to 7, the most elongated. They sit in the handle of the Hubble tuning fork, on the left of Fig. 1.1. Lenticulars, or ‘S0s’, are the intermediate shaped galaxy with an ellipsoidal, disc shape but no spiral arms. S0s sit at the base of the handle of the Hubble tuning fork, as the middle point between ellipsoidal and disc galaxies. Together these two classes are called ‘early-type’ galaxies (ETGs) whose name harks from early 20th century theories of galaxy evolution. They tend to have old stellar populations, little gas or dust and very low star formation rates.

Those galaxies with spiral arms are classified by the presence of a nuclear bar, with those having such a structure denoted by the letter ‘SB’ and those without by ‘S’. The two classes form the prongs of the Hubble tuning fork, Fig. 1.1. They are further classified by the relative size of the nuclear region, the tightness of the spiral arm wind and how clumpy the spiral arms are. ‘a’ or ‘early-type’ spirals have a large bulge and tightly wound, smooth spiral arms. ‘b’ spirals are the intermediate with a smaller nuclear region and more open arms. ‘c’ or ‘late-type’ spirals are the other extreme of very small nuclei and dominating flocculent spiral arms. ‘Irregular’ are those galaxies that do not fit in the above classification system; they lack both dominant nuclei and rotational symmetry. Together with spiral galaxies, irregulars are labelled ‘late-type’ galaxies (LTGs).

Both sets of galaxies (ETGs and LTGs) appear to follow different evolutionary pathways as evidenced by there residence in particular environments, having certain properties and following specific relations. The history of a galaxy can be interpreted from its environment, the scars of hierarchical merging and from its properties for instance stellar population, gas mass and stellar velocity dispersion.

1.1.1 MORPHOLOGICAL TRANSFORMATION

The colour of a galaxy is often used as a diagnostic for how evolved it is, younger stellar populations tend to be bluer as the large, blue stars have not yet evolved to (super-) red giants or died. Older stellar populations tend to be redder as they contain the smaller stars (which are more yellow/red in colour) and red giants, thus whether a galaxy is star forming or not can be roughly determined by its colour. It has long been observed that there is a bimodal distribution in the colour of galaxies, the ETGs being redder than LTGs (e.g. Baum 1959; Strateva et al. 2001; Bell et al. 2004). ETGs have been shown to be redder both at current times (Schweizer & Seitzer, 1992) and out to redshift $z \approx 1$ (Kodama et al., 1999), implying they have not been forming new stars for quite some time. Whereas the bluer LTGs have ongoing star formation. This inference implies something has happened to or in ETGs to turn off or stop star formation (e.g. Martig et al. 2009).

The evidence further suggests that this is an evolutionary path where LTGs merge and stop star formation to become ETGs in a process known as hierarchical merging, as mentioned earlier this is a result of Λ-CDM cosmology (e.g. Steinmetz & Navarro, 2002). Bell et al. (2004) find a bimodal colour distribution of galaxies out to $z \approx 1$. They find that at fixed magnitude the blue star-forming peak has colours that become redder with decreasing redshift (i.e. towards present day) with more luminous blue galaxies at $z \gtrsim 0.5$. This is as a consequence of both declining star formation rates, and increasing metallicity. They find the quantitative size of this change is consistent with the passive ageing of ancient stellar populations to the present time (Bell et al., 2004). Following on from this they estimated the B-band luminosity function and density of red galaxies in the interval $0 < z \lesssim 1.1$ and found a mild evolution in the B-band luminosity density. During this time an ancient stellar population would have faded by a factor of 2-3, therefore the evolution reveals an increase in the stellar mass of red galaxies since $z \approx 1$, consistent with that expected from hierarchical merging in Λ-CDM cosmology (Bell et al., 2004). Many factors point to hierarchical merging as the assembly method of the universe however, interpreting what is driving this change is more difficult (e.g. Bekki et al. 2002; Steinmetz & Navarro 2002; Laurikainen et al. 2010; Kormendy & Bender 2012).

Environment is often seen as as a big influencer on galaxy evolution, in particular being in or entering into a cluster appears to have a a huge influence on the gas within a galaxy (Gunn & Gott, 1972). Ram pressure stripping and galaxy-galaxy harassment strip gas from a galaxy but can, also, initially compact it causing a burst of star formation (e.g. Moore et al. 1996; Zabel et al. 2019). It has been found that the number of ETGs increases with galaxy density, i.e. within galaxy clusters (e.g. Gunn & Gott 1972; Oemler 1974; Dressler 1980; Haynes et al. 1984; Djorgovski & Davis 1987; Kauffmann et al. 2004; Paulino-Afonso et al. 2019). This indicates the cluster environment may be a leading factor in transforming LTGs to ETGs. The morphology-density relation between ETGs and clusters is still being deciphered, with stellar mass, galaxy size and quenching fraction being found to be important (Paulino-Afonso et al., 2019). The environment appears to have a varying effect on galaxies of different mass, for instance Kauffmann et al. (2004) find that for galaxies of stellar mass $10^{10} - 3 \times 10^{10}$ M$_\odot$ environment can change the specific star formation rate (star formation rate divided by the stellar mass, SFR/M$_*$) by up to a factor of 10, with more active galaxies in low density and inactive ones usually at high density. However they find no evidence for star formation history depending on environment more than 1 Mpc away from a galaxy (Kauffmann et al., 2004), indicating environment may be limited in its affect.

Despite the potential for destruction clusters can also bring gas to a galaxy, in particular the most massive, more central galaxies in clusters (Brightest Cluster Galaxies, BCGs) have potentially huge sources of gas. Groups and clusters are observed to have haloes of hot ($10^7 - 10^8$ K) gas, which is cooling by emission of Bremsstrahlung radiation. When this gas cools it will contract, increasing it's cooling and so its contraction, slowly inflowing towards the central galaxy and eventually being deposited on to it. The cooling rates observed are $10-1000\,\mathrm{M_\odot\,yr^{-1}}$, implying the BCGs in such clusters should be much bluer and brighter than they are. This conundrum, of what happens to the cooled gas, is know as the 'cooling flow problem' (see review Fabian 1994). A solution has been observed, and successfully simulated, in the form of mechanical feedback from AGN. AGN produce radiative winds and relativistic jets which appear to influence and heat the gas at large scales, slowing the cooling flow (e.g. McNamara et al. 2005; McNamara & Nulsen 2007, 2012; Clarke et al. 2009). This feedback appears to keep the ISM of the BCG relatively stable, The importance of AGN in the regulation of gas in BCGs and large ETGs is still being understood, it puts SMBHs as an important part of galaxy evolution. I discuss more on gas regulation by AGN in Chapter 5 where evidence is presented of AGN feedback in the BCG NCG 0708.

The quenching of galaxies by secular (internal) processes, for instance fuel exhaustion, is another candidate for the evolution of galaxies. Secular evolution tends to be slow and driven by instabilities caused by structures within the galaxy (e.g. bars) or galactic winds (and fountains; Kormendy & Kennicutt 2004). The gravitational resonances and instabilities caused by spiral structure and bars transfer angular momentum causing gas flows and the disruption of stellar orbits. In particular bars are often seen to both move gas inwards providing fuel for starbursts and AGN, and to diffuse stars into the bulge (e.g. Pfenniger & Norman 1990; Combes 2001; Kormendy & Kennicutt 2004). This activity reduces the fuel available for star formation in the disc of a LTG and moves it to an earlier-type of galaxy.

It has been observed that near the centre of all galaxies lies a SMBH; 'look into the heart of almost any galaxy and there you will find a monster'*. If the SMBH is consistently fuelled it can become an AGN which are extremely powerful sources of radiation and kinetic energy and appear to be a driver of morphological transformation. AGN produce intense fluxes of photons and particles known as AGN winds which can sweep up gas removing it from the galactic nucleus and sometimes out of the galaxy. The complex magnetic fields of SMBHs can also accelerate charged particles to relativistic speeds in very collimated jets, these can directly impact gas and move it outwards but also inflate bubbles of relativistic plasma. By these means the gas in the centre of a galaxy can be

*Dan Gifford `https://astrobites.org/2011/05/31/black-holes-and-dark-halos-growing-together/`

efficiently stripped and pushed out of the galaxy, thereby stalling its star formation. This process also removes the fuel for said AGN activity indicating there may be a cyclical nature to this process (see e.g. review by Fabian 2012). King & Pounds (2015) find that many small-scale phenomena are explained by AGN wind, for instance quiescence in AGN hosts. Thus the presence of gas in a galaxy also fuels its removal from said galaxy.

The effects of environment, AGN and internal kinematics on a galaxy's interstellar medium (star formation fuel), and therefore morphological type, work on different timescales and appear to be more important for certain morphological types (e.g. Steinmetz & Navarro 2002). Observations of the ISM are therefore important in determining the mechanisms of such transformations.

1.2 THE INTERSTELLAR MEDIUM

The gas and dust within galaxies forms the interstellar medium (ISM), from this stars and planets form. The ISM is replenished by stellar winds, supernovae, galactic fountains and extra-galactic sources such as mergers and accretion of the intergalactic medium. The ISM has a multitude of densities and temperatures and was divided into three 'phases' by McKee & Ostriker (1977), however this is a simplified treatment and does in fact name four phases.

The most pervasive phase is collision-ionised, hot and of low-density (the hot ionised medium; HIM) formed from energetic processes, e.g. accretion shocks and supernova explosions with a filling factor of 0.7–0.8. The HIM is mostly homogeneous with typical temperatures of $\approx 10^6\,$K and densities of $\approx 3.2 \times 10^{-3}\,\mathrm{cm}^{-3}$ (McKee & Ostriker, 1977). The neutral phase, composed mostly of hydrogen atoms (H I) is formed of two temperature regimes; one cold, dense and stable (the cold neutral medium; CNM) and the other warm, less dense and unstable (the warm neutral medium; WNM). The CNM is found in clumps of internal density $\approx 40\,\mathrm{cm}^{-3}$ at a temperature of $\approx 80\,$K. It is optically thin and extends to $\approx 100\,$pc scale height, with a filling factor of 0.02-0.04 (McKee & Ostriker, 1977; Wolfire et al., 2003). The WNM surrounds these clumps, and blends into a partially ionised corona within the galaxy, it has average densities of $\approx 0.3\,\mathrm{cm}^{-3}$ and temperatures of $\approx 8000\,$K and extends to a scale height of $\approx 250\,$pc. The neutral hydrogen is optically thin to the 21 cm emission due to rotational transitions but does have a fractional ionisation of ≈ 0.1 percent due to very soft X-rays from supernova. The warm neutral component is often not counted as a separate medium as it is the transition between neutral and photo-ionised hydrogen (McKee & Ostriker, 1977; Wolfire et al., 2003). The warm medium (both neutral and ionised) fills a larger volume than the CNM but contains far less mass, having a filling factor of 0.2 percent. It is mostly ionised by hot stars (the warm ionised medium;

WIM) and has average temperatures of $\approx 8000\,\mathrm{K}$, densities of about $\approx 0.1-1\,\mathrm{cm}^{-3}$ and a fractional ionisation of ≈ 0.7 (McKee & Ostriker 1977; Cox 2005). These components of the ISM are in general in pressure equilibrium with material switching between the phases relatively quickly, within less than 10^6 years. The CNM clouds and WNM evaporate, are photo- and shock-ionised and thermal instabilities cool hot gas to keep this equilibrium (McKee & Ostriker, 1977).

The ISM also has a fifth phase, that is a colder denser component of the CNM dark clouds (Cox, 2005). Within these dark clouds, shielded from the interstellar radiation, molecules can form and exist; most abundant are hydrogen (H_2) and carbon monoxide (^{12}CO). Temperatures can reduce to $\lessapprox 15\,\mathrm{K}$ and the density is at least several hundred $H_2\,\mathrm{cm}^{-3}$ (Young & Scoville 1991; Scoville & Sanders 1987; Cox 2005). All phases of the ISM have clumpy fractal structures (with more structure revealed with every increase in resolution), further to this the internal motions of the clouds are supersonic and show filamentary structure, indicative of inhomogeneous, turbulent motion (Larson, 1981). The interpretation of cloud kinematics, in terms of determining the dominant form of motion, is a subject of great debate.

It is this very cold, dense phase of the ISM that this thesis is most interested in, as the site for star formation these clouds are of great interest to the astronomy community at large. In particular I focus on cold gas in ETGs, initial observations indicated that ETGs lack gas, in particular the cold, star-forming kind (Lees et al., 1991). Despite apparently lacking gas ETGs do have multiple sources of gas, including AGB stars, supernova and mergers. As they tend to be massive a lot of energy is required to eject gas from them. All galaxies, in relation to their size, are surrounded by a halo of hot (10^7 K) gas which cools via Bremsstrahlung radiation (mainly in the X-ray). As this gas cools it contracts inwards and is deposited on to the galaxy. It should be noted this is a smaller scale version of the cooling flow phenomenon in clusters. This accretion, as well as the internal sources of gas, should give ETGs plenty of gas for star formation. ETGs have since been found to have large hot gas reservoirs (O'Sullivan et al., 2001), especially in dense environments (i.e. in clusters), indicating some mechanism must be preventing the cooling of gas in ETGs. The lower cool gas mass could also indicate some mechanism in the formation of or within ETGs that is not replenishing or is removing that cold gas.

More recent surveys of ETGs using more sensitive detectors have found that they do contain significant gas reservoirs (e.g. Wiklind & Henkel 1989; Knapp & Rupen 1996; Oosterloo et al. 2010; Young et al. 2011; Davis et al. 2019). Oosterloo et al. (2010) detect HI in $\sim 2/3$ of field ETGs and < 10 percent of Virgo cluster objects. Whilst Young et al. (2011) show that at least 22 percent of ETGs contain molecular gas by searching for CO(1–0) and CO(2–1) in a volume limited survey of ETGs (for survey details see ATLAS^{3D};

Cappellari et al. 2011). They find a strong correlation between detection in CO and the presence of dust, blue features, and young stellar ages indicating the gas observed is often engaged in star formation (Young et al., 2011). Further to this a representative sample from the MASSIVE survey (see Ma et al. 2014 for full survey) found a detection rate of ≈ 25 percent for the most massive galaxies within 108 Mpc (Davis et al., 2019).

Also as part of the ATLAS^{3D} survey Davis et al. (2013a) made interferometric ^{12}CO observations and found that the molecular gas extent in ETGs is similar to that of LTGs when scaled by the stellar extent. In their study the surface brightness profiles of the molecular gas followed the stellar light profile in roughly half the ETGs, indicating a lack of recent mergers due to the relaxed gas at large radii. Davis et al. (2013a) also found that mainly low mass galaxies, often in a cluster environment have disturbed, sometimes truncated molecular gas profiles indicating recent mergers or the effect of the hot intra-cluster medium (ICM). In ≈ 70 percent of their ETGs Davis et al. (2013a) found the molecular gas to extend beyond the turnover of the circular velocity curve observed through stellar kinematics. Molecular gas is mostly found to be dynamically cold, to match predications from the circular velocity curve and therefore to be a better direct tracer of the circular velocity compared to ionised gas (Davis et al., 2011, 2013a).

It was also found that there is a marginal drop (1σ effect) in the CO detection in clusters (Young et al., 2011). Further to this, Davis et al. (2019) found the molecular gas to stellar mass fractions of isolated objects are ≈ 0.6 dex higher on average than satellite and BCGs. Clusters are expected to remove gas from galaxies, with e.g. ram pressure stripping, starvation and harassment (e.g. Gunn & Gott 1972; Haynes et al. 1984; Moore et al. 1996; Zabel et al. 2019).

These more recent findings of gas in ETGs complicates the hierarchical evolution of the galaxies, they are not as inactive as initial observations suggested. Further observations are required to fully understand the processes involved.

1.2.1 OBSERVING MOLECULAR GAS

As the most abundant molecule it would be ideal to directly observe H_2 to determine the mass and kinematics of the molecular gas, however as a symmetric molecule it has no permanent electric dipole. The lowest quadrupole rotational transition of H_2 is in the infrared but requires excitation temperatures above those usually found in molecular gas clouds so only traces a vary small fraction of the gas. Astronomers hence turned to the second most abundant molecule, ^{12}CO which has rotational transitions at millimeter wavelengths. By observing ^{12}CO line emission both spatial and kinematic information is collected and as shown by e.g. Wiklind & Henkel (1989); Wrobel & Kenney (1992); Young et al. (2008); Crocker et al. (2009); Davis et al. (2011, 2013a); Ramakrishnan et al. (2019) CO is an excellent tracer of the kinematics of cold gas and the gravitational potential of the galaxy as a whole. Low-J transitions of ^{12}CO were chosen as they are observable with ALMA at many redshifts. The emission lines from e.g. HCN and HCO^+ have transitions at similar frequencies but are normally thought as high density gas tracers which tends to be strongly centrally concentrated indicating they won't be able to trace the gravitational potential out to $V_{\rm flat}$, i.e. the rotational velocity due to the stellar potential, which CO does trace (e.g. Gao & Solomon 2004; Davis et al. (2011)). HCN and HCO^+ are also typically tens times fainter than CO so require high sensitivity observations.

Molecular gas emission lines can be observed from the ground, both by single dish mm-telescopes, and using interferometric techniques. Due to the low frequency, the spatial resolution provided by even the largest single dish telescopes is only $\sim 20''$ (e.g. $22''$ for the 30 m IRAM dish at the frequency of ^{12}CO(1–0), 115 GHz). In this thesis we thus use interferometry to probe in detail the spatial distribution of gas in the centre of galaxies.

Interferometers operate by combining the signal received at two or more physically separated antenna, the signals are interfered giving a sample of the sky brightness distribution. Each measurement of the source signal, with each set of two antenna, is called a visibility. These contain the brightness of emission on those scales that that visibility is sensitive to in the amplitude of the sinusoid observed, and the relative position of that brightness on the sky in the phase of the sinusoid observed. By observing with a variety of differently spaced antenna a range of angular scales can be observed. For a single dish the resolution is defined as $\theta = \lambda/D$ where D is the diameter of the dish and λ is the wavelength of observation. For an interferometer the distance between the dishes (baseline, d) replaces D in that equation. The longest baseline ($d_{\rm max}$) defines the smallest angular scale resolved by the observations. At the other end of the scale, the dishes cannot be infinitely close together and hence there is a largest angular scale that they detect as the visibilities do not cover such scales. This largest angular scale is calculated as $\approx \lambda/d_{\rm min}$, where $d_{\rm min}$ is the smallest baseline. Emission on scales larger than this will be resolved out, which can lead to low flux being received, compared to single dish observations.

These visibilities are calibrated to correct for weather, imperfect receivers and electronic noise. In the most extreme cases bad time periods or antennas can be flagged and removed completely from the process. Constant monitoring of e.g. receiver temperature and atmospheric water vapour content can also be used to correct the visibilities or, if required, remove them. An antenna close to the centre of the array, with a steady response is used as a correction reference for the other antenna and is used as the zero for phase calculations. Cross-calibration can then be applied, this uses observations of bright point sources close to the science target which have known or easily predicted visibilities. The calibration solutions of such objects can be found quickly and extrapolated onto science target observations. For instance observations of known sources of constant radio flux, e.g. quasars or planets, can be used to scale the relative flux density of the science target observed to the absolute value.

These calibrated visibilities are then Fourier transformed from the *uv*-plane to the image, this is the dirty image and still contains the interference pattern due to observing with discrete receivers. To remove this the image must be cleaned. An important part of cleaning is weighting the visibilities to determine how important they are during the transformation. If the visibilities are weighted based on their noise properties, such that short baselines are typically given higher weightings, this is known as natural weighting. The signal-to-noise ratio is maximised however the beam size can be inflated as this weighting can over use visibilities in dense regions of the *uv*-plane. By giving more weight to those visibilities in sparser regions of the *uv*-plane the sensitivity is reduced but the angular resolution is increased, this is called uniform weighting. The scale in between these two was developed by Briggs (1995), with uniform at -2 and natural at 2. Finding the optimal weighting value depends on the source and scientific aims. Another important part of cleaning is the clean algorithm, this determines how the synthesised beam is calculated and therefore the point spread function used when cleaning which determines how the emission is selected. This can be aided by creating a mask of where the real emission is to inform the algorithm. The real emission is then re-convolved with a Gaussian beam of FWHM equal to that of the dirty beam and the final clean image is ready. For observations of ^{12}CO lines the final data product is a RA-Dec.-velocity data cube.

To estimate the amount of molecular gas the total integrated ^{12}CO intensity ($I_{\rm CO}$) is calculated by summing over all 3 axes of the data cube. This is then multiplied by a conversion factor $\alpha_{\rm CO}$ (or $X_{\rm CO}$) to obtain the total mass surface density of molecular gas ($\Sigma_{\rm H_2}$, or $N_{\rm H_2}$ the $\rm H_2$ column density). The conversion factor ($\alpha_{\rm CO}$) has been measured in the Milky Way to be $\approx 4.3\,{\rm M_\odot}\,({\rm K\,km\,s^{-1}})^{-1}\,{\rm pc^{-2}}$, with similar values found in other nearby spiral galaxies (Bolatto et al., 2013). However it is theorised to increase with decreasing metallicity, which dust determinations agree with (Bolatto et al., 2013). $\alpha_{\rm CO}$ also appears to be positively correlated with optical depth, as indicated by dust continuum emission, e.g. in ultra-luminous infrared galaxies where $\alpha_{\rm CO} \approx 0.8\,{\rm M_\odot}\,({\rm K\,km\,s^{-1}})^{-1}\,{\rm pc^{-2}}$ (Downes & Solomon, 1998). In general there is great discussion of the best value to use, see Bolatto et al. (2013) for a full discussion. Despite an increased ability to resolve molecular gas in extragalactic sources most analysis still makes the simplistic assumption that the molecular gas in other galaxies behaves similarly to that in the Milky Way. I will discuss more on $\alpha_{\rm CO}$ later in this thesis, including how I proposed to aide its determination in extragalactic sources.

In this thesis we are interested in the evolution of galaxies, and in particular the regulation of their molecular ISM. Such studies extragalactically require high resolution, and thus long baseline interferometry. As this type of observatory has only recently come online (e.g. ALMA in 2011) the scientific discoveries are still in progress.

1.3 SMBH-GALAXY CO-EVOLUTION

Returning to galaxy evolution, it was mentioned above that black holes are expected to play a key role in galaxy evolution. One of the key pieces of evidence for this comes from cosmological simulations and the dark matter halo mass function they predict. Λ-CDM based cosmological simulations predict the distribution of dark matter halo masses to have a relatively steep slope ($d\log(N)/d\log(M) \sim -0.9$), see Model 1 (dashed line Fig. 1.2; Benson et al. 2003) where the dark matter halo mass function has been converted into a galaxy luminosity function by assuming a fixed mass-to-light ratio. This does not fit the observed galaxy luminosity function, shown by the points in Fig. 1.2, which is characterised by a shallower Schechter function (Schechter 1976; Bower et al. 2012). The mass function of galaxies $10^8 \lesssim M_* \, h^{-1}\,\mathrm{M}_\odot \lesssim 10^{10.5}$ is approximately independent of mass, and decreases exponentially above this range (Bower et al., 2012). The offset between the two functions raises questions, specifically (i) why is the number of low mass ($M_* \lessapprox 10^{10.5}\,h^{-1}\,\mathrm{M}_\odot$) galaxies flat as a function of mass when halo mass is a strong function of mass and (ii) what physical processes cause the exponential cut off in number of galaxies at masses $M_* \gtrapprox 10^{10.5}\,h^{-1}\,\mathrm{M}_\odot$(e.g. White & Frenk 1991; Benson et al. 2003; Bower et al. 2012).

Λ-CDM based cosmological simulations have consequently been forced to incorporate multi-scale 'feedback' into their models which take the outputs of supernovae and AGNs (mass, energy and metals) and produces their effect in the surrounding ISM and intergalactic medium. It is found that the inclusion of these processes not only relieves the tension between dark matter halo and stellar mass functions but also correctly simulates the enrichment of the ISM with metals (e.g. Springel & Hernquist 2003; Benson et al. 2003; Bower et al. 2006, 2012; Booth & Schaye 2009). The improvement in fit of the simulations to the data can be seen in Fig. 1.3 (from Bower et al. 2012) where the blue and green line are new models that include AGN 'hot-halo' feedback. The red line (Fig. 1.3) shows the effect of switching off this feedback, as it no longer correctly reproduces the high mass cut off in the galaxy mass function.

Supernova winds are less energetic than AGN winds and are therefore less able to disrupt the gas within massive ($M_* \gtrapprox 10^{10.5}\,h^{-1}\,\mathrm{M}_\odot$) dark matter halos. Supernova are found to be the dominant feedback for low mass galaxies ($M_* \lessapprox 10^{10.5}\,h^{-1}\,\mathrm{M}_\odot$; e.g. Bower et al. 2012 especially their Fig. 3), most notably their winds can cause galactic winds and outflows but on a smaller scale their thermal heating, cloud evaporation and metal enrichment also contribute to quenching a galaxy (Springel & Hernquist, 2003).

At higher mass AGN begin to dominate the feedback process but the exact details of this feedback is yet to be established. A large obstacle to this is measuring the 'amount' of AGN, there are multiple types of AGN, with different observational features so comparing them is problematic. As the object behind AGN, and a ubiquitous part of a galaxy, SMBH are the ideal comparison point of this process. The property observable of a SMBH is its mass, which also dictates its accretion ability and therefore its feedback capability. Rather problematically SMBH masses can be difficult to measure. Initially the co-evolution of SMBH and their hosts seems implausible for SMBH are tiny in comparison compared to their host galaxy, 'similar to a coin in comparison to the Earth' (Fabian, 2012), and hence their gravitational influence only reaches $\sim 1-100\,\mathrm{pc}$ (e.g. Kormendy & Ho 2013).

Fabian (2012) performs a simple 'back of the envelope' calculation to determine if the accretion on to a SMBH has the potential to have a 'profound effect on its host galaxy'. The binding energy of a galaxy with velocity dispersion σ and bulge mass M_{bulge} is $E_{\mathrm{bulge}} = M_{\mathrm{bulge}}\sigma^2$. Typically the SMBH mass is $M_{\mathrm{BH}} \approx 1.4 \times 10^{-3} M_{\mathrm{bulge}}$ (e.g. Ferrarese & Merritt 2000; Kormendy & Gebhardt 2001). Assuming a radiative efficiency of ~ 10 percent then the energy released by the growth of the SMBH is $E_{\mathrm{BH}} = 0.1 M_{\mathrm{BH}} c^2$. Then the ratio of the two energies $E_{\mathrm{BH}}/E_{\mathrm{bulge}} \approx 1.4 \times 10^{-4}(c/\sigma)^2$. Ordinarily galaxies have $\sigma < 400\,\mathrm{km\,s^{-1}}$, therefore $E_{\mathrm{BH}}/E_{\mathrm{bulge}} < 80$ and the energy released by the SMBH growth exceeds the binding energy of the galaxy by a large factor. In the event that even a small fraction of the SMBH energy can be transferred to the gas the effect would be major, as I will demonstrate in Chapter 5. This simple estimation shows the potential for SMBH-host galaxy co-evolution. As previously stated, the energy of SMBH is able to release is directly related to its mass, in Section 1.4 and Chapters 2 and 3 I will detail the techniques used to measure such masses.

The first relation to gain traction was $M_{\mathrm{BH}} - M_{\mathrm{bulge}}$, SMBH mass to bulge mass (e.g Magorrian et al. 1998; Marconi & Hunt 2003; Scott et al. 2013). Note that this is classical bulge mass and should not include pseudobulges. Galactic bulges grow through dry (gas poor) mergers, which move a galaxy towards the early-type morphology (e.g. Steinmetz & Navarro, 2002; Conselice, 2003). The $M_{\mathrm{BH}} - M_{\mathrm{bulge}}$ relation implies that mergers are critical to both galaxy evolution and SMBH mass growth. This idea also fits with some of the other correlations found, and the non-correlations. In particular the lack of correlation between SMBH mass and any stellar disc property bolstered the idea that for SMBHs only the host nucleus mattered and that external forces, rather than internal processes, were the ones to grow it (e.g. Magorrian et al. 1998; Marconi & Hunt 2003; also reviews by e.g.

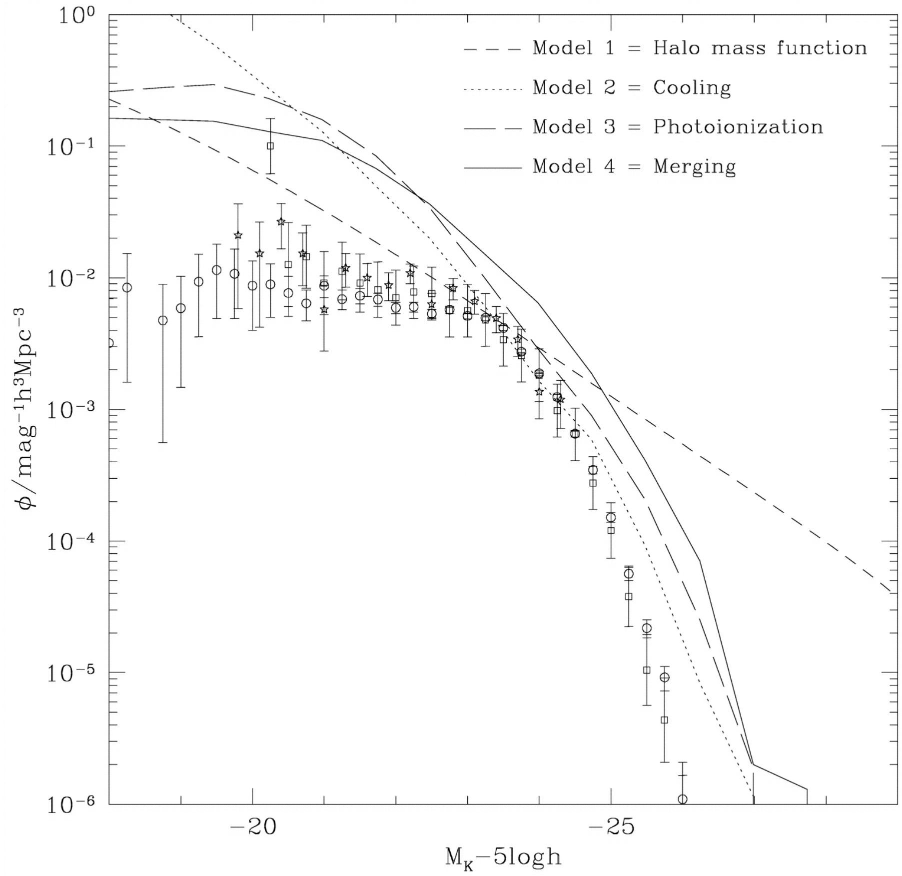

Figure 1.2. Figure 1 in Benson et al. (2003), *K*band luminosity function of galaxies. The points show the observational determinations of Cole et al. (2001; circles), Kochanek et al. (2001; squares), and Huang et al. (2003; z¡0.1, stars). Lines show model results. Model 1 (dashed line) shows the result of converting the dark matter halo mass function into a galaxy luminosity function by assuming a fixed masstolight ratio chosen to match the knee of the luminosity function. Model 2 (dotted line) shows the result from GALFORM when no feedback, photoionization suppression, galaxy merging, or conduction is included. Models 3 and 4 (longdashed and solid lines, respectively) show the effects of adding photoionization and then galaxy merging.

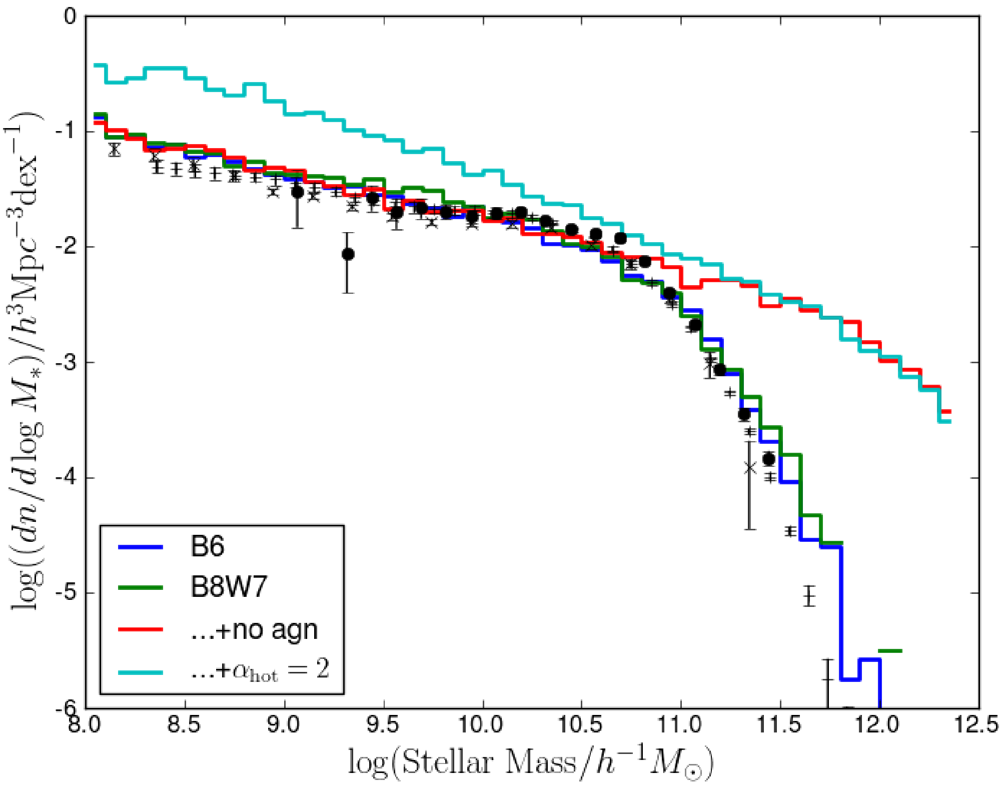

Figure 1.3. Figure 1 in Bower et al. (2012), Comparison of the stellar mass function of Bower et al. (2006, blue line) with the baseline Bower et al. (2008, green line) model used in Bower et al. (2012). This is based on the Wilkinson Microwave Anisotropy Probe(WMAP7) cosmology and inclused AGN 'hot-halo' feedback following Bower et al. (2008). The two models are almost indistinguishable. To illustrate the importance of AGN feedback, they show the effect of turning off the AGN feedback (red line). For comparison, observational data are shown as black points. The data taken from Bell et al. (2003, circles) and Li & White (2009, crosses).

Kormendy & Ho 2013; van den Bosch 2016).

SMBH masses are also found to correlate with bulge Sérsic Index (n), Graham & Driver (2007) find a log-quadratic fit describes the correlation well. In general this relation indicates that a more centrally concentrated galaxy, that with a larger bulge, will have a larger SMBH. At the low-n end this correlation predicts SMBHs with mass $M_{\rm BH} \approx 10^3\,{\rm M}_{\odot}$for $n \sim 0.5$ dwarf ellipticals. However, the quadratic shape does imply a more complicated story than simply bulge and SMBH grow together. The quadratic relation predicts a maximum SMBH mass for any n of $M_{\rm BH} \approx 10^9\,{\rm M}_{\odot}$, however this is inconsistent with recent SMBH mass measurements of $\geq 10^9\,{\rm M}_{\odot}$(e.g. Thomas et al. 2016; Boizelle et al. 2019; North et al. 2019 see Chapter 3; Smith et al. sub. 2020) bringing into question how widely applicable the relation is.

Studies so far have agreed that the $M_{\rm BH} - \sigma_{\rm e}$ (SMBH mass to luminosity-weighted line-of-sight stellar velocity dispersion within one effective or half-light radius) relation is both the tightest SMBH-galaxy relation and the one that applies to most galaxies independent of morphology or size. Gebhardt et al. (2000) compare this to the fundamental plane, creating a four dimensional space of coordinates $\log M_{\rm BH}$, $\log L$, $\log \sigma_{\rm e}$, $\log R_{\rm e}$ (where L is the total luminosity and $R_{\rm e}$ is the effective radius). They conclude that the $M_{\rm BH} - \sigma_{\rm e}$ relation implies that a) galaxies are still constrained by the 2-dimensional fundamental plane in the 3-dimensional space ($\log L$, $\log \sigma_{\rm e}$, $\log R_{\rm e}$) and b) the projection on to $\log M_{\rm BH}$, $\log \sigma_{\rm e}$ is viewing the fundamental plane edge on (Gebhardt et al., 2000). Interestingly whilst the $M_{\rm BH} - \sigma_{\rm e}$ relation appears to apply to all galaxies it still implies bulges and SMBHs grow together.

Kormendy & Ho (2013) review this coevolution (or not) between SMBH and host galaxy, Fig. 1.4 shows their comparison between the $M_{\rm BH} - M_{\rm bulge}$ and $M_{\rm BH} - \sigma_{\rm e}$ relations. It illustrates the difference in scatter between the two relations, with $M_{\rm BH} - \sigma_{\rm e}$ being much tighter.

These relations show the close connection between SMBH and host galaxy. However they are based on a small sample of SMBH mass measurements, so to understand the full picture more measurements are needed, both in galaxies of different morphologies but also at high redshift. I will explore SMBH mass measurements in Section 1.4 and present how the WISDOM project aims to help the SMBH sample size in Chapter 2. The other problem for co-evolution theories is confidently linking the observable quantities to physical meaning and hence ascertaining a cause and effect, this is more a long term problem which will slowly be solved with more observational evidence.

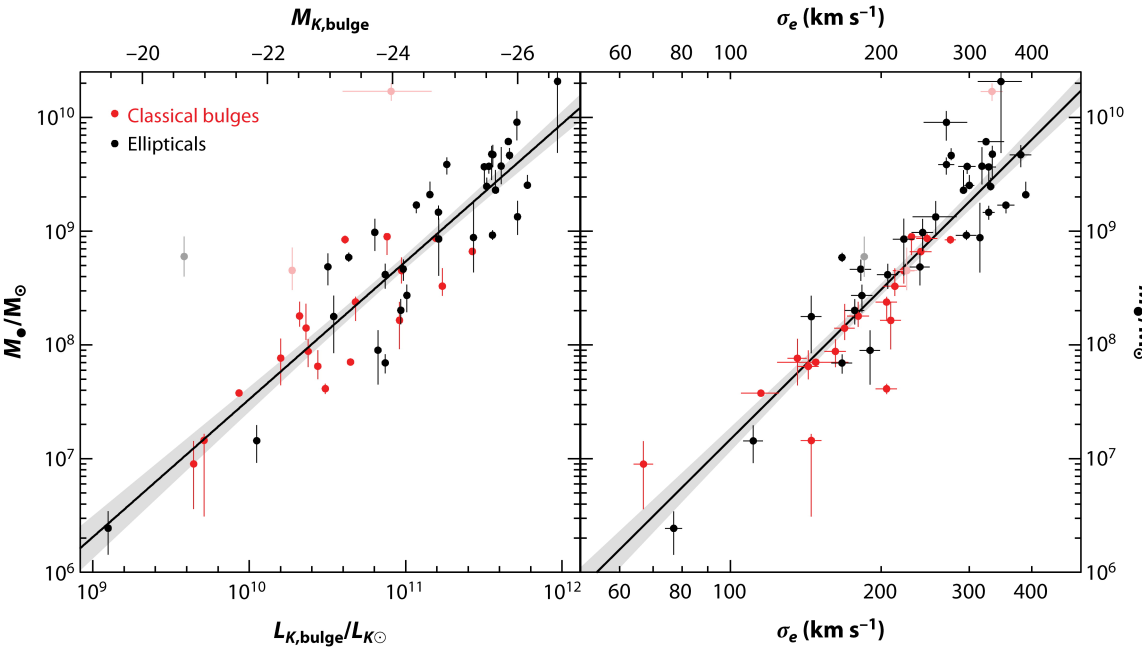

Kormendy J, Ho LC. 2013.
Annu. Rev. Astron. Astrophys. 51:511–653

Figure 1.4. Figure 12 of Kormendy & Ho (2013): Correlations between $M_{\rm BH}$ and (left) the K-band absolute magnitude of the classical bulge or elliptical and (right) its effective velocity dispersion.

1.4 MEASURING SMBH MASSES

The previous chapter demonstrates the importance of SMBH in galaxy evolution, which is quantified by relations between galactic properties and SMBH mass ($M_{\rm BH}$; see e.g. Kormendy & Ho 2013 for a review). The measurement of SMBH in a large range of galaxies is therefore critical to understanding galaxy evolution, in particular the regulation of the gas reservoirs within galaxys. Further to this the massive size of SMBHs opens up questions on their origin. Accretion occurs too slowly to have built up such mass from a stellar mass seed, so a larger seed is required. These larger seeds could have formed from the earliest stars, or by direct collapse from primordial gas. Answering this has implications for both cosmology and galaxy formation. The current data on SMBH masses does not sample the range of black hole masses well enough to begin to confirm any theories, in particular intermediate mass black holes need to be measured as these could be the seeds of SMBH (e.g. Volonteri et al. 2003; Davis et al. 2020). As the problem to be tackled by the WISDOM project and hence the purpose of the data I will present in this thesis I now discuss the problems related to measuring SMBH masses.

The advent of high resolution telescopes across most of the electromagnetic spectrum mean there are many ways to measure or infer a SMBH mass. The most reliable methods directly probe the gravitational potential of the SMBH to determine its mass. At the cnetre of a galaxy there are multiple objects to consider when predicting the gravitational potential, to achieve an accurate measurement these must be well modelled. The simplest of these methods determine the mass enclosed within a radius r via the velocity V of test particles, using Newtonian physics this is $M_{\rm enc} = V^2 r/G$, where G is the gravitational constant. The expected mass, that due to stars, can be calculated from the star light (luminosity , L) and a mass-to-light ratio (M/L). Then any extra mass, above the stellar mass, is attributed to a 'dark massive object' or SMBH. To confidently conclude an SMBH is the only explanation for the increasing velocities measurements close to the SMBH are required, this allows for accurate modelling of the other potential gravitational sources. Test particles used so far are the stars themselves or gas in orbit about the centre of the galaxy. Depending on the distance to the galaxy individual stars can be used. This technique of directly observing the orbits of stars about the SMBH as been used very successfully in the Milky Way. The development of Adaptive Optics has resolved the Milky Way nuclear star cluster into individual stars whose orbits can be tracked. Ghez et al. (2005) model the orbits of 7 proper motion stars within $0\overset{\prime\prime}{.}4$ to determine a mass of $(3.7 \pm 0.2) \times 10^6 [R_0/8\,\mathrm{kpc}]^3$ $\mathrm{M}_\odot$, work which one them the Nobel Prize for Physics in 2020. The Galactic centre's distance, which adds an additional 19 percent uncertainty, is now the limiting source of uncertainty in the absolute mass. This is the best SMBH mass measurement made to date, one of the stars has a pericenter radius of 45 ± 14 AU$\approxeq 500\, r_{\rm schw}$ and the only conclusive evidence of a black hole.

Similar to observing and modelling the orbits of individual stars, the general motion of the stars in the nucleus of a galaxy can be used. The mean velocity and velocity dispersion can be observed by spectroscopy of stellar absorption lines. Again models can be made, including observational effects e.g. seeing, and then fitted to the data to determine the probable SMBH mass. Large rotational velocities and velocity dispersions near the centre of the galaxy (or position of the SMBH) are the best indicator of large mass. The inclusion of dark matter in dynamical models was first applied to M 87 by Gebhardt & Thomas (2009), this proved important as it decreases M/L at large radii by attributing some of the mass there to dark matter and not luminous matter. The radially constant M/L therefore decreases in the centre and $M_{\rm BH}$ increases to balance the dynamical mass. Stellar absorption lines are best observed in bright, dense galaxies without significant dust obscuration, and thus tends to work better for ETGs.

Continuing the use of spectroscopy but turning to nebular emission lines from ionised gas, these can also be used to trace the gravitational potential of galaxies. Spiral galaxies have detectable optical nebular emission lines in their central few hundred parsecs, as do >50 percent of S0s and elliptical galaxies (Ho et al., 1997). The lines are also readily observable at ground based resolutions, despite only $\sim 10^4 - 10^5\,\mathrm{M}_\odot$ of warm (10^4 K) gas being present (Ho et al., 2003). Nebular emission lines have larger equivalent widths and relatively simple line profiles, making measurements of the velocities and velocity dispersion straightforward Kormendy & Ho (2013). The dynamical modelling of ionised gas is also much simpler than that for stellar orbits, if the gas is in Keplerian rotation in a dynamically cold disc. Simple axisymmetric models of circular orbits, including the potential due to stars and that due to the SMBH, can be fitted to the observations. However, ionised gas modelling requires the gas to be in a dynamically cold disc, which must be checked on a galaxy-by-galaxy basis. Broad emission lines caused by high velocity dispersion and non-circular motions are difficult to physically interpret which then causes uncertainty as to whether they need to be modelled. Dust attenuation complicates the luminous mass model by obscuring parts of the disc which may require masking during modelling.

The current gold standard for SMBH mass measurement is the use of megamasers as the tracer of the gravitational potential, because megamasers can occur close to the SMBH and radio interferometry allows them to be resolved there. Megamasers are microwave lasers mostly made by water molecules (and OH), the lines are strong and intrinsically narrow (Miyoshi et al., 1995). The first use of megamasers for SMBH mass measurement was Miyoshi et al. (1995), who measured the SMBH mass in NGC 4258 which has velocity components offset $1000\,\mathrm{km\,s^{-1}}$ within ~ 4milliarcseconds of the SMBH. The best megamaser measurements reach angular radii of a few milliarcseconds (Kormendy & Ho, 2013). Megamaser emission has the potential to expand the range of objects with SMBH mass measurements, occurring commonly in gas-rich, optically obscured, star-forming galaxies, and often with AGN emission. Unfortunately to observe megamaser emission the masing disc must be viewed to within a few degrees of edge on and the beam direction must hit Earth, the likelihood of such an event is low (Kormendy & Ho, 2013; Greene et al., 2010). For instance the probability of observing the maser emission from NGC 4258 is ~ 6 percent given the beam angle of 8° and assuming random inclination, this is approximately the detection rate of megamasers in active galaxies (Miyoshi et al. 1995; Lo 2005). Megamaser emission has expanded the SMBH range to lower masses, but as a rare object it won't be able to explore the full range of SMBH masses.

Other methods for estimating SMBH masses use relations calibrated in the near universe and then applied further afield. For instance, reverberation mapping of AGN broad line emission regions uses direct measurement of both the RMS velocity (ΔV) of gas near the SMBH and the radius of the broad emission-line region (R_{BLR}) to measure the SMBH mass via $GM_{\mathrm{BH}} = fR_{\mathrm{BLR}}\Delta V^2$ (e.g. Blandford & McKee 1982; Peterson 1993; Peterson & Horne 2004; Peterson 2008; Denney et al. 2010; Beckmann & Shrader 2012). The broad emission-line region (BLR) is gas surrounding the SMBH that is excited by continuum emission from the accretion disc, the continuum emission varies and in response to this so does the emission lines. There is a lag between the two due to the distance travelled by the light from emission to the gas of the BLR, the time lag is $\tau = R_{\mathrm{BLR}}c$ where c is the speed of light (e.g. Blandford & McKee 1982; Peterson 1993; Peterson & Horne 2004; Peterson 2008; Denney et al. 2010; Beckmann & Shrader 2012). The local calibration comes into the factor, f, which is not well known and changes for each galaxy as it depends on the geometry and dynamics of the BLR gas. Peterson et al. (2004) and Onken et al. (2004) calculated the average scaling factor, $< f >$, that removes the statistical bias in reverberation mapped (i.e. AGN) SMBH masses to bring them in to agreement with the $M - \sigma$ relation for quiescent galaxies. Whilst the method is very successful, care must be taken when applying local correlations elsewhere as the exact !!! The field of galaxy evolution needs a diverse sample of SMBH covering the full range of masses, including into the Intermediate Black Hole (IMBH) mass range. To obtain such data a new method of measuring SMBH masses which not biased towards dense and bright galaxies or reliant on rare alignments within galaxies is required. Any new method will have biases however as long as these cover a different range of galaxies to the current methods new insights into story of this co-evolution will be found.

This thesis concentrates on one of these new methods, using the rotation of molecular gas around SMBHs to measure their mass- work which has been conducted as part of the WISDOM project.

CHAPTER 2
THE WISDOM PROJECT

To acquire knowledge, one must study; but to acquire wisdom, one must observe.

Marilyn vos Savant

The introduction chapter introduced the idea that SMBH-host galaxy relations and the physics behind them are a key part of galaxy evolution and that to understand the co-evolution more SMBH mass measurements are required. I also discussed the current methods to dynamically measure SMBH masses and their biases towards nearby, high surface brightness objects. To truly test the co-evolution of galaxies and their SMBHs we need a more diverse sample, and therefore a new method of measuring SMBH masses. The mm-Wave Interferometric Survey of Dark Object Masses (WISDOM) project was set up with the aim of exploiting such a method to expand the sample of known SMBH masses. This project aims to use molecular gas as the kinematic tracer of a galaxy's gravitational potential and therefore with high enough resolution, to trace the velocity field surrounding the SMBH. Suitable, i.e. relaxed and close to the SMBH, molecular gas discs are found in most galaxies and not constrained to a particular type of galaxy (e.g. Sage & Wrobel 1989; Regan et al. 2001; Alatalo et al. 2013). Molecular gas has also been shown to be an excellent dynamically cold tracer of the galactic potential as e.g. Wiklind & Henkel (1989); Wrobel & Kenney (1992); Young et al. (2008); Crocker et al. (2009); Davis et al. (2011, 2013a); Ramakrishnan et al. (2019). As mentioned in Section 1.2.1 carbon monoxide (CO) is observable both without dust attenuation and, with the advent of long baseline millimetre interferometry, at the high resolution required for this work. In particular the ^{12}CO(2–1) transition is a good compromise between resolution and sensitivity. Higher-J CO lines lack sensitivity because of atmospheric absorption and ^{12}CO(1–0) gives lower resolution.

For a full example of the molecular gas method see Chapter 3 but briefly, the molecular gas kinematics are governed by the gravitational potential of the luminous material (stars, gas) and that of any dark components (SMBH, dark matter). High-resolution near-infrared imaging can be used to determine the distribution of the stellar component. The interferometric observations also inform us of the mass of molecular gas which may be included in the fitting if it contributes significantly to the central mass density. The central dark matter content of most galaxies tends to be negligible and/or distributed evenly for instance Cappellari et al. (2013) constructed axisymmetric dynamical models of the 260 ATLAS^{3D} galaxies and found a median dark matter fraction of 13 percent. When modelling gravitational microlensing Bate et al. (2011) find that a smooth dark matter component, with percentages of 80 in the ETG MG 0414+0534 and 0 in the spiral galaxy Q2237+0305. Treu & Koopmans (2004) also model gravitational microlenses and required dark matter mass fractions of 0.15-0.65 inside one effective radius for ETGs out redshift ~ 1. it is therefore included in the mass-to-light ratio term (or, if large radius information is available, included self consistently by including the halo potential in the modelling). The difference between the luminous mass model kinematics and those observed is the contribution of the SMBH, the fitting can quantify this thus constraining the SMBH mass.

The molecular gas method was developed using Combined Array for Research in Millimeter-wave Astronomy (CARMA) data of the nearby galaxy NGC 4526 by Davis et al. 2013b. The resolution achieved ($0\farcs25$ or 20 pc along the kinematic axis of the galaxy) is equal to the sphere of influence ($R_{\rm SOI}$) of the SMBH in NGC 4526 predicted using the $M-\sigma_{\rm e}$ relation (Gültekin et al., 2009). Where the sphere if influence, the radius of the area where the SMBH dominates the gravitational potential, is defined as

$$\frac{R_{\rm SOI}}{\rm pc} \equiv G\left(\frac{M_{\rm BH}}{\rm M_\odot}\right)\left(\frac{\sigma_*}{\rm km\,s^{-1}}\right)^{-2}. \tag{2.1}$$

Where G is the gravitational constant and $M_{\rm BH}$ is the SMBH mass and σ_* is the stellar velocity dispersion, normally measured at one effective radius i.e. $\sigma_{\rm e}$ which is what we will use in this thesis unless otherwise stated. A SMBH mass of $4.5^{+4.2}_{-3.1} \times 10^8\,\rm M_\odot$was measured, the best-fitting model is shown as in the central panel of Fig. 2.1. Fig 2.1 also shows the gas distribution along the major axis which has a gap at $\approx 1-2''$, although this does not affect the ability to measure the SMBH mass as the Keplerian rotation of the gas is clearly detected. The SMBH mass and mass-to-light ratio are degenerate with each other, as the mass-to-light ratio increases the SMBH mass decreases. This highlights the importance of the stellar model in obtaining an accurate SMBH mass measurement. This was the proof of concept, and with the completion of baselines greater than 1 km at the Atacama Large Millimetre/submillitmetre Array (ALMA) the availability of such data was

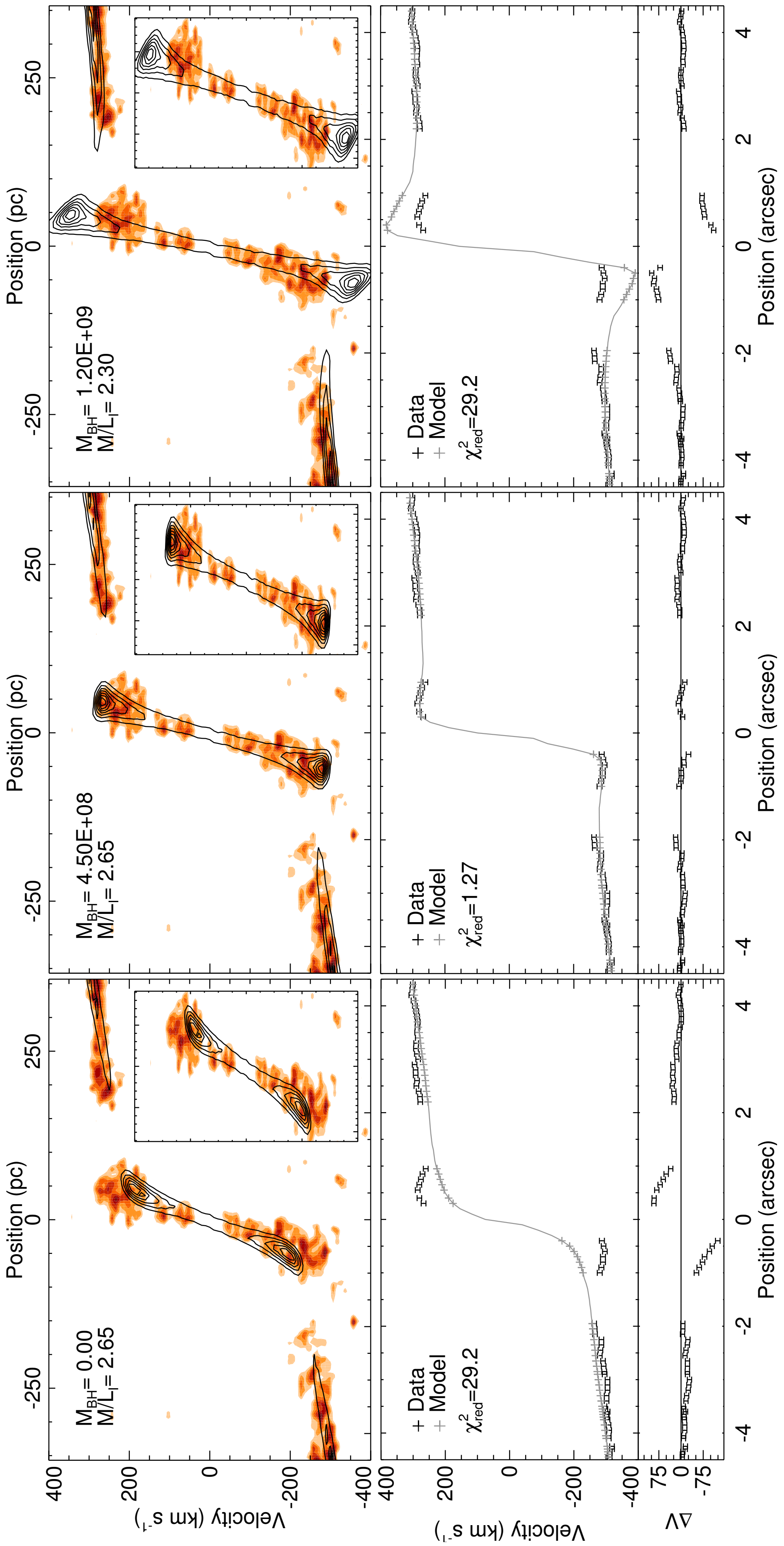

Figure 2.1. Reproduced with permission from Davis et al. (2013b): NGC 4526 kinematic models (black contours and grey points) and data (orange contours and black points)

set to increase.

2.1 FIGURE OF MERIT

In preparation for this increase in potential data Davis (2014) published a figure of merit for the molecular gas method (or any dynamically cold tracer) with the aim of aiding the design of future observational campaigns.

As in Davis (2014) the figure of merit ($\Gamma_{\rm FOM}$) is derived in the following. To detect the kinematic signature of the SMBH with molecular gas one must observe molecular emission at higher velocities than would be predicted from the luminous mass alone. $V_{\rm gal}(r)$ is the velocity a test particle would have in circular orbit in an edge on galaxy at radius r given the potential of the luminous mass alone. To claim a detection at the α confidence level the velocity difference, at the smallest resolvable radii, must be α times the error (δV). For a galaxy observed at inclination i this detection limit can be written mathematically as

$$V_{\rm obs}(r) - V_{\rm gal}(r)\sin i > \alpha\delta V\,, \tag{2.2}$$

where $V_{\rm obs}(r)$ is the observed velocity of the test particle. The potential of the SMBH is $\phi_{\rm BH}(r) = \frac{-GM_{\rm BH}}{r}$, where G is the gravitational constant and $M_{\rm BH}$ is the SMBH mass. Under the assumption of circular orbits in a flat disc at the same inclination as the galaxy $V_{\rm obs}(r) = \sqrt{[V_{\rm gal}(r)^2 - \phi_{\rm BH}(r)]}\sin i$. Substituting this into Equation 2.2 yields

$$\sqrt{V_{\rm gal}(r)^2 - \phi_{\rm BH}(r)} - V_{\rm gal}(r) > \frac{\alpha\delta V}{\sin i}, \tag{2.3}$$

which rearranges neatly to the figure of merit:

$$\Gamma_{\rm FOM} = \frac{\sqrt{V_{\rm gal}(r)^2 - \phi_{\rm BH}(r)} - V_{\rm gal}(r)}{\alpha\delta v}\sin i. \tag{2.4}$$

The $\Gamma_{\rm FOM}$ is one when an SMBH detection is made at a confidence level α. Section 2.3 of Davis (2014) describes several useful formula that follow from Equation 2.4. Davis (2014) note that if the beamsize (θ) is equal to the radius at which you wish to measure the SMBH mass then we can redefine the radius in terms of parsecs as $r = 4.84\theta D$, where D is the distance to the galaxy in mega-parsecs and the 4.84 factor comes from the definition of a parsec.

2.1.1 VELOCITY ERROR

The velocity error term (δV) expresses how well one can estimate the underlying potential and contains many components depending on the observations (channel width), velocity dispersion of the gas in the galaxy and the accuracy of the model used. In Davis (2014) they review only the error due to channelisation and the mass model used. According to Larson's first law, that the size ($R_{\rm c}$) and velocity dispersion ($\sigma_{\rm c}$) follow a power-law relationship of $\sigma_{\rm c} = 1.10 R_{\rm c}^{0.38}$, due to the thermal velocity dispersion and subsonic turbulence within the cloud (e.g. Larson 1981; Solomon et al. 1987; Heyer & Brunt 2004; Bolatto et al. 2008). Giant molecular clouds are tens to hundreds of parsecs across (e.g Fukui & Kawamura, 2010), which according to Larson's law gives velocity dispersions of $2-15\,{\rm km\,s^{-1}}$. This line width tends to be similar to the channel width used in such observations, normally $10\,{\rm km\,s^{-1}}$. For observations of low to intermediate signal-to-noise ratio (SNR) the true velocity of a gas particle cannot be known to better than half the channel width (CW; for high SNR estimations can be better than this) and consequently for similar treatment of both the model and real data the error is

$$\delta V\mid_{\rm chan} = \sqrt{2\left(\frac{CW}{2}\right)^2} = \sqrt{0.5}\,CW. \tag{2.5}$$

When the line width is larger than the channel width, and therefore well sampled, the true velocity can be more accurately determined and the velocity error includes both the channel width and the SNR. The model of the luminous matter will also have an associated error ($\delta V\mid_{\rm gal}$) which is to be added in quadrature as

$$\delta V\mid_{\rm tot} = \sqrt{0.5(CW)^2 + \delta V\mid_{\rm gal}}. \tag{2.6}$$

If required more terms can be added in quadrature depending on the observations and model used.

2.1.2 FIGURE OF MERIT PREDICTIONS

The $\Gamma_{\rm FOM}$ can be used to make predictions on how differing observational parameters will affect the recovery of the SMBH mass (see also Davis 2014). Here I show the affect of varying the inclination and the channel width on the minimum detectable SMBH mass, calculated from Equation 2.4. I use typical values for observations for the molecular gas method, a channel width of $10\,{\rm km\,s^{-1}}$and a detection limit of $\alpha = 5$ level. I also used typical observed values of a radius of $0\farcs15$ (12 pc at 16.5 Mpc), an inclination of $60^{\circ}$and $V_{\rm gal}(r) = 150\,{\rm km\,s^{-1}}$.

Of the parameters that affect Γ_{FOM}, the inclination is easy to limit during target selection. The minimum SMBH for different inclinations is shown in the left panel of Fig. 2.2, the SMBH mass decreases as the inclination increases, which is to be expected. As the inclination increases the component of the rotational velocity into the line of sight increases also, which splits the linewidth over more channels. Therefore at higher inclinations smaller changes in velocity (i.e. smaller SMBH mass) can be detected.

The right panel of Fig. 2.2 shows the minimum SMBH mass detectable (at the $\alpha = 5$ level) for different observed channel widths, again at a radius of $0\farcs15$ (12 pc at 16.5 Mpc) and an inclination of 60°. The typical minimum channel width used by extragalactic astronomers with ALMA for these observations is $2\,\mathrm{km\,s^{-1}}$. The right panel of Fig. 2.2 shows the SMBH mass detectable increasing with increasing channel width, which, again is to be expected. As the channel width decreases the velocity is better resolved so the influence of a smaller SMBH can be detected. However, as the channel width decreases the SNR also decreases as the noise per channel increases which can lead to signal dropping below the noise and thus not being detected, hence the need for accurate flux and linewidth predictions when selecting targets. Davis (2014) also show that for very narrow channels as the width becomes equivalent to the velocity error (e.g. how well one can estimate the underlying potential) the minimum SMBH mass detectable reaches an asymptote. The local SMBH mass function (e.g. Shankar et al. 2009) indicates most known SMBH have masses $10^{6.5} \leq M_{\mathrm{SMBH}} \leq 10^{10}\,\mathrm{M_\odot}$ which are covered at all channel widths under the above assumptions (e.g. at the distance of Virgo).

The trade off between resolution and SNR is important for the molecular gas method and the accurate recovery of SMBH masses. The unique nature of galaxies, their rotational velocity, mass of molecular gas and SMBH masses mean that selecting targets and the observations to make of them can be difficult. Below I discuss how targets were selected in the WISDOM project, but I return to these questions of SMBH detectability in Chapter 4.

2.2 TARGET SELECTION

The Davis (2014) figure of merit, and the useful formulae that follow from it, set criteria on what SMBH masses are within the observable range of current telescopes. The WISDOM project used this as part of their selection criteria for new observations. In 2016 I was involved in helping the WISDOM project create a catalogue of suitable targets to base future observing proposals on. The catalogue started from the HyperLEDA database (Makarov et al., 2014)*, selecting all those flagged as 'Galaxy' within the declination limits $-75° <$Dec.$< 30°$ as required for observation by ALMA. This selection provided

*http://leda.univ-lyon1.fr/

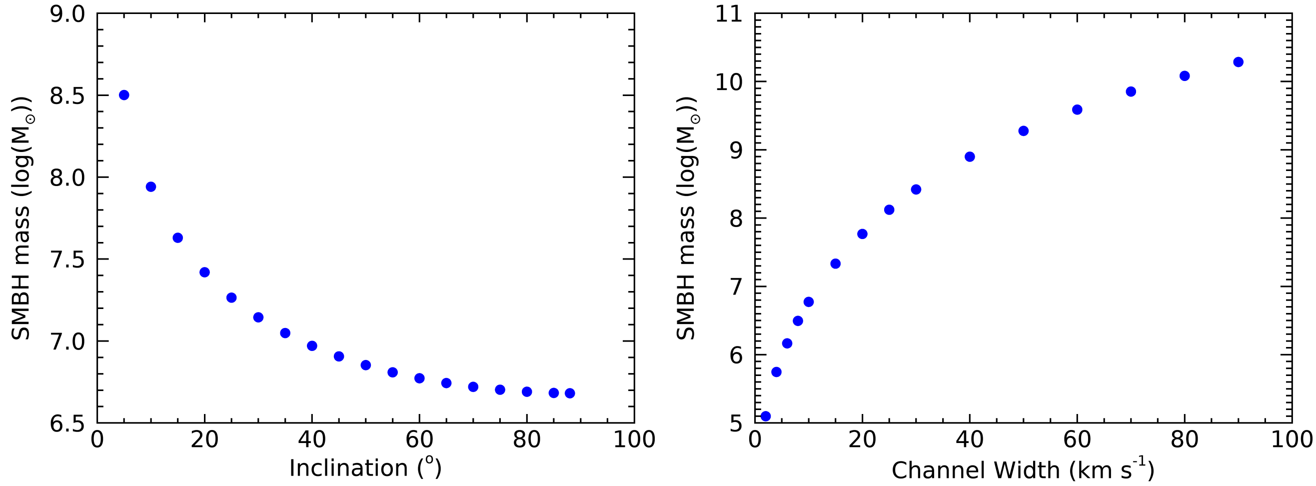

Figure 2.2. *Left panel:* Minimum SMBH mass detectable (at $\alpha = 5$) as a function of inclination. *Right panel:* Minimum SMBH mass detectable (at $\alpha = 5$) as a function of channel width for the observations. See text for other parameters.

2.5 million candidates. To obtain all the required information for each source, this list was cross-referenced against the SDSS DR13 (Albareti et al., 2017)[†], 2MASS extended source catalogue (XSC; Skrutskie et al. 2006[‡]), SIMBAD (Wenger et al., 2000)[§] and WISE (Cutri & et al., 2012)[¶] databases. The redshifts, morphological classifications, shapes, distances, apparent J, H, K and $W1-4$ band magnitudes and velocity dispersions were collected from across these databases and homogenised in units and value, where overlap occurred. Where data was available from multiple sources a mean was taken, ignoring obvious outliers. Where raw distances are not available a prediction was made using the redshift and Hubble's law ($\mathrm{H_0} \approx 70\,\mathrm{km\,s^{-1}\,Mpc^{-1}}$;Hubble 1929; Freedman et al. 2019).

From this raw data we predicted the SMBH sphere of influence and integrated ^{12}CO(1–0) flux for each galaxy. The SMBH mass was predicted by two methods; the $M_{\mathrm{BH}} - \sigma_{\mathrm{e}}$ relation of McConnell & Ma (2013) and the fundamental plane unification between K-band luminosity, effective radius, velocity dispersion and SMBH mass of van den Bosch (2016). The McConnell & Ma (2013) $M_{\mathrm{BH}} - \sigma_{\mathrm{e}}$ relation is:

$$\frac{M_{\mathrm{BH}}}{\mathrm{M_{\odot}}} = 10^{8.3}\left(\frac{\sigma_{\mathrm{e}}}{200\,\mathrm{km\,s^{-1}}}\right)^{5.6}. \tag{2.7}$$

The van den Bosch (2016) estimate requires correcting the effective radius (R_{e}) using

[†] `http://skyserver.sdss.org/dr13/en/home.aspx`
[‡] `https://irsa.ipac.caltech.edu/Missions/2mass.html`
[§] `https://simbad.u-strasbg.fr/simbad/`
[¶] `https://irsa.ipac.caltech.edu/Missions/wise.html`

$\log R_{\rm e} = 1.16 \log R_{\rm K\_R\_EFF} + 0.23 \log q_{\rm K\_BA}$, where $R_{\rm K\_R\_EFF}$ is the K-band effective radius and $q_{\rm K\_BA}$ is the K-band axis ratio as listed in the 2MASS‡ database. Also correcting the K-band luminosity, by correcting the the 2MASS‡ extrapolated K-band apparent magnitude ($m_{\rm K\_m\_ext}$) to $m_K = 1.01 m_{\rm K\_m\_ext} - 0.33$. The stellar velocity dispersion at an effective radius ($\sigma_{\rm e}$) is then

$$\log\left(\frac{\sigma_{\rm e}}{\rm km\,s^{-1}}\right) = 2.11 + 0.71 \log\left(\frac{L_*}{10^{11}\,{\rm L_\odot}}\right) - 0.72 \log\left(\frac{R_{\rm e}}{5\,{\rm kpc}}\right), \tag{2.8}$$

where L_* is the stellar luminosity in the K-band. The SMBH mass is

$$\log\left(\frac{M_{\rm BH}}{\rm M_\odot}\right) = 7.37 + 3.66 \log\left(\frac{L_*}{10^{11}\,{\rm L_\odot}}\right) - 3.42 \log\left(\frac{R_{\rm e}}{5\,{\rm kpc}}\right). \tag{2.9}$$

The integrated ^{12}CO(1–0) flux is estimated from the 12 µm luminosity (WISE $W3$-band, L_{12}), by converting L_{12} to a H_2 mass ($M_{\rm H_2}$) using the Jiang et al. (2015) correlation:

$$\log\left(\frac{M_{\rm H_2}}{\rm M_\odot}\right) = 0.88 \log\left(\frac{L_{12}}{\rm L_\odot}\right) + 1.49. \tag{2.10}$$

The $M_{\rm H_2}$ can then be converted to an integrated ^{12}CO(1–0) flux using

$$\int \left(\frac{I_{\rm CO}}{\rm Jy\,km\,s^{-1}}\right)\left(\frac{dV}{\rm km\,s^{-1}}\right) = 1.3 \times 10^{-4} \left(\frac{D}{\rm Mpc}\right)^2 \left(\frac{M_{\rm H_2}}{\rm M_\odot}\right), \tag{2.11}$$

where D is the distance to the object and dV is the bandwidth. To plan the observations the ^{12}CO(1–0) line width of the emission from the galaxy (at 50 percent of the maximum, W_{50}) is required. The linewidth informs us of the channel and band width required to well sample and fully observe the line. W_{50} can be calculated using the Tully-Fisher relation of Tiley et al. (2016) which requires the inclination (i) of the galaxy. Following Tiley et al. (2016) the inclination can be calculated from the SIMBAD§ or 2MASS‡ axis ratio (b/a, minor/major-axis length) and assuming $c/a = 0.34$ for ETGs and $c/a = 0.2$ for LTGs and unclassified (c is the z-axis length). Then the inclination is

$$\cos^2 i = \frac{\frac{b}{a}^2 - \frac{c}{a}^2}{1 - \frac{c}{a}^2}. \tag{2.12}$$

The Tully-Fisher relation found by Tiley et al. (2016) can be rearranged to give the linewidth as

$$\frac{W_{50}}{\rm km\,s^{-1}} = \sin i \times 10^{2.58} - \frac{M_{W1}/{\rm mag} + 23.83}{7.1}, \tag{2.13}$$

where $M_{\rm W1}$ is the WISE¶ band 1 absolute magnitude. Assuming the CO extends to one effective radius, the integrated flux is then distributed across the linewidth and divided by the number of beams in a minor axis:

$$\frac{I_{\rm CO}}{\rm Jy\,beam^{-1}} = \left(\frac{\int I_{\rm CO} dV}{\rm Jy\,km\,s^{-1}}\right)\left(\frac{W_{50}}{\rm km\,s^{-1}}\right)^{-1}\left(\frac{R_{\rm e}}{0.''06}\right). \tag{2.14}$$

The flux of the galaxy is split during observation, spectrally this is across the number of channels spanned by the emission. Spatially the flux is spread over the number of resolution elements (beams) needed to cover the galaxy, typically this is given by the minor axis length. Observations tend to be made of the ^{12}CO(2–1) line instead of (1–0), due to the higher resolution and sensitivity of ALMA in this band. A line ratio of $S_{2-1}/S_{1-0} = 0.7$ (Jiang et al., 2015) is used to convert the flux to a flux density at that wavelength. Assuming observations at zenith, an SNR of 3 and all 43 dishes of the ALMA 12 m array the exposure time for each object can be calculated. Samples are taken at 5 minute increments from the ALMA exposure time calculator and a power law is fitted and then extrapolated to the sensitivity required for each object.

Once this information has been assimilated cuts are made for the observing conditions available. The minimum resolution of ALMA (i.e. the maximum baseline) requires $R_{\rm SOI} \geq 0.''06$. A limit of 1 hour for on-source integration time selects 970 candidates, a limit of 2 hours would only select an additional 311 so these were put as secondary.

The choice of which objects to propose then begins from this list of 970, the obvious place to start is with those with existing CO observations or the highest predicted CO flux. To complete the kinematic model near-infrared imaging is required to create the luminous mass model, the next criteria for proposing a source is therefore to check for *Hubble Space Telescope (HST)* broad-band near infrared imaging (e.g. F110W, F160W or maybe F814W), and in particular that which shows a relaxed dust disc indicating the molecular gas will be so also. This is also a good check for mergers as these are likely to have disturbed kinematics unsuitable for this method so can be discarded from the candidate list.

2.2.1 OBSERVING STRATEGY

As mentioned in Chapter 1, Section 1.2.1 the maximum and minimum resolvable angular scales for an interferometer are important for planning observations. When using molecular gas as the kinematic tracer it is important to know how much molecular gas is present, therefore correct flux predictions are essential. To reduce the likelihood of resolving out flux the WISDOM project uses observations of varying baselines when making an SMBH mass estimate. Not only does this aide with *uv*-plane coverage but by initially only obtaining low resolution observations, which are quicker, the true suitability of the gas disc can be confirmed without the large input of time that a high resolution observation requires. In some cases, for very large SMBH, this low resolution observation can be used to make a measurement of the SMBH mass. The low resolution observation is the final check that the gas disc is suitable before high resolution observations are acquired.

Throughout the proposing cycles that I have been involved in the WISDOM project has focused on different characteristics of galaxies to group them into proposals, for instance high-mass SMBH masses or those at fixed velocity dispersion. Despite having smaller gas fractions (M_{H_2}/M_*), ETGs are the most common morphology for a published SMBH mass by the molecular gas method. The WISDOM project found that LTGs can have more disturbed gas, with bars being particularly problematic. Fig. 2.3 exhibits the moment zero maps of six WISDOM galaxies to show the quality of observations and the variety of gas distributions. Each galaxy is labelled with its morphological type to highlight how LTGs tend to be more disturbed. Again the WISDOM project aims to reduce the ETG bias by particularly targeting LTGs in recent observing proposals and publishing the first LTG SMBH mass measurement using dense gas tracers HCN and HCO^+ (Onishi et al., 2015). One of the most recent publications from the WISDOM project is the intermediate mass black hole mass measurement in dwarf galaxy NGC 0404 (Davis et al., 2020), this exhibits the molecular gas method's ability to explore more of the SMBH-host galaxy relation parameter space.

2.2.2 ANALYSIS TOOLS

The WISDOM project has developed a suite of tools for the analysis of molecular gas data and the measurement of SMBH masses, including a mm-wave kinematic molecular gas observation simulator tool, KINMS[‖] (Davis et al., 2013a) and a Markov Chain Monte Carlo (MCMC) code (KINMS_MCMC[**]). KINMS creates mock observation cubes from a surface brightness model, observational parameters (e.g. beam size) and a velocity curve, it also applies observational effects for instance beam smearing. KINMS_MCMC is written to easily interface with KINMS to create models, compare them directly with the data cube and perform likelihood maximisation to find the best-fitting model. These codes are available in both IDL and PYTHON. I use the IDL versions of these tools throughout this thesis (Chapters 3 and 4), and have helped to test and improve them. Early on in the project it was realised that galaxies with irregular gas morphologies would be difficult to model, requiring more complex parametrisations to properly reproduce them and therefore constrain the SMBH mass. However finding the correct model is difficult and results in

[‖] https://github.com/TimothyADavis/KinMS
[**] https://github.com/TimothyADavis/KinMS_MCMC

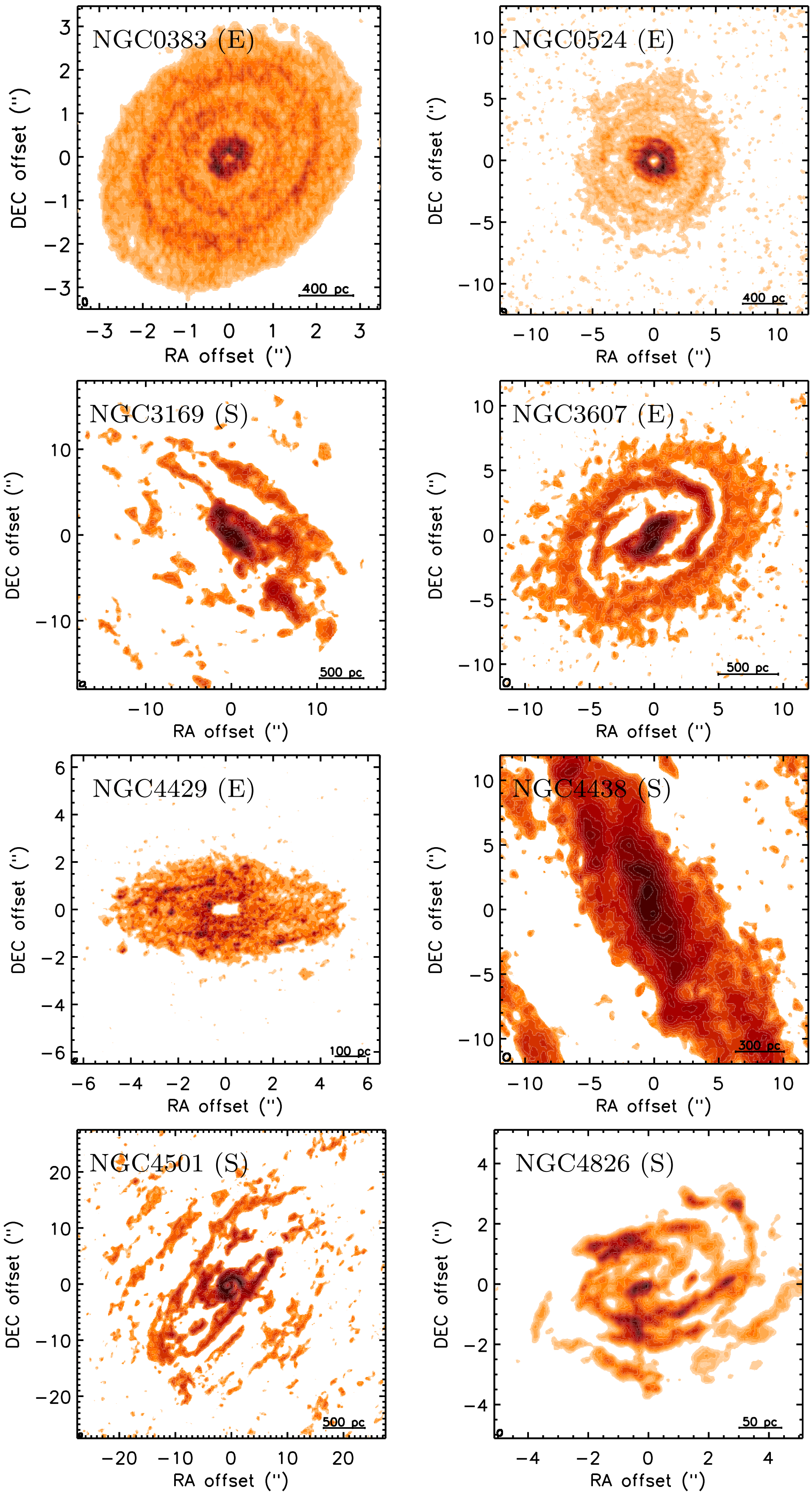

Figure 2.3. Moment zero maps of eight WISDOM galaxies to illustrate the variety of molecular gas distributions, each is labelled with its morphological type to highlight the increased clumpiness found in the gas distribution of late-type (S) galaxies compared to early-types (E). The RA and Dec. offsets are from the centre of the 230 GHz continuum source.

many more free parameters. The other option for modelling such structures is to use the observed gas distribution as an input, and so fit the total flux at each location. Smith et al. (2019, of which I am a co-author) developed SKYSAMPLER[††] to perform a fit to the observed gas distribution, again interfacing easily with the PYTHON version of KINMS[‡‡] to create models. For a full description of the SKYSAMPLER[††] code see Smith et al. (2019), also it is used in Chapters 3 and 4.

As an active member of the WISDOM project alongside working on SMBH mass measurements in specific galaxies and examining the accuracy of our methods via simulated observations I aided with target selection by searching the literature for previous low resolution CO observations that indicated a suitable gas disc. I also led several proposals for ALMA observations, for both SMBH mass measurements and to try and determine the CO-to-H_2 conversion factor, $X_{\rm CO}$.

2.3 MORE THAN SMBH MASSES

Due to the individuality of each galaxy, and its molecular gas, the WISDOM team tends to work on and publish each galaxy independently. The high resolution observations required for SMBH mass estimates using the molecular gas method are not only useful for that purpose. It was realised that these observations also reveal giant molecular clouds (GMCs) and their kinematics. The WISDOM project therefore diversified its activity and specialism to include research into this. Studies of GMCs in ETGs are lacking, and those published indicate that GMCs in ETGs do not follow the local size-linewidth relation, and have higher luminosity, density and velocity dispersion than Milky Way and local group GMCs (Utomo et al., 2015). Liu et al. (2020, of which I am a co-author) is the first WISDOM paper on GMCs, it introduces the methods and tools to be used for GMC analysis including a modified code to identify GMCs and new formalism for the Virial parameter of GMCs when shear is important e.g. in the centres of galaxies. We find high velocity gradients within individual GMCs and a steep size-linewidth relation, both of which are consequences of gas motions driven by the background galactic potential (Liu et al. 2020). The new Virial parameter analysis reveals that the clouds are only marginally self-gravitating as the gravitational potential contributes significantly to the clouds' gravitational budget (Liu et al. 2020). Analysis of a larger sample of ETGs is required to establish if these are common properties of GMCs in ETGs and such work is currently in preparation by the WISDOM project.

The data and kinematic modelling can also reveal gas flows within galaxies, if gas is

[††] `https://github.com/Mark-D-Smith/KinMS-skySampler`
[‡‡] `https://github.com/TimothyADavis/KinMSpy`

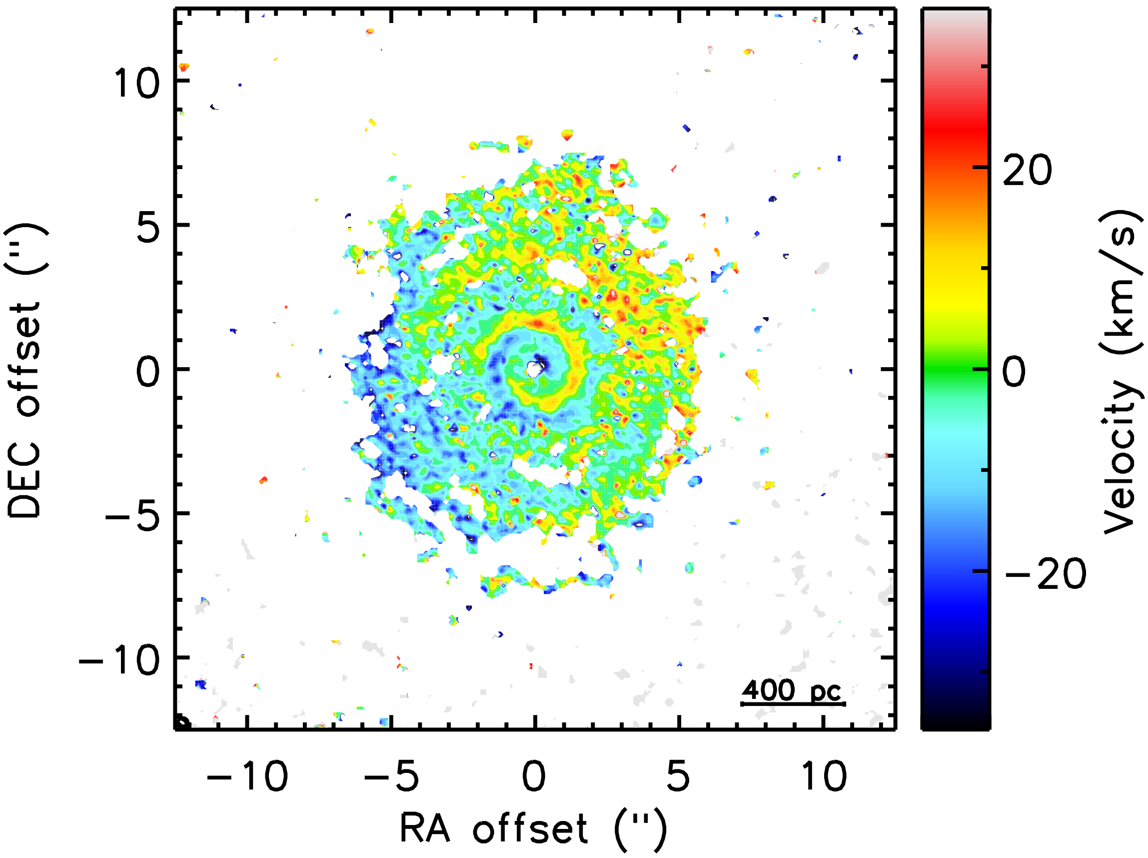

Figure 2.4. Reproduced with permission from Smith et al. (2019): Residuals between the first moments (mean velocity fields) of the data cube and best-fitting model cube. Positions are from RA= $01^{h}24^{m}47\overset{s}{.}75$, Dec.= $+9^{\circ}32'20\overset{''}{.}12$.

observed to flow towards the centre this can indicate a possible mechanism for feeding the SMBH. Gas flow can also affect the star formation rate by removing, destroying or adding to the star formation fuel. Non-circular motions can also be indicative of resonances, shear or tidal forces, all important to the evolution of the galaxy. When studying NGC 0524 Smith et al. (2019) found that the residuals of the data minus the best-fitting model, that assumes circular motion, exhibits a spiral feature (see Fig. 2.4). The feature has a peak amplitude of 15 km s^{-1}, $\approx$ 10 percent of the line-of-sight projected velocity and is therefore thought to trace not only a small perturbation on top of the dominant axisymmetric potential in NGC 0524 (Smith et al., 2019). Whilst this feature could be caused by radial flow, they find that a model with a kinematic position angle warp leaves no spiral structure in the residuals Smith et al. (2019). The WISDOM database of high resolution molecular gas data has great capacity to reveal the intricacies of gas in galactic centres. I find similar evidence for gas flows in NGC 0383 in Chapter 3 (North et al., 2019), the residuals are less pronounced than those in NGC 0524 so I do not attempt to fit or explain them.

The WISDOM project also noted that many ($\approx$ 20 percent of those observed in the project) galaxies have a central hole in their molecular gas, as traced by CO(2–1) or CO(3–2) emission. To ascertain the origin of these holes dense gas tracers and both higher- and lower-J CO lines have been proposed for. The galaxies observed to have molecular gas holes do not currently host an AGN, which leads to the question of what has caused the hole to form. The holes could be due to X-ray heating or tidal forces from the SMBH, shear from the entire galaxy, or a increase in the gas density changing the excitation state of the gas. Interestingly the radial size of the holes tends to be approximately that at which the SMBH begins to dominate the potential. If found, holes formed by X-ray heating or tidal forces from the SMBH would be a great example of very small-scale feedback by a SMBH. This would show how, even when not considered 'active' SMBHs still play an important role in ISM kinematics.

As mentioned above I led ALMA proposals for work other than SMBH masses, in particular determining the CO-to-H_2 conversion factor, $X_{\rm CO}$ or $\alpha_{\rm CO}$. This has long been debated (e.g. discussions in Bolatto et al. 2013 and Geach et al. 2014). Sandstrom et al. (2013) pioneered a new method for determining $X_{\rm CO}$ on $\sim$ sub-kiloparsec scales using dust to trace the molecular hydrogen surface density. The proposal was to use resolved *Herschel* observations (selected from Dustpedia Clark et al. 2018) with new ALMA ones and exploit the Sandstrom method. The resolved nature of this method allows for the variation of $X_{\rm CO}$ across a galaxy, i.e. in different environments, to be known. I also chose ETG candidates for the proposal as these appear to have very different gas conditions to the Milky Way, as evidenced by their very low star formation efficiencies (e.g. Saintonge et al. 2011a,b who assume a Milky Way $X_{\rm CO}$). Thus determining $X_{\rm CO}$ in ETGs is important for confirming the low star formation efficiencies, and then interpreting the gas conditions within them.

The WISDOM project uses not only ALMA CO observations, but also e.g. those of star formation tracers and ionised gas. I led proposals for Very Large Array (VLA) and Multi Unit Spectroscopic Explorer (MUSE) observations. With the VLA the aim was to observe 3 GHz continuum from supernova remnants to determine the star formation rate, which paired with molecular gas observations at similar resolution would allow the determination of star formation efficiencies and therefore why some star formation appears suppressed. Similarly with MUSE the proposal was to determine the SFR of galaxies where we already have high resolution molecular gas observations to determine quenching mechanisms, although tracing SFR with Hα. My VLA proposal was successful, unfortunately the data could not be used for the intended purpose as only central point-like emission was detected.

Since Davis et al. (2013b) molecular gas has demonstrated its accessibility and importance as a kinematic tracer, whose uses continue to expand and which the WISDOM project plans to employ to reveal the physics at play in ISM gas regulation and SMBH -host galaxy co-evolution. My work focuses on two galaxies from the WISDOM sample, both are local, massive galaxies with active nuclei and radio jets that were chosen by the WISDOM team for their relaxed molecular discs. I proposed observations of both galaxies in ALMA Cycle 4 as part of the massive galaxies proposal I submitted and I found the data that was returned fitted into my interest in AGN and their role in galaxy evolution. NGC 0383 was chosen for my work because of the high quality detection of the Keplerian rise in rotation velocity. Whereas from the data on NGC 0708 an SMBH mass measurement cannot be made due to the blue-shifted feature in the molecular gas. In the next chapter I present my work on NGC 0383, one of the neatest examples of an SMBH mass measurement with the molecular gas method, illustrating just how powerful the method can be.

CHAPTER 3
RESOLVING MOLECULAR GAS IN KEPLERIAN ROTATION AROUND THE SUPERMASSIVE BLACK HOLE IN NGC 0383

If you're going to let one stupid prick ruin your life, you're not the girl I thought you were.

Professor Stromwell (Legally Blonde)

The chapter presents the supermassive black hole mass measurement by the molecular gas method in NGC 0383. This work is published in North et al. (2019).

3.1 INTRODUCTION

Early-type galaxies, as gravitationally bound stellar systems, lie on a tight "Fundamental Plane" defined by their mass (luminosity), size (half-light radius) and second velocity moment (velocity dispersion; e.g. Djorgovski & Davis 1987; Dressler et al. 1987). Late-type galaxies follow less tight correlations such as the Tully–Fisher relation between mass (luminosity) and rotation velocity (Tully & Fisher 1977; see Courteau et al. 2014 and section 4 of Cappellari 2016 for reviews of the fundamental planes of galaxies). Comparing central supermassive black hole (SMBH) mass measurements with these galaxy properties has revealed further relations connecting, for example, bulge mass, stellar mass (or luminosity), or Sérsic concentration index to the SMBH mass (Kormendy & Richstone 1995; Magorrian et al. 1998; Marconi & Hunt 2003; Häring & Rix 2004; Graham & Driver 2007). This has led to the prevailing theory that SMBHs, despite their comparatively small masses, are a major influence on galaxy evolution (e.g. Beifiori et al. 2012; van den Bosch 2016). However, the SMBH-host galaxy relations are poorly constrained, with relatively few data points drawn from biased samples, and with large uncertainties. The mm-Wave Interferometric Survey of Dark Object Masses (WISDOM; see Chapter 2) projects focus is to address the bias in the SMBH mass sample by covering more morphological types and covering the gaps in the mass-size plane, see Chapter 6 for further discussion. Further evidence indicates both SMBH mass growth at the same rate as (e.g. Mullaney et al., 2012; Madau & Dickinson, 2014) and SMBH feedback quenching of (Bundy et al., 2008) star formation. Furthermore, whether all galaxies follow the same relations or not is still inadequately tested. In particular, there is evidence that low-mass late-type and high-mass early-type galaxies follow different co-evolutionary relationships (e.g. McConnell & Ma, 2013). Kormendy & Ho (2013) give a comprehensive review of the current state of these relations.

One of the tightest relationships is that between the SMBH mass ($M_{\rm BH}$) and the stellar velocity dispersion ($\sigma_{\rm e}$; e.g. Gebhardt et al. 2000; Ferrarese & Merritt 2000), but there is again growing evidence of divergence between galaxies of different morphological types or masses (e.g. McConnell & Ma 2013; van den Bosch 2016, esp. their Fig. 2; Krajnović et al. 2018). To fully analyse the extent of the co-evolution between all these galaxy properties, it is essential to gather a larger, more diverse, sample of *reliable* SMBH mass estimates (van den Bosch, 2016)

Reliability is achieved by directly measuring the SMBH masses through their gravitational influence. Methods to measure SMBH masses dynamically include observing and modelling the stellar kinematics (e.g. Dressler & Richstone, 1988; Cappellari et al., 2002; Krajnović et al., 2009), ionised gas kinematics (e.g. Ferrarese et al., 1996; Sarzi et al., 2001; Walsh et al., 2013) and megamaser kinematics (e.g. Miyoshi et al., 1995; Herrnstein et al., 1999; Greene et al., 2010). However, each of these methods can only be used in a small fraction of the galaxy population, as each is biased towards particular morphologies. For instance, stellar kinematics are often hampered by dust contamination and require either resolving individual stars directly or strong absorption lines in integrated spectra. Megamasers probe material very close to the SMBHs but require an edge-on view and are very rare (being present in only $\approx 5\,\%$ of objects searched; Lo 2005). They are typically found in Seyfert 2 and low-ionisation nuclear emission region (LINER)-type nuclei of low-mass galaxies. Overall the current sample is biased towards nearby, high surface brightness objects. A new method of measuring SMBH masses is thus required to diversify the sample.

To expand the current sample to all morphological types, galaxy masses and both active and non-active galaxies, the WISDOM project is using a new method exploiting molecular gas observations to trace the velocity fields surrounding SMBHs. The first use of this method with Carbon Monoxide (CO) was by Davis et al. (2013b). SMBH mass measurements in fast-rotator early-type galaxies (Onishi et al., 2017; Davis et al., 2017, 2018), an early-type galaxy with an irregular gas distribution (Smith et al., 2019), and in the first late-type galaxy with the dense molecular gas tracers HCN and HCO^+ (Onishi et al., 2015) have been successful. Barth et al. (2016a,b) and Boizelle et al. (2019) also used CO to constrain the SMBH mass in the early-type galaxies NGC 1332 and NGC 3258. Most recently, Combes et al. (2019) used CO(3–2) observations to investigate the molecular tori around seven SMBHs and therefore measure their SMBH masses. Nagai et al. (2019) observed the radial filaments of NGC 1275 in CO(2–1), detecting a rotating disc allowing them to make an SMBH mass estimate, that agrees with the estimate from H_2 observations by Scharwächter et al. (2013).

All these observations can detect the dynamical influence of the SMBH if, as shown in Davis (2014), they have a minimum spatial resolution of approximately two times the radius of the sphere of influence ($R_{\rm SOI}$, Equation 2.1) of the SMBH. The use of molecular gas, specifically ^{12}CO, reduces the selection biases normally associated with dynamical SMBH mass measurements, because of the wide range of objects with suitable molecular gas discs, and because the high angular resolution required is easily reached by modern interferometers, e.g. the Atacama Large Millimeter/sub-millimeter Array (ALMA). Indeed, molecular discs are found around the centres of galaxies of all morphological types (e.g. Regan et al., 2001; Alatalo et al., 2013). Furthermore, with rotational transitions in the millimetre/sub-millimetre wavebands, CO is observable without dust attenuation.

NGC 0383 (radio source 3C 031; Edge et al. 1959; Bennett 1962) is a well-known radio galaxy (implying the presence of a large SMBH), it has a very regular central dust disc and it is also strongly detected in CO (see Fig. 3.1 left and top right panel) with a clear double-horned profile (Lim et al., 2000; Okuda et al., 2005; Ocaña Flaquer et al., 2010). This chapter presents a measurement of the SMBH mass in this galaxy using ALMA observations of the ^{12}CO(2–1) line with a spatial resolution of $58 \times 32\,\mathrm{pc}^2$ ($0\farcs18 \times 0\farcs1$). In Section 3.2, I present the target, observations and data reduction. In Section 3.3, I describe the dynamical modelling and SMBH mass measurement method. A discussion of the uncertainties and comparisons to other SMBH mass measurement techniques are presented in Section 3.4. I conclude briefly in Section 3.5.

3.2 TARGET: NGC 0383

NGC 0383 is a dusty lenticular galaxy at a distance of 66.6 ± 9.9 Mpc (Freedman et al., 2001). It is the brightest galaxy of its group (the NGC 0383 group), part of the Pisces-Perseus Supercluster (Hudson et al., 2001). NGC 0383 hosts a radio-loud active galactic nucleus (AGN) with spectacular radio jets. The coincident radio source is catalogued as 3C 031 (Edge et al., 1959; Bennett, 1962). Observations of the jets are presented in MacDonald et al. (1968), Bridle & Perley (1984), Laing & Bridle (2002) and van Velzen et al. (2012), whilst the flat-spectrum radio source is described in Healey et al. (2007).

I can estimate the required angular resolution by predicting the $R_{\rm SOI}$ using the SMBH mass upper limit of Beifiori et al. (2009) ($M_{\rm BH} = 1.1 \times 10^9$ M$_\odot$, corrected to the distance and inclination assumed in this chapter, see Section 3.4.4) and $\sigma_{\rm e}$ as listed in van den Bosch (2016) ($\sigma_{\rm e} = 239 \pm 16$ km s^{-1} i.e. σ_* within $R_{\rm e}$ from Beifiori et al. 2009, corrected following Jorgensen et al. 1995). Using Equation 2.1 with these values, I obtain $R_{\rm SOI} = 82 \pm 15$ pc, indicating I need an angular resolution of better than $\approx 0\farcs5$ to attempt to detect the dynamical influence of the SMBH (i.e. to resolve $2R_{\rm SOI}$; Davis 2014).

There are existing ^{12}CO(1–0) observations of NGC 0383 from Lim et al. (2000), Okuda et al. (2005) and in particular single-dish observations from the Thorough ANalysis of radio-Galaxies Observation project (TANGO; Ocaña Flaquer et al. 2010). They report the total molecular gas mass enclosed by the Institut de Radioastronomie Millimétrique (IRAM) 30-m telescope beam to be $M_{\rm H_2} = (1.7 \pm 0.2) \times 10^9$ M$_\odot$. I correct this from 71.06 Mpc to the distance assumed in this chapter of 66.6 Mpc, yielding $(1.49 \pm 0.19) \times 10^9$ M$_\odot$ as the total molecular gas mass.

3.2.1 ALMA OBSERVATIONS

The ^{12}CO(2–1) line in NGC 0383 was observed with ALMA on June 21st 2016 at moderate resolution ($0\farcs5$ or ≈ 160 pc) and then on August 16th 2017 at high resolution ($0\farcs1$ or ≈ 32 pc), both as part of the WISDOM project (programmes 2015.1.00419.S and 2016.1.00437.S). Configurations C36-5 (baselines 15–704 m) and C40-8 (baselines 21–3637 m) were used to achieve sensitivity to emission on scales up to $4''$ (≈ 1.3 kpc), with on-source integration times of 2.22 and 28.8 min, respectively. A 1850 MHz correlator window was placed over the CO(2–1) line and centred at 226.6 GHz, yielding a continuous velocity coverage of ≈ 2000 km s^{-1} with a raw channel width of ≈ 1.3 km s^{-1}, fully covering and well resolving the line. Three additional low spectral resolution correlator windows were included to detect continuum emission, each of 2 GHz width.

The raw ALMA data were calibrated using the standard ALMA pipeline, as provided by the ALMA regional centre staff. The amplitude and bandpass calibrator used in the two observations was, respectively, J0237+2848 and J2253+1608. The phase calibration used J0057+3021 and J0112+3208, respectively, to determine and therefore correct atmospheric phase offsets.

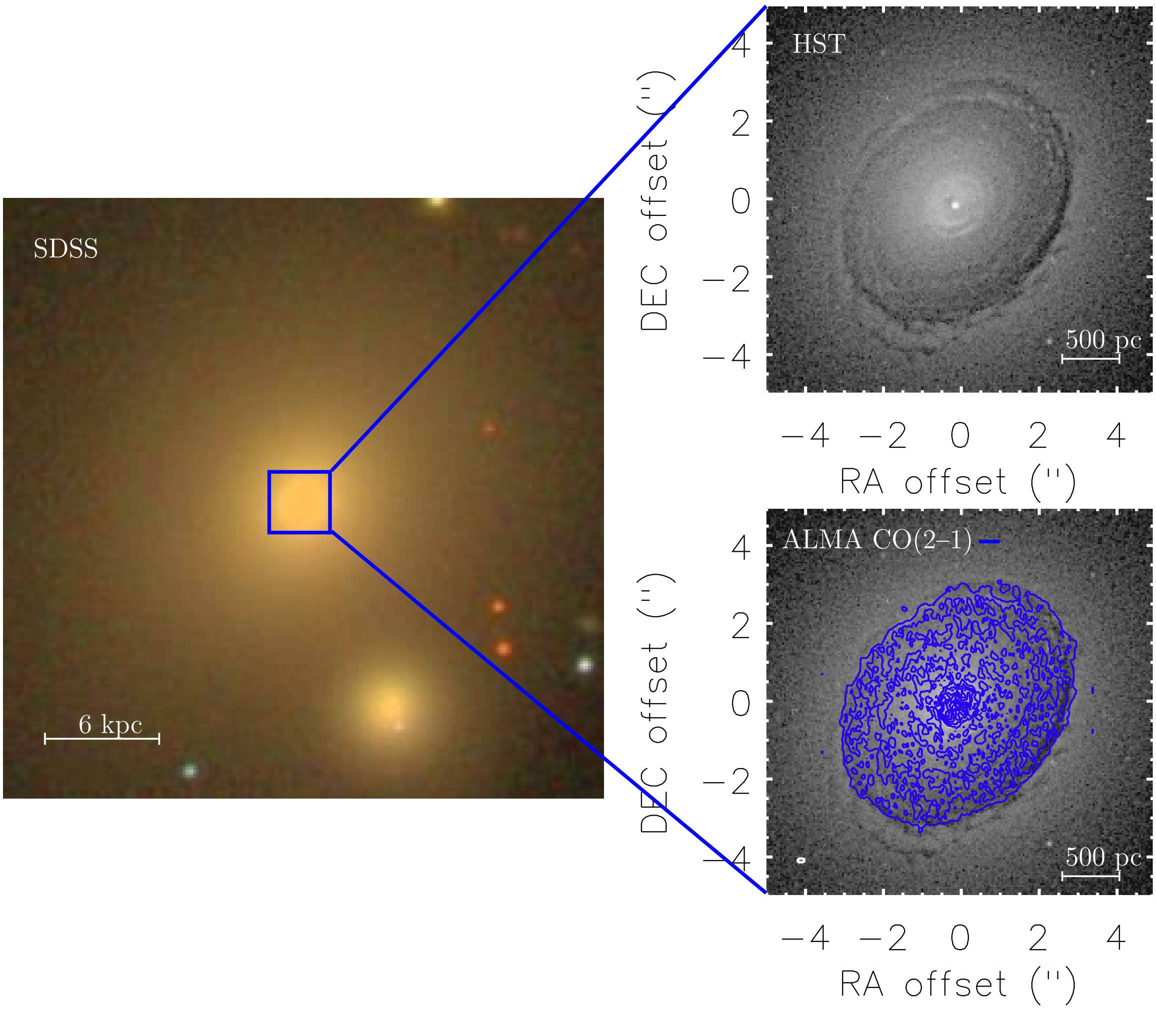

Figure 3.1. *Left panel:* SDSS three-colour (*gri*) image of NGC 0383, $90'' \times 90''$ ($29 \times 29\,\mathrm{kpc}^2$) in size. *Right panel, top:* Unsharp-masked Hubble Space Telescope (*HST*) Wide-Field Planetary Camera 2 (WFPC2) F555W image of a $3.2 \times 3.2\,\mathrm{kpc}^2$ region around the nucleus (indicated in blue in the left panel), revealing a clear central dust disc. *Right panel, bottom:* As above, but overlaid with blue ^{12}CO(2–1) integrated intensity contours from the ALMA observations presented in this chapter. The synthesised beam ($0\farcs18 \times 0\farcs1$ or $58 \times 32\,\mathrm{pc}^2$) is shown as a (very small) white ellipse in the bottom-left corner. The molecular gas disc coincides with the dust disc.

I then used the COMMON ASTRONOMY SOFTWARE APPLICATIONS (CASA; McMullin et al. 2007) package to combine the two configurations and image the resultant visibilities. A three-dimensional RA-Dec.-velocity data cube was produced with a binned channel width of $10\,\mathrm{km\,s^{-1}}$. To balance spatial sampling and resolution, pixels of $0\farcs035\times0\farcs035$ were chosen, yielding approximately 5 pixels across the synthesised beam major axis.

The data presented here were produced using Briggs weighting with a robust parameter of 0.5, yielding a synthesised beam full width at half-maximum (FWHM) of $\theta_{\mathrm{maj}} \times \theta_{\mathrm{min}} \approx 0\farcs18 \times 0\farcs1$ at a position angle of $6\fdg6$. The corresponding spatial resolution is $\approx 58 \times 32\,\mathrm{pc}^2$, so that the predicted R_{SOI} is well resolved with about 2 synthesised beams, i.e. $R_{\mathrm{SOI}} / \sqrt{\theta_{\mathrm{maj}} \times \theta_{\mathrm{min}}} = 1.9$. Continuum emission was detected, measured over the full line-free bandwidth, and then subtracted from the data in the *uv*–plane using the CASA task UVCONTSUB. The achieved continuum root mean square (rms) noise is $35\,\mu\mathrm{Jy\,beam^{-1}}$. The continuum-subtracted dirty cube was cleaned (see Högbom 1969 for the CLEAN procedure) in interactively-identified regions of source emission in each channel, to a threshold equal to the rms noise of the dirty channels. The clean components were then added back and re-convolved using a Gaussian beam of FWHM equal to that of the dirty beam. This produced the final, reduced and fully calibrated $^{12}\mathrm{CO}(2\text{–}1)$ data cube of NGC0383, with an rms noise level of $0.4\,\mathrm{mJy\,beam^{-1}}$ in each $10\,\mathrm{km\,s^{-1}}$ channel.

3.2.2 LINE EMISSION

The final data products used in this chapter were created from the clean, fully calibrated data cube. Zeroth moment (integrated intensity), first moment (mean velocity), and second moment (velocity dispersion) maps were created using a masked moment technique (e.g. Dame, 2011). The mask was generated by taking a copy of the clean cube and smoothing it, first spatially using a Gaussian with FWHM equal to that of the synthesised beam, and then Hanning-smoothing in velocity. The mask selects pixels with an amplitude in the smoothed cube greater than 0.8 times the rms of the unsmoothed data cube. The moments, shown in Fig. 3.2, are made from the original un-smoothed cube with the mask applied. I note that the masking procedure is only used when creating the moment maps, whilst the fitting is performed on the whole unmasked cube.

A regularly rotating and symmetric molecular gas disc is clearly detected, with no evidence that the disc is disturbed by the strong AGN jets. The disc extends $\approx 4'' \times 6''$ in projection ($\approx 1.4 \times 1.6\,\mathrm{kpc}^2$). There is a slight dip in flux at the centre of the zeroth moment, partially due to the masking procedure used in making the moment maps removing low surface brightness emission spread over a large number of channels close to the central SMBH. This hole becomes much less significant when a simple clipping procedure is used,

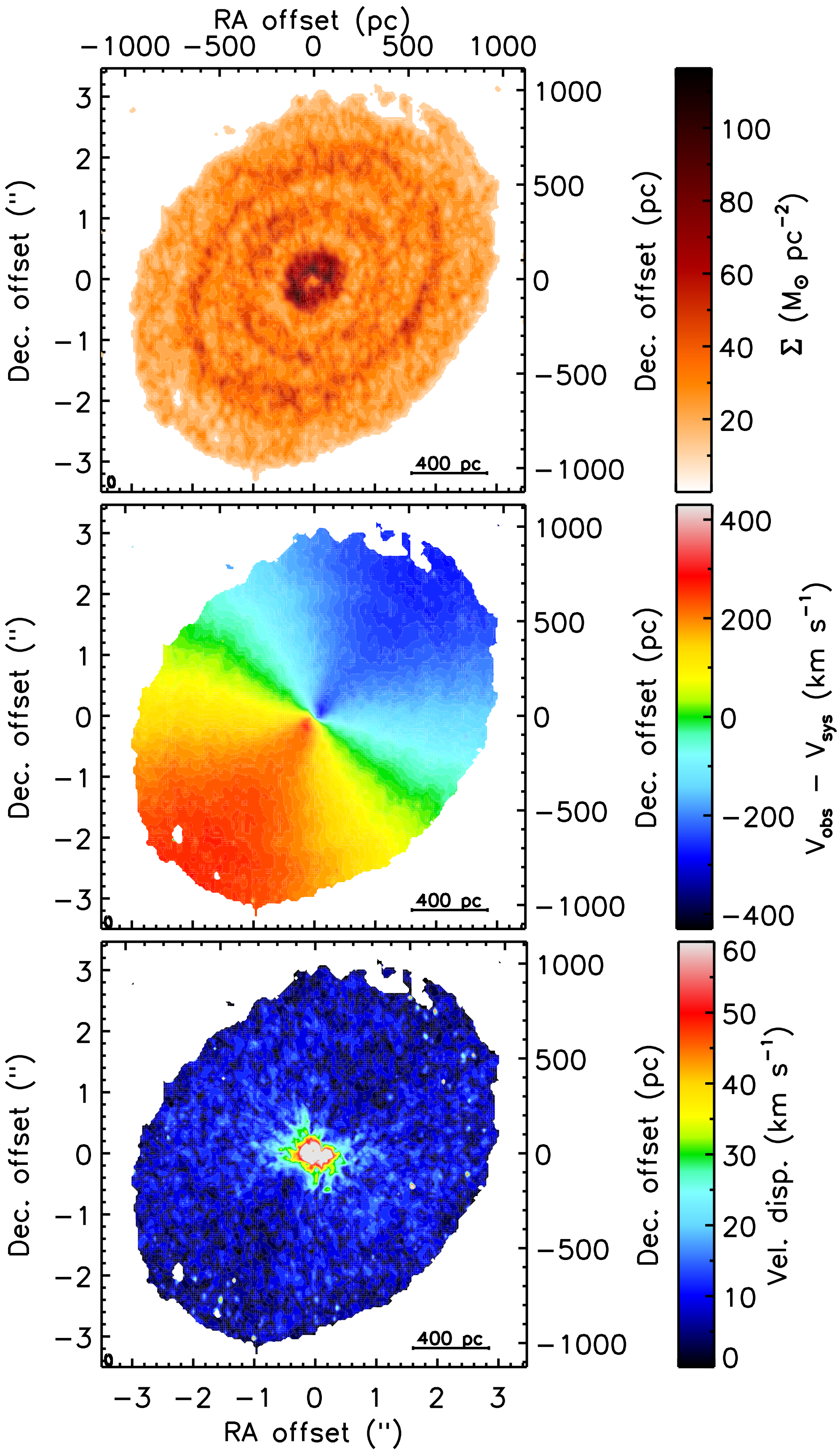

Figure 3.2. ^{12}CO(2–1) moment maps of NGC 0383. *Top panel:* moment zero (integrated intensity) map, assuming conversion factor CO-to-H_2 $\alpha_{CO} = 4.8\,M_\odot\,(K\,km\,s^{-1})^{-1}\,pc^{-2}$. *Central panel:* moment one (intensity-weighted mean velocity) map. *Bottom panel:* moment two (intensity-weighted velocity dispersion) map. The ellipse at the bottom-left shows the synthesised beam ($0\farcs18 \times 0\farcs1$) and the positions are from RA= $01^h07^m24\fs95$, Dec.= $+32^\circ24'45\farcs15$.

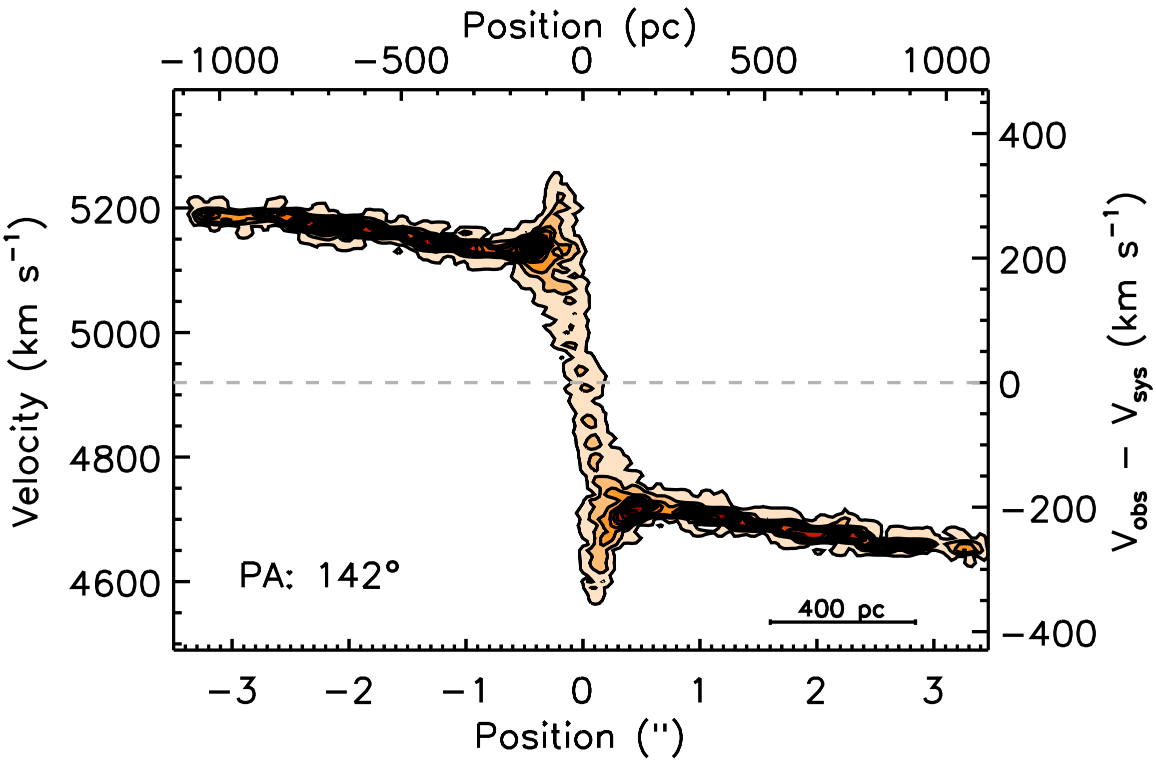

Figure 3.3. Major-axis PVD of NGC 0383 with the smooth mask applied. The SMBH signature is clearly visible and dominant at radii less than 0.″5. The rotation of the outer disc ($\gtrsim$ 0.″5) is very regular and relaxed. The dashed line shows the systemic velocity $V_{sys} = 4925 \pm 4$ km s^{-1}. The positions are from RA= 01^{h}07^{m}24.^{s}95, Dec.= +32°24′45.″15.

although this does increase the noise. I again note that the masking is only used for making the moment maps and the subsequent fitting is performed on the unmasked cube. The enhanced velocities around the centrally located SMBH are obvious in both the first moment map and the major-axis position-velocity diagram (PVD; Fig. 3.3), the latter constructed by summing pixels within a 5-pixel wide (0.″175) pseudo-slit at a position angle of 142°. The position angle used here and derived from the CO observations is reasonably consistent with the optical position angle as listed in the NASA/IPAC Extragalactic Database (NED)* of ≈ 150°. The moment one colourbar and PVD right-hand velocity axis are the observed line-of-slight velocity minus the systemic velocity of $V_{sys} = 4925 \pm 4$ km s^{-1} derived in Section 3.3.2. The large velocity dispersion observed at the centre of Fig. 3.2 is primarily due to beam smearing.

Fig. 3.4 shows the ^{12}CO(2–1) integrated spectrum, made by integrating over a 6″×6″ (1.9 × 1.9 kpc^2) area of the clean cube, thus encompassing the entire disc. It clearly shows the double-horn shape of a rotating disc, as also observed by Lim et al. (2000) in both CO(1–0) and CO(2–1) and Okuda et al. (2005) in CO(1–0) only. The total CO(2–1)

*https://ned.ipac.caltech.edu

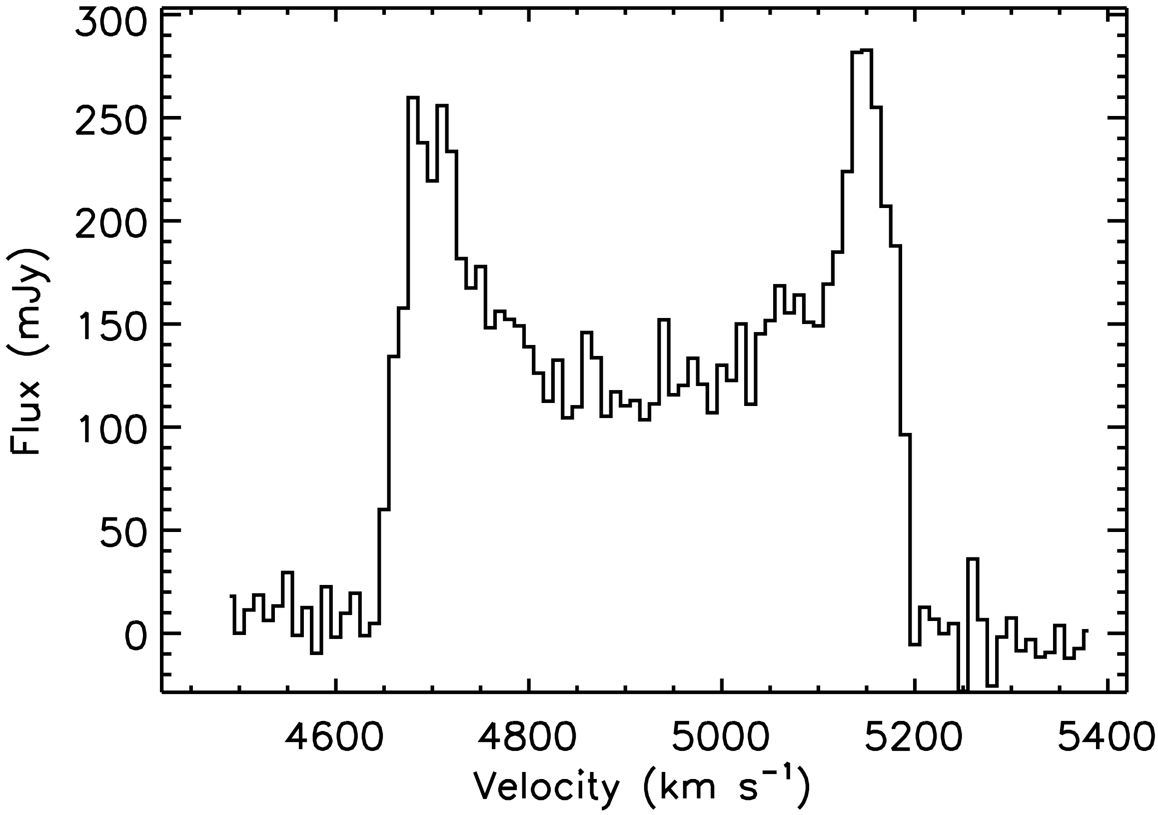

Figure 3.4. ^{12}CO(2–1) integrated spectrum of NGC 0383, showing the clear double-horned shape of a rotating disc.

flux is 87.1± Jy km s^{-1} (also ±8.7 10 percent systematic flux calibration uncertainty).

For this measurement, I want high spatial resolution data and hence use long-baseline interferometric observations. Incomplete *uv*–plane coverage can thus lead to some flux being resolved out. To check the scale of this problem, I compare the integrated flux derived from the CO(2–1) observations presented in this chapter with that of Ocaña Flaquer et al. (2010), obtained with the 30-m IRAM single-dish telescope. Their CO(2–1) flux is 74.4 ± 2.8 Jy km s^{-1}. As I retrieve slightly more flux than this, and the entire molecular gas disc of NGC 0383 fits within the primary beam of the 30-m telescope, it is unlikely that I resolve out flux in the observations presented here. The lower flux of the single-dish observations may be due to pointing and/or flux calibration errors.

Comparing the CO(2–1) flux measured here of 87.1 Jy km s^{-1} to that of the CO(1–0) line (29.8 Jy km s^{-1}; Ocaña Flaquer et al. 2010), I find a CO(2–1)/CO(1–0) ratio of 0.73 after converting to beam temperature units (K km s^{-1}). This ratio is very similar that found by Saintonge et al. (2017) in their mass-selected sample of local galaxies and within the range found by Leroy et al. (2013) for nearby star-forming disc galaxies, indicating the molecular gas in NGC 0383 is similar to that in other local galaxies. The detection of CO line emission provides information about the cold gas mass distribution, that is later incorporated into the modelling used in this chapter (in addition to the kinematics themselves).

3.2.3 CONTINUUM EMISSION

As mentioned previously, NGC 0383 hosts a radio-loud AGN. I detect a continuum point source at the kinematic centre of the galaxy, with a total integrated intensity of 65.2 ± 0.1 mJy at a central frequency of 235.33 GHz. Adding to the flux presented here to those tabulated in the NED† at millimetre and radio wavelengths, I constructed a radio–sub-mm spectral energy distribution (SED), shown in Fig. 3.5. Our data point, shown by the cyan diamond, agrees well with previous observations. The literature data generally encompass emission from both the nucleus and the jet, but it is likely that it is the nucleus that causes the observed variability (i.e. the few data points well below the red best-fitting line in Fig. 3.5). Nevertheless, the data are fitted well with a simple power law for the flux F as a function of frequency ν ($F_\nu \propto \nu^\alpha$), with a power-law index $\alpha = -0.66 \pm 0.03$ (the red line shown in Fig. 3.5). This index value (≈ -0.7) is typical of a radio galaxy dominated by synchrotron radiation, as expected here from the prominent AGN jets (e.g. MacDonald et al. 1968; Bridle & Perley 1984; Laing & Bridle 2002).

Despite the prominence of the AGN jets, the extreme regularity of the molecular

† `https://ned.ipac.caltech.edu`

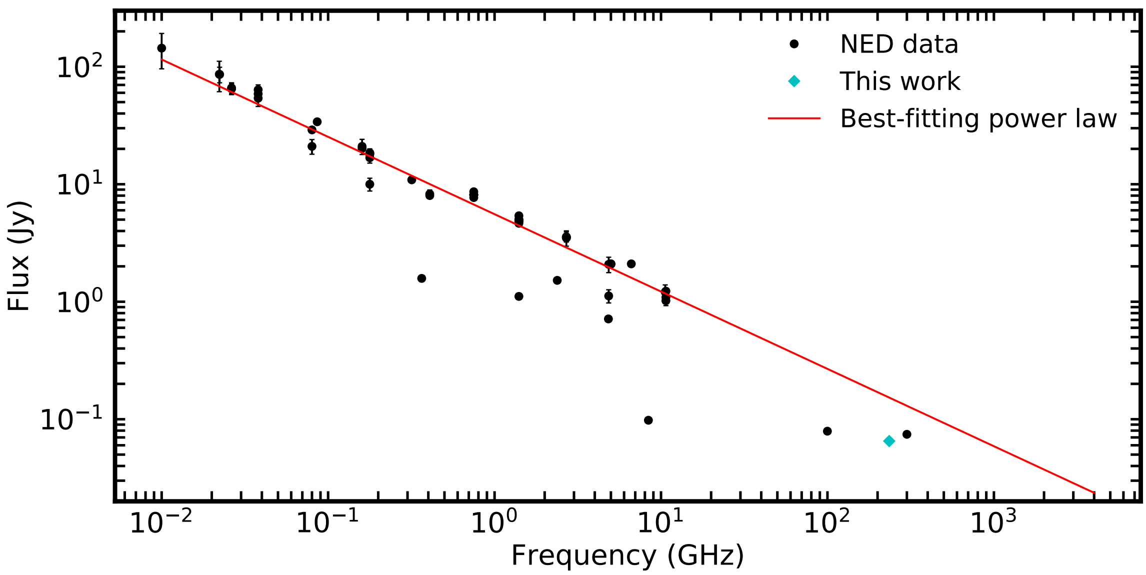

Figure 3.5. Spectral energy distribution of NGC 0383 from radio to mm wavelengths, constructed using data from NED (black circles) and the continuum flux measurement presented in this chapter (cyan diamond). A best-fitting power law with slope -0.66 is overlaid in red. Error bars are plotted for all points but most are smaller than the symbol used.

gas distribution and kinematics (Fig. 3.2) indicates that the radio AGN activity does not directly disturb the gas disc. Our ability to model the disc motions and estimate the SMBH mass is thus unaffected.

3.3 DYNAMICAL MODELLING

The method I use to estimate the SMBH mass is described in detail in Davis et al. (2017) and was used in the previous WISDOM papers, but I summarise the specifics for modelling NGC 0383 in this section. I make use of the publicly available KINEMATIC MOLECULAR SIMULATION (KINMS)[‖] mm-wave observation simulation tool of Davis et al. (2013a) to create models of the data cube. KINMS uses input information about the gas distribution and kinematics, including a circular velocity curve. Applying observational effects such as beam smearing and velocity binning, KINMS then creates a simulated data cube that can be directly compared to the observed data cube. The model parameters are incrementally driven towards the best-fitting values by a Markov chain Monte Carlo (MCMC) method. The MCMC algorithm fully samples the χ^2 hyper-volume to estimate the posterior distributions and hence uncertainties on the best-fitting values.

3.3.1 MASS MODEL

I use an axisymmetric model of the stellar light distribution to derive the circular velocity curve of the galaxy. I assume that the stellar mass dominates the potential in the inner parts of the galaxy: the molecular gas mass density is negligible in this system (see Section 3.4.2), whilst dark matter is usually unimportant at small radii, as shown by e.g. Cappellari et al. (2013). Even if this latter assumption is incorrect, if the dark matter were distributed identically to the stellar mass in the inner parts of the galaxy, it would simply lead to a higher mass-to-light ratio and would not affect the best-fitting SMBH mass. If dark matter were to contribute significantly and be distributed differently to the stellar mass, I would then find evidence for a significant mass-to-light ratio gradient (I find marginal evidence for a small mass-to-light ratio gradient in Section 3.3.2).

To model the luminous mass I perform a Multi-Gaussian Expansion (MGE; Emsellem et al. 1994), using the method implemented in the MGE_FIT_SECTORS Interactive Data Language (IDL) software[‡] version v4.12 of Cappellari (2002). I use a combined *Hubble Space Telescope (HST)* Near Infrared Camera and Multi-Object Spectrometer (NICMOS) F160W and Two-Micron All-Sky Survey (2MASS) *H*-band image. This combined image allows us to model the stellar light with a sum of two-dimensional (2D) Gaussians up to a radius of $20''$ (6.4 kpc), the *HST* image being used exclusively for the inner $\approx 4''$ (1.3 kpc) in radius because of its superior angular resolution. To minimise the effect of dust attenuation on the mass-to-light ratio, the *HST* image was masked over part of its lower-right limb (see the cyan region in Fig. 3.6, top panel). The resulting MGE model is shown in Fig. 3.6, with the values of each Gaussian listed in Table 3.1 (these values have not been deconvolved).

The circular velocity curve is then calculated by the MGE_CIRCULAR_VELOCITY procedure[‡], by first analytically deprojecting the 2D Gaussians to a three-dimensional (3D) mass distribution, calculating the potential, and hence the circular velocity. The above procedure uses a mass-to-light ratio of $1\,\mathrm{M_\odot}\,/\,\mathrm{L_{\odot,F160W}}$. The circular velocity is then multiplied element-wise by the square root of the actual mass-to-light ratio adopted (the mass-to-light ratio is a free parameter in the fitting, explained below), and a point mass representing the SMBH is added in the centre. The functional form of the mass-to-light ratio is fully explained in Section 3.3.2. However, I will show in Section 3.4 that, in the case of NGC 0383, the SMBH mass is essentially independent of the stellar mass-to-light ratio.

[‡]`http://purl.org/cappellari/software`, part of the Jeans Anisotropic MGE (JAM) dynamical modelling package of Cappellari (2008).

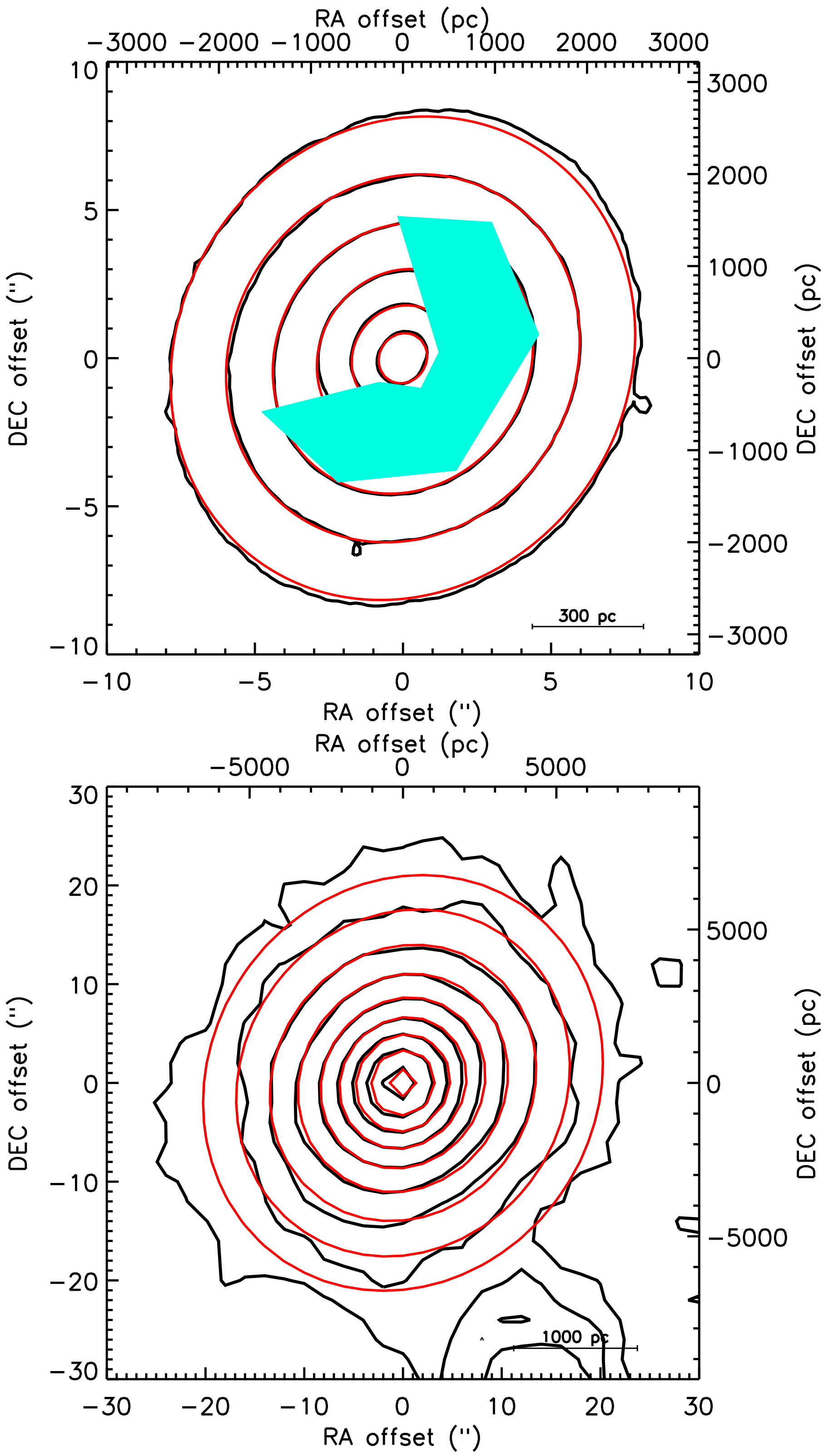

Figure 3.6. MGE model of NGC 0383 (red contours) overlaid on the *HST* NICMOS F160W image (black contours, top panel) and the 2MASS *H*-band image (black contours, bottom panel). In the *HST* image (top panel), the area masked due to dust is shown in cyan. A foreground star, bottom-right in the 2MASS image (bottom panel), is outside the fit radius and does not affect the MGE. The positions are from RA= $01^{\mathrm{h}}07^{\mathrm{m}}24^{\mathrm{s}}.95$, Dec.= $+32^{\circ}24'45''.15$.

Table 3.1. MGE best-fitting Gaussians (not deconvolved).

I ($\mathrm{L}_{\odot,\mathrm{F160W}}\ \mathrm{pc}^{-2}$)	σ_j ($''$)	q_j
12913.05	0.0682	0.91
3996.80	0.823	0.9
5560.84	1.13	0.93
4962.29	2.63	0.9
2877.92	4.98	0.9
957.88	12.7	0.9

Notes: For each Gaussian component, column 1 lists its F160W central surface brightness, column 2 lists its standard deviation (width), and column 3 lists its axis ratio.

3.3.2 BAYESIAN ANALYSIS

I use an MCMC method to find the posterior distribution of the model best fitting the NGC 0383 data, making use of the IDL KINMS_MCMC** code of Davis et al. (2013b, 2017) that easily interfaces with the KINMS simulation tool to create new models and calculate and maximise the likelihood. A single fit was made to the whole clean data cube, with one hundred thousand iterations. All parameters had flat priors in linear space within specified physical limits, as listed in Table 3.2, the only exception being the SMBH mass prior that was flat in log-space. The observational errors were taken to be the rms of the data cube in line-free channels, assumed to be constant throughout the cube.

The molecular gas disc of NGC 0383 has a slight nuclear ring and outer spiral/ring structures that make assuming a smoothly varying monotonic radial profile inappropriate. Rather than constructing an arbitrarily complicated parametrisation of the radial gas distribution, I adopt instead the observed gas distribution as an input to the KINMS model. Using the SKYSAMPLER†† tool (Smith et al., 2019), I thus sample the de-convolved CLEAN components produced by the CASA task to generate a set of gas particles that exactly replicate the surface brightness profile. These particles are then used as an input into KINMS, with the three-dimensional central position, inclination and position angle of the gas disc as free parameters. The centre is initially assumed to be at the centre of the continuum emission (RA= $01^{\mathrm{h}}07^{\mathrm{m}}24\overset{\mathrm{s}}{.}95$, Dec.= $+32^{\circ}24'45\overset{''}{.}15$) and the velocity of the central channel of the cube ($V_{\mathrm{helio,radio}} = 4940\,\mathrm{km\,s^{-1}}$). With no evidence to the contrary, I use the thin disc approximation for NGC 0383.

I found that allowing a linearly varying radial mass-to-light ratio profile fits the data better than a single (constant) mass-to-light ratio. Initial fits used a single mass-to-light ratio for the whole disc, but this did not provide a good fit to the entire data cube. I therefore implemented the simplest model to account for this, a linearly varying mass-to-light ratio, defined as

$$M/L(R) = (M/L_{\rm outer} - M/L_{\rm inner})\left(\frac{R}{3\farcs5}\right) + M/L_{\rm inner}\,, \tag{3.1}$$

where R is the radius and the inner ($M/L_{\rm inner}$) and outer ($M/L_{\rm outer}$) mass-to-light ratios are free parameters of the fit performed in this chapter. The inner value is set at the centre of the disc ($R = 0''$) with the outer edge at $R = 3\farcs5$ and a flat mass-to-light ratio beyond that.

Here I adopt the usual definition of 1σ (3σ) uncertainties as the 68.3 % (99.7 %) confidence intervals of the Bayesian posteriors found from the MCMC. Table 3.2 lists the best-fitting value of each model parameter, along with its formal uncertainties.

As discussed in Section 3.2 of van den Bosch & van de Ven (2009), when working with very large data sets the statistical uncertainties can be severely underestimated due to the dominance of the systematic uncertainties. Accordingly, they suggest an approximate correction to account for the systematic uncertainties, by rescaling the $\Delta\chi^2$ (with respect to the minimum χ^2, $\chi^2_{\rm min}$) required to define a given confidence level by the standard deviation of the χ^2, namely $\sqrt{2(N-P)} \approx \sqrt{2N}$, where N is the number of constraints ($\approx 5.9 \times 10^6$) and P is the number of inferred model parameters (10). This sets the 68.3 % (99.7 %) confidence level at $\chi^2_{\rm min} + \sqrt{2N}$ ($\chi^2_{\rm min} + 3\sqrt{2N}$). Applying this rescaling results in significantly larger uncertainties on the fitted parameters, which are likely to be more physically plausible. The same method was applied and discussed in detail by Smith et al. (2019), and I use it here in the MCMC fitting of NGC 0383. The corner plots and one-dimensional marginalisation of each model parameter are shown in Fig. 3.7.

Correlations are induced between pixels due to the synthesised beam, that can be corrected for by accounting for the induced covariance. However, the effect of this covariance on the MCMC uncertainties is negligible compared to the rescaling of the χ^2 discussed above; hence, I did not include the covariance matrix in the calculations which this measurement are based on.

I find strong evidence for an SMBH, of mass $(4.2 \pm 0.7) \times 10^9$ $\mathrm{M}_\odot$ (3σ uncertainty). The best-fitting model's PVD is shown in the middle panel of Fig. 3.8, as the blue contours overlaid on the data. It has a reduced χ^2 of 1.01. Fig. 3.8 shows that a kinematic model with a dark massive object at the centre is the only model to fully describe the data. In the left panel the SMBH has been removed and the model no longer reproduces the data. The right panel of Fig. 3.8 shows the best-fitting model with the mass-to-light ratio set to zero, i.e. no stellar mass, demonstrating the that SMBH mass dominates in the inner $0\farcs5$ (as the fit is still very good in that region). In this figure both the model and the data have a smooth mask applied to mitigate noise in the plot and use the same contours.

Table 3.2. Best-fitting parameters with uncertainties from the MCMC fits.

Parameter	Search range	Best fit	1σ uncertainty	3σ uncertainty
SMBH mass ($\log(\mathrm{M_\odot})$)	8.70–9.95	9.63	0.04	0.08
Stellar M/L inner ($\mathrm{M_\odot/L_{\odot,F160W}}$)	0.01–10	2.78	0.21	0.61
Stellar M/L outer ($\mathrm{M_\odot/L_{\odot,F160W}}$)	0.01–10	2.36	0.12	0.33
Position angle (°)	112–172	142.20	0.04	0.10
Inclination (°)	26–89	37.58	1.67	3.48
Velocity dispersion ($\mathrm{km\,s^{-1}}$)	0–15	8.32	0.72	2.11
Nuisance parameters				
Integrated intensity ($\mathrm{Jy\,km\,s^{-1}}$)	5–200	74.60	4.15	9.79
Centre X offset (″)	-5–5	-0.00	0.01	0.03
Centre Y offset (″)	-5–5	-0.05	0.02	0.04
Centre velocity offset ($\mathrm{km\,s^{-1}}$)	-50–10	-15.16	1.37	3.63

Note: The X and Y offsets are measured with respect to the location of the unresolved continuum point source, RA= $01^{\mathrm{h}}07^{\mathrm{m}}24\overset{\mathrm{s}}{.}96$ and Dec. $= +32°24'45\overset{''}{.}11$. The velocity offset is measured with respect to the central channel of the cube ($V_{\mathrm{helio,radio}} = 4940\,\mathrm{km\,s^{-1}}$). The best-fitting centre velocity offset thus defines a systemic velocity of $V_{\mathrm{sys}} = 4925 \pm 4\,\mathrm{km\,s^{-1}}$.

The best-fitting F160W-band mass-to-light ratio decreases linearly from $2.8 \pm 0.6\,\mathrm{M_\odot/L_{\odot,F160W}}$ in the centre to $2.4 \pm 0.3\,\mathrm{M_\odot/L_{\odot,F160W}}$ at the outer edge of the disc (both 3σ uncertainties). The spatial centre (as indicated by the X and Y offsets) is consistent with the unresolved continuum source to within the beam size.

3.4 DISCUSSION

In this chapter I have presented ALMA ^{12}CO(2–1) observations of NGC 0383 showing a relaxed gas disc (Section 3.2). The data clearly show the kinematic signature of a massive dark object, with a mass of $(4.2 \pm 0.7) \times 10^9\,\mathrm{M_\odot}$ (3σ uncertainty) measured through dynamical modelling (Section 3.3).

3.4.1 UNCERTAINTIES

The uncertainties associated with an SMBH mass derived through the molecular gas technique are discussed extensively in the previous papers using this method. Each paper builds from the last and focuses on the sources of uncertainty that are relevant to each galaxy. In particular, Smith et al. (2019) discussed properly constraining the mass-to-light ratio and inclination. As I resolve the SMBH R_{SOI} in NGC 0383 in this case the mass measurement presented here is essentially independent of the mass-to-light ratio (see

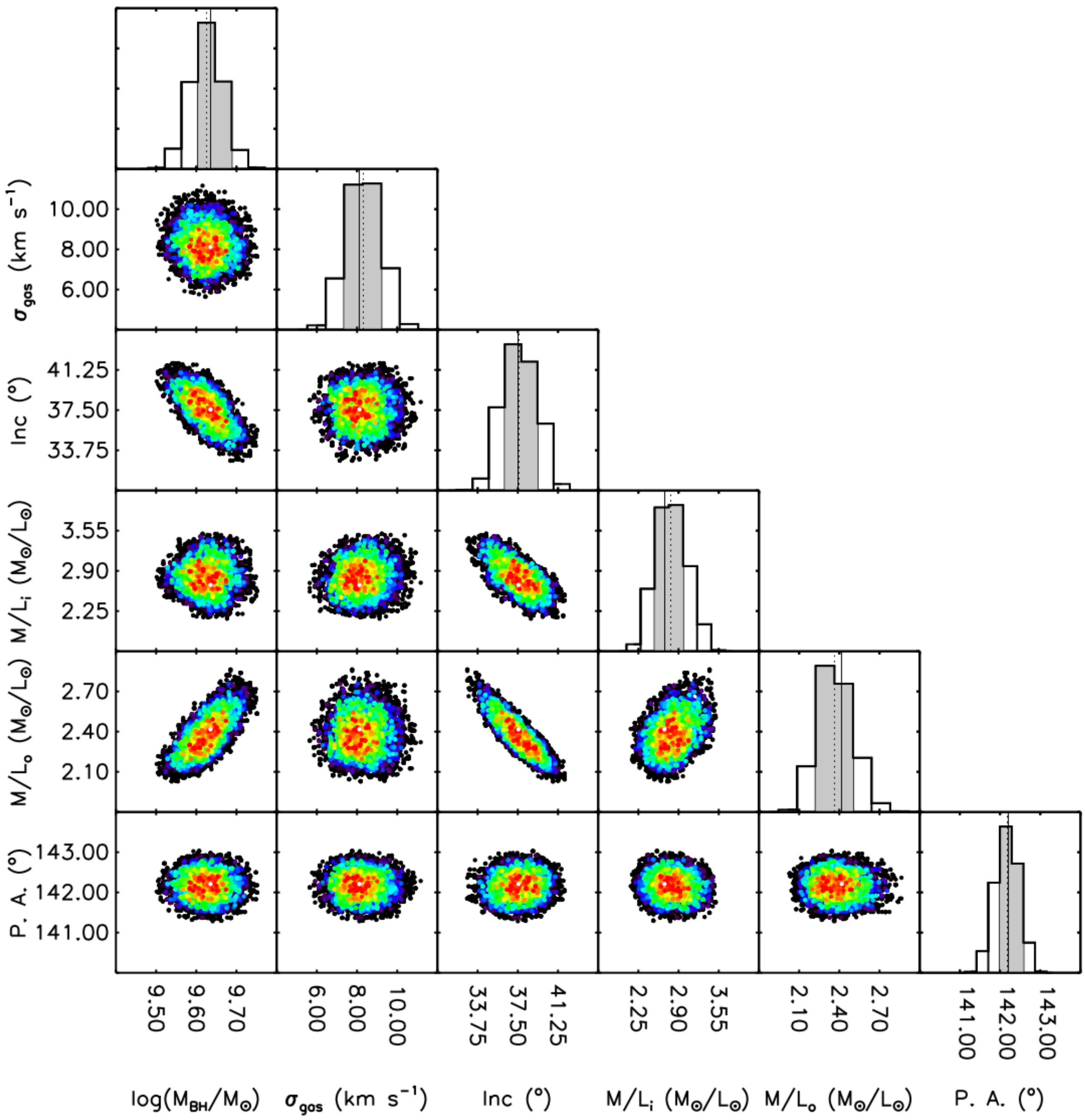

Figure 3.7. Corner plots showing covariances between the model parameters, for the non-nuisance parameters. The colours represent increasing confidence intervals from 68.3 % (red, 1σ) to 99.7 % (blue, 3σ). The white dots show the χ^2_{min} values. Covariances are present between the SMBH mass and outer stellar mass-to-light ratio, SMBH mass and inclination, and inclination and both stellar mass-to-light ratios. In the SMBH mass cases, this is exaggerated by plotting linear against logarithmic scales. Histograms show the one-dimensional marginalised posterior distribution of each model parameter. The shaded regions indicate the 68 % (1σ) confidence intervals. The black dashed lines show the median values and the black solid lines the χ^2_{min} values.

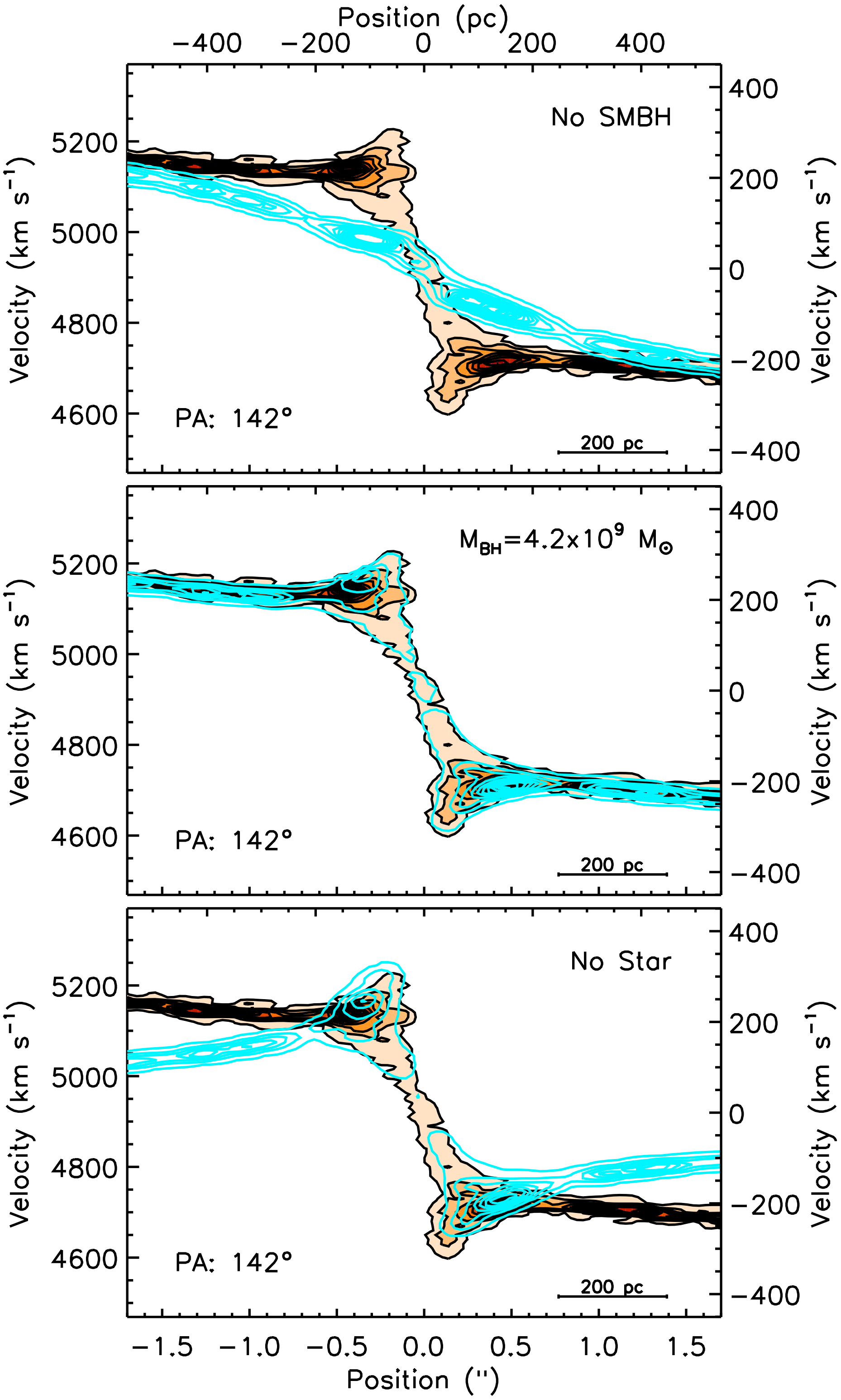

Figure 3.8. Observed PVD of NGC 0383 with the smooth mask applied (orange contours) with the best-fitting model's PVD overplotted (blue contours). *Top panel:* with no SMBH mass. *Central panel:* with the best-fitting SMBH mass and mass-to-light ratio. *Bottom panel:* with the mass-to-light ratio set to zero, i.e. no stellar contribution. The positions are from RA= $01^h07^m24\overset{s}{.}95$, Dec.= $+32°24'45\overset{''}{.}15$.

Section 3.4.2). Accurately determining the inclination, however, remains important. Our choice to apply the χ^2 scaling (discussed in Section 3.3.2) allows us to retrieve more physically meaningful estimates of the inclination uncertainties. As NGC 0383 is fairly face-on ($i \approx 38^\circ$) these uncertainties dominate the error budget, through the degeneracy between inclination and SMBH mass (see Fig. 3.7).

Other potential sources of uncertainty arise from the assumption that the molecular gas is dynamically cold and rotating on circular orbits. The velocity dispersion of the gas is consistently small ($\sigma_{\rm gas} < 10\,{\rm km\,s^{-1}}$), indicating the disc is nearly perfectly rotationally supported ($V_{\rm rot}/\sigma_{\rm gas} \gtrsim 40$, where $V_{\rm rot}$ is the deprojected rotation velocity of the gas in the nearly flat portion of the rotation curve; see e.g. Fig. 3.3). Despite this, some non-circular motions do appear to be present. The velocity residuals (Fig. 3.9; data moment 1 minus best-fitting model moment 1) show the same spiral/ring structures noted in the moment zero (Fig. 3.2), indicating that material may be flowing along these arms (potential fuelling the AGN). The larger velocity residuals near the centre are due to the intensity weighting when creating the moment 1 map. However, the dominance of the SMBH in the central regions (see Fig. 3.10) indicates that non-circular motions are unlikely to significantly affect the derived SMBH mass.

All these uncertainties are small, and in any case they are dwarfed by that on the distance measurement. This uncertainty is $\approx 15\,\%$ (i.e. $66.6 \pm 9.9\,{\rm Mpc}$), from the use of the Tully–Fisher relation in Freedman et al. (2001) to estimate the distance. The SMBH mass measurement scales linearly with the distance adopted, and as is customary I do not include the distance uncertainty in the results presented here.

3.4.2 MASS-TO-LIGHT RATIO INFLUENCE

The posterior distribution between SMBH mass and mass-to-light ratio shows a strong covariance (see Fig. 3.7, middle panels of the leftmost column), although this is exaggerated by plotting linear against logarithmic scales. The correlation present is contrary to the expected anticorrelation, and it may be a product of the SMBH mass–inclination and mass-to-light ratio–inclination correlations. By allowing the inclination to vary during the fit, the correlation between mass-to-light ratio and inclination dominates and induces correlations in other variables. See Smith et al. (2019) for a fuller discussion of this issue.

A simple calculation of the total mass enclosed from the circular velocity (and assuming spherical symmetry, i.e. $M_{<R} \propto V_{\rm rot}^2(R)/R$) allows us to determine how significant the stellar mass is as a function of radius in NGC 0383. Fig. 3.10 shows the enclosed stellar mass as a function of radius as well as the enclosed total mass, revealing that the stellar mass becomes significant only at a radius of $\approx 200\,{\rm pc}$. The $R_{\rm SOI}$ is calculated from

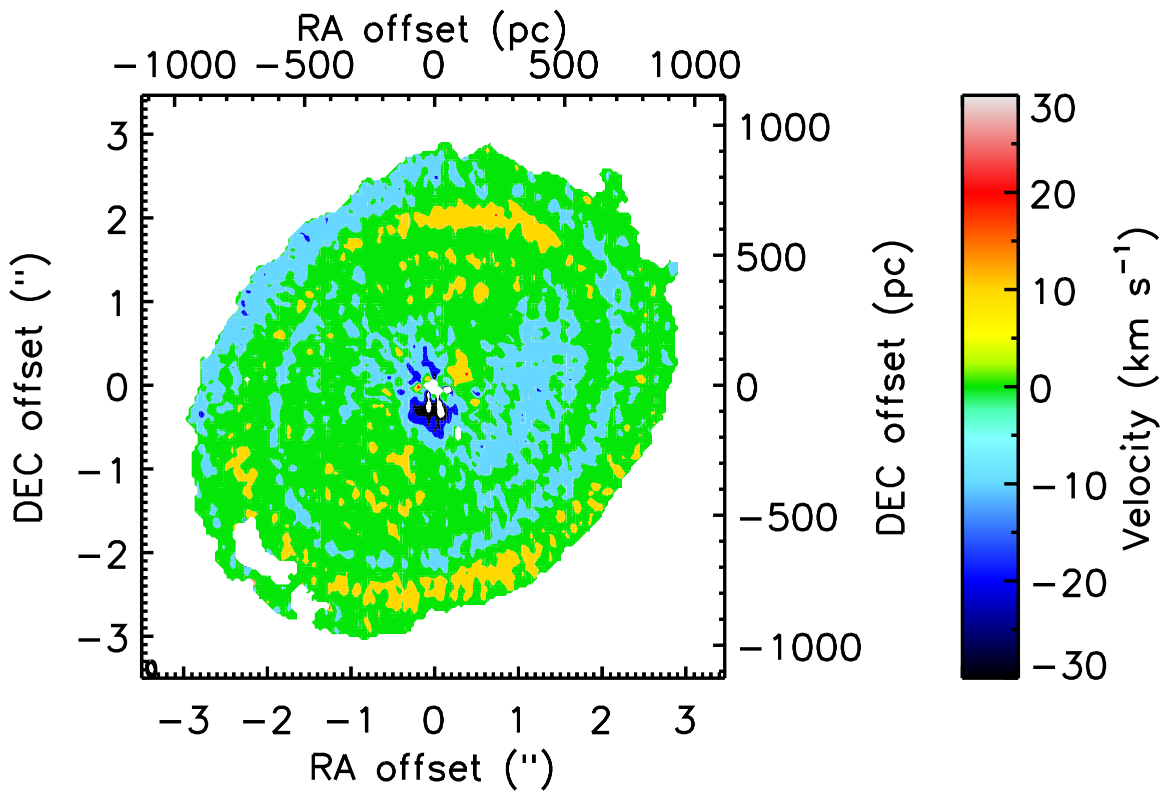

Figure 3.9. First moment (intensity-weighted mean velocity) residuals of NGC 0383, created by subtracting the first moment of the best-fitting model cube from the first moment of the data cube. The plot clearly shows the slight spiral features that could not be modelled by the axisymmetric mass model used here. Due to the simplicity of the model and weighting when creating the first moment, there are larger velocity residuals near the disc centre. The positions are from RA= $01^{\mathrm{h}}07^{\mathrm{m}}24\overset{\mathrm{s}}{.}95$, Dec.= $+32^{\circ}24'45\overset{''}{.}15$.

Equation 2.1 with our measurement of $M_{\rm BH}$ and $\sigma_{\rm e}$ from van den Bosch (2016). At $0\farcs13$ (i.e. one synthesised beam, 43 pc), the stellar mass is only $\approx 1\,\%$ of the mass enclosed at that radius, so is insignificant. The molecular gas disc mass at this radius is $\approx 10\,\%$ of the total enclosed mass, that is again small compared to the SMBH mass ($\approx 90\,\%$ of the total enclosed mass). This indicates that whilst the mass-to-light ratio (and assumed $X_{\rm CO}$) do have a covariance with the SMBH, their effect on the best-fitting value is very small and the SMBH mass is largely independent of them. The fact that the SMBH mass presented here is almost independent of the luminous mass model in turn leads to the very small uncertainties on $M_{\rm BH}$ compared to other works (indeed, the 3σ confidence interval in Fig. 3.7 is very narrow). It also gives us greater confidence in the measurement.

Although in NGC 0383 the SMBH dominates the total mass distribution within a few synthesised beams (i.e. angular resolution elements), this might not always be the case and in some instances the mass of the molecular gas disc itself may matter. In fact, even in NGC 0383, the molecular gas mass is larger than the stellar mass within one synthesised beam. This reinforces the importance of spatially resolved molecular gas data for SMBH mass measurements.

3.4.3 ESTIMATING $M_{\rm BH}$ FROM THE OBSERVED $R_{\rm SOI}$

In contrast to the detailed dynamical modelling of Section 3.3.2, I can make a crude estimate of the SMBH mass from the observed radius of the SMBH sphere of influence ($R_{\rm SOI}$). The SMBH $R_{\rm SOI}$ is defined as the radius within which the SMBH dominates the potential (see Equation 2.1). This radius can be determined from the observed PVD (Fig. 3.3) as the local minimum in the rotation curve (i.e. the transition point) between the SMBH-dominated Keplerian curve ($V_{\rm rot} \propto 1/\sqrt{R}$) and the stellar mass-dominated approximately flat rotation curve ($V_{\rm rot} \simeq$constant). By visual inspection, I estimate this occurs at a radius of $\approx 0\farcs7$ (≈ 225 pc; see Fig. 3.8). Using Equation 2.1 and $\sigma_{\rm e} = 239 \pm 16\,{\rm km\,s^{-1}}$ (van den Bosch, 2016) then yields $M_{\rm BH} \approx 3.0 \times 10^9\,{\rm M_\odot}$. Given that the SMBH $R_{\rm SOI}$ is so well resolved, this back-of-the-envelope estimate agrees well with the result presented above of $(4.2 \pm 0.7) \times 10^9\,{\rm M_\odot}$ (the latter also yielding an exact $R_{\rm SOI} = 316 \pm 60$ pc or $0\farcs98 \pm 0\farcs18$).

3.4.4 COMPARISON TO THE LITERATURE

An upper limit on the SMBH mass in NGC 0383 has previously been determined by Beifiori et al. (2009). Once scaled to the distance assumed here (66.6 Mpc from 63.4 Mpc) and inclination ($37\fdg6$ from 33°) this is $M_{\rm BH} = 1.1 \times 10^9\,{\rm M_\odot}$. Given that this is lower than the measurement presented here, it might indicate the presence of very disturbed ionised gas.

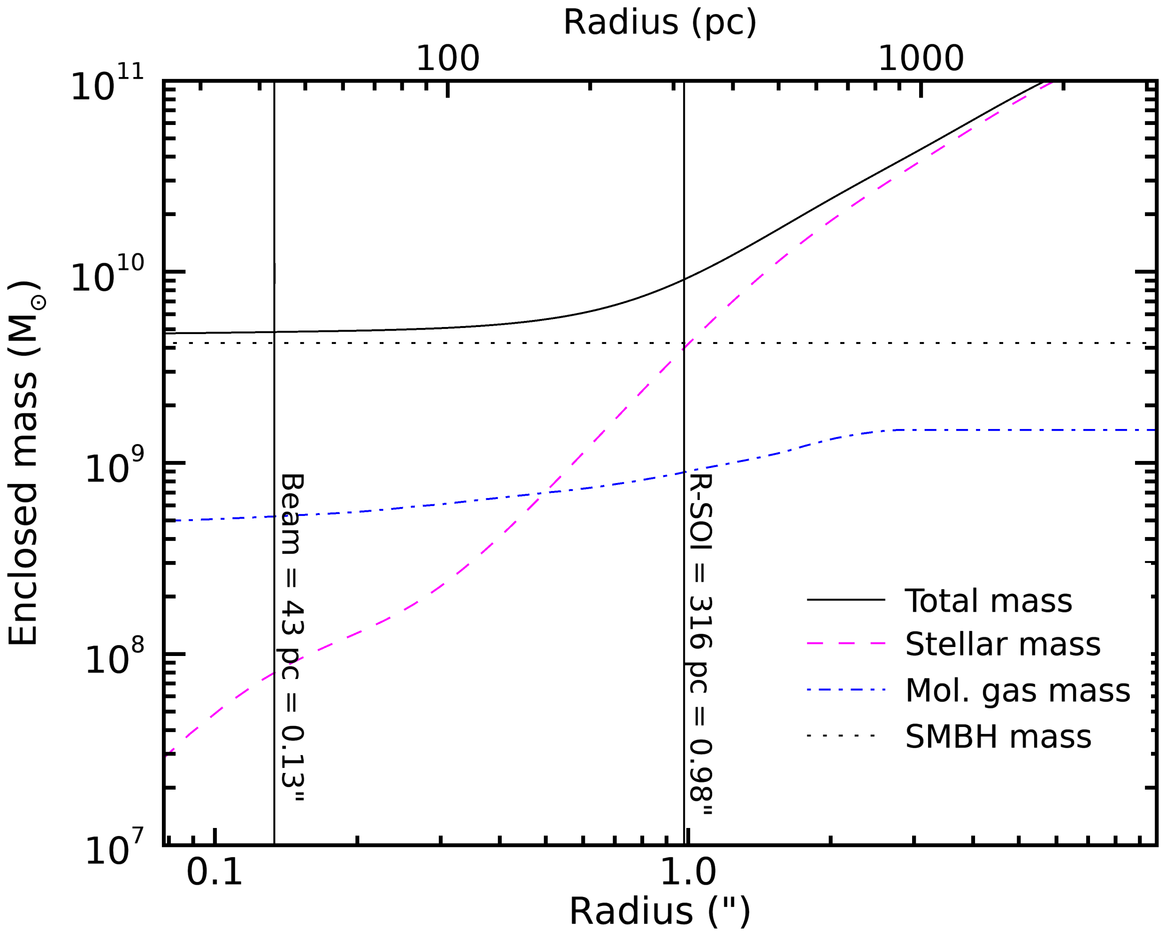

Figure 3.10. Cumulative mass profile of NGC 0383, showing the total mass (black solid line), SMBH mass (black dotted line), stellar mass (magenta dashed line), and molecular gas disc mass (blue dot-dashed line) enclosed as a function of radius. The vertical lines indicate the synthesised beam and measured R_{SOI}. At a radius of one synthesised beam, both the stellar mass and the molecular gas mass are insignificant (≈ 1 % and ≈ 10 % of the total mass, respectively). The positions are from RA$= 01^{\mathrm{h}}07^{\mathrm{m}}24\overset{\mathrm{s}}{.}95$, Dec.$= +32^{\circ}24'45\overset{''}{.}15$.

One of the tightest known correlations between SMBH mass and a host galaxy property is that with the stellar velocity dispersion, i.e. the $M_{\rm BH} - \sigma_{\rm e}$ relation (e.g. Gebhardt et al., 2000; Ferrarese & Merritt, 2000). I added the measurement presented here to the dynamical measurements and power-law fit of van den Bosch (2016) in Fig. 3.11, to see whether it also lies on this relation. The data of van den Bosch (2016) are shown in grey, whilst the measurement presented in this chapter for NGC 0383 is shown in blue. Other SMBH masses estimated using the molecular gas method are shown in red (Davis et al. 2013b; Onishi et al. 2015; Barth et al. 2016a,b; Davis et al. 2017; Onishi et al. 2017; Davis et al. 2018; Boizelle et al. 2019; Combes et al. 2019; Nagai et al. 2019; Smith et al. 2019). NGC 0383 has the largest SMBH mass estimated with molecular gas so far, and is on the upper edge of the scatter in the van den Bosch (2016) $M_{\rm BH}$-$\sigma_{\rm e}$ relation. If accurate, the low $\sigma_{\rm e}$ compared to the SMBH mass indicates NGC 0383 might be part of the so-called overmassive black hole population. NGC 0383 appears to have a slightly low $\sigma_{\rm e}$ compared to the SMBH mass which may give insight about its formation and evolution, other galaxies have also been found with overmassive black holes. Lim et al. (2000) discuss whether the AGN activity in NGC 0383 is the result of a gas-rich minor merger, with black hole accretion beginning soon after the merger event.

3.4.5 COMPARISON OF SPATIAL SCALES PROBED BY MOLECULAR GAS AND MEGAMASERS

Modelling megamaser dynamics is typically the most accurate method of measuring SMBH masses, due to the exquisite angular and spectral resolution usually achieved. The Keplerian rise I detect in the centre of NGC 0383 indicates that the data presented here reach very close to the SMBH. The connection between the accretion disc/torus region (where masers are typically found) and the outer molecular gas disc has only recently begun to be explored in any detail. It is thought that position angle mismatches are common between these two components, and tilted and counter-rotating accretion discs are frequently observed (e.g. recently by Imanishi et al., 2018; Combes et al., 2019). In contrast to this expectation, NGC 0383 seems to have a single, unwarped molecular disc extending from kiloparsec scale to well within its SMBH SOI.

I am able to estimate just how close to the SMBH the highest velocity molecular gas I detect here is. Equating the centrifugal and gravitational forces at a radius R and assuming the SMBH mass dominates the stellar mass within this radius, I obtain

$$R = \frac{GM_{\rm BH}}{V_{\rm c}^2}, \tag{3.2}$$

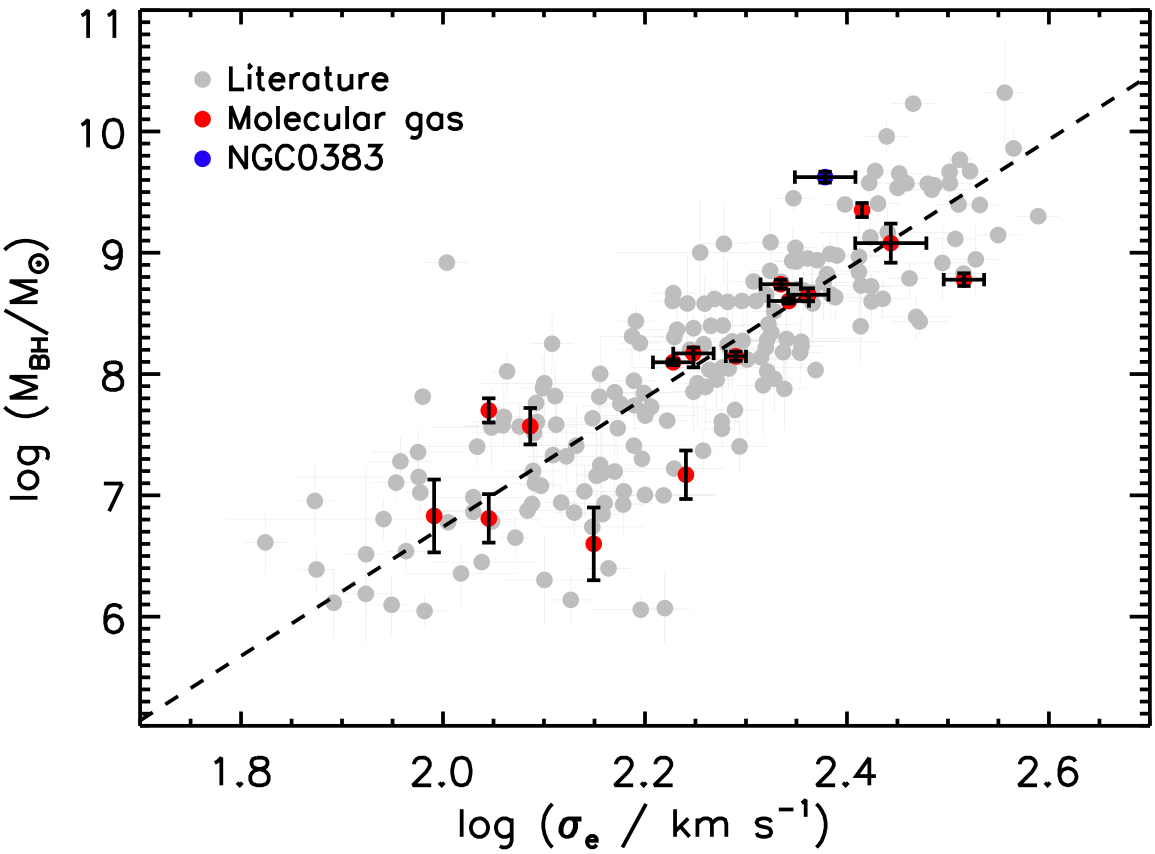

Figure 3.11. The $M_{\rm BH} - \sigma_{\rm e}$ relation from literature measurements (grey points and dotted line), as compiled by van den Bosch (2016). SMBH mass measurements using the molecular gas method are highlighted in red, whilst this measurement (NGC 0383) is in blue. For the molecular gas-derived SMBH masses, the error bars shown correspond to 1σ uncertainties.

where V_c is the circular velocity at R. If I normalise the radius by the Schwarzschild radius

$$R_{\rm Schw} \equiv \frac{2GM_{\rm BH}}{c^2}, \tag{3.3}$$

where c is the speed of light, and the circular velocity by c, I find

$$\frac{R}{R_{\rm Schw}} = \frac{1}{2}\left(\frac{V_c}{c}\right)^{-2}, \tag{3.4}$$

where interestingly the SMBH mass has dropped out. All rotationally supported discs around an SMBH should thus follow this unique relation, irrespective of the SMBH mass. Substituting $V_c = V_{\rm obs}/\sin(i)$, where $V_{\rm obs}$ is the observed line-of-sight velocity (along the galaxy major axis) and i the inclination, I obtain

$$\frac{R}{R_{\rm Schw}} = 0.5\times10^6\left(\frac{300\,{\rm km\,s^{-1}}\sin(i)}{V_{\rm obs}}\right)^2. \tag{3.5}$$

The maximum rotation velocity observed in NGC 0383 is $V_{\rm obs} \approx 350\,{\rm km\,s^{-1}}$ (the peak of the PVD in Fig. 3.3) and $i = 37\overset{\circ}{.}5$. The highest velocity molecular gas I detect therefore reaches $\approx 1.36\times10^5$ Schwarzschild radii.

Megamasers, although rare, are the current gold standard for dynamical SMBH mass measurements. Megamasers are thought to trace gas very close to the SMBH (in the accretion disc/torus), and as such they probe the gravitational field of the SMBH in a way that is unaffected by most outside sources. In addition, in the best cases, maser observations provide independent geometric distance estimates, vastly reducing the dominant systematic effect that plagues most SMBH mass measurements. Some of the earliest megamasers discovered were in NGC 4258 (Nakai et al., 1993; Herrnstein et al., 1999), more recently The Megamaser Cosmology Project (MCP) have carried out the most complete survey of megamasers to date, with the goal of measuring Hubble's constant (see e.g. the survey compilation by Braatz et al. 2015). The MCP observations also allow them to make several SMBH mass measurements (e.g. Reid et al. 2009; Zhao et al. 2018). The observed megamasers with SMBH masses have $V_{\rm obs}$ ranging from $170\,{\rm km\,s^{-1}}$ (NGC 1029; Gao et al., 2017) to $950\,{\rm km\,s^{-1}}$ (NGC 2273; Kuo et al., 2011), with an average of $\approx 600\,{\rm km\,s^{-1}}$. All megamaser systems are observed close to edge-on, so that $\sin(i) \approx 1$. Given this, megamasers typically probe gas at radii between 5×10^4 and 1.5×10^6 Schwarzschild radii. Our data thus show that the molecular gas disc in NGC 0383 extends unbroken and unwarped down to very close to the SMBH, and that it traces the same material probed by megamasers in other galaxies.

3.5 CONCLUSIONS

I have presented a measurement of the mass of the SMBH in the nearby lenticular galaxy NGC 0383 (radio source 3C 031). This estimate is based on ALMA observations of the ^{12}CO(2–1) emission line with a physical resolution of ≈ 43 pc ($0\farcs18 \times 0\farcs1$). I thus have a spatial resolution a factor of > 7 better than the $R_{\rm SOI}$. Our spectroscopic resolution, and a channel width of $10\,{\rm km\,s^{-1}}$, allow us to resolve gas down to $\approx 140,000$ Schwarzschild radii and thus to probe the same material as typical megamaser observations. NGC 0383 has a relaxed, smooth nuclear disc with weak ring/spiral features. I detect a clear Keplerian increase of the rotation velocity of ^{12}CO(2–1) at radii $\lesssim 0\farcs5$, and forward modelling of the ALMA data cube presented here with the KinMS tool in a Bayesian MCMC framework to measure an SMBH mass of $(4.2 \pm 0.7) \times 10^9\,{\rm M_\odot}$, a F160W-band mass-to-light ratio varying linearly from $2.8 \pm 0.6\,{\rm M_\odot/L_{\odot,F160W}}$ in the centre to $2.4 \pm 0.3\,{\rm M_\odot/L_{\odot,F160W}}$ at the outer edge of the molecular gas disc ($3\farcs5$ radius) and a velocity dispersion of $8.3 \pm 2\,{\rm km\,s^{-1}}$ (all 3σ uncertainties). I also detect continuum emission from the AGN in NGC 0383 across the full bandwidth, consistent with synchrotron radiation. This chapter not only shows the power of ALMA to estimate SMBH masses, but it also demonstrates that the molecular gas method is highly complimentary to megamaser observations as it can probe the same emitting material.

CHAPTER 4
TESTING THE WISDOM METHODOLOGY WITH A FIRE SIMULATED GALAXY

Math. It's just there... You're either right or you're wrong. That's what I like about it.

Katherine Johnson

4.1 INTRODUCTION

It is now widely accepted that supermassive black holes (SMBHs) co-evolve with their host galaxy and that there are empirical relationaships between the SMBH mass and various galaxy properties (see e.g. reviews by Kormendy & Ho 2013; van den Bosch 2016). Yet, these relations have large scatter and appear to change depending on the sample selected (see e.g. Fig. 2 of van den Bosch 2016). The most reliable SMBH masses are those measured dynamically, however the methods used are typically biased towards large, bright galaxies which compromises the SMBH-host galaxy relations drawn from them. Therefore to fully analyse the extent of the host galaxy-SMBH co-evolution it essential to gather a larger, more diverse sample of SMBH mass measurements (e.g. van den Bosch 2016; Davis et al. 2017).

The mm-Wave Interferometric Survey of Dark Object Masses (WISDOM) project that I have worked with, and other groups aim to fill this data gap by using the molecular gas method of SMBH mass measurement. As discussed earlier in this thesis, this involves modelling the kinematics of the molecular gas within the central kiloparsec of a galaxy with the SMBH mass at its centre a free parameter. Suitable molecular gas discs are found in many galaxies and are not limited to particular morphological types. The molecular gas method has proved successful with at least 12 measurements published so far. This method is especially promising, as for any redshift SMBH masses $\gtrsim 4 \times 10^8$ M$_\odot$ can be robustly measured, given sufficient surface brightness sensitivity (Davis, 2014).

The measurements typically use observations of the Carbon Monoxide (^{12}CO) emission lines to trace the velocity of the molecular gas, but some have used dense molecular gas tracers HCN and HCO$^+$ (Onishi et al., 2015). Emission in the millimeter wave bands is observable without dust attenuation and the high-resolution observations required are easily obtained with modern interferometers e.g. the Atacama Large Millimeter/submillimeter Array (ALMA). Targets for the molecular gas method tend to be chosen for their relaxed dust discs with no signs of disturbance, favouring those with existing molecular gas observations. These criteria have given a variety of new SMBH measurements (e.g Barth et al. 2016a; Smith et al. 2019) which are extending our knowledge of SMBH mass relations (e.g. Fig. 11 Davis et al. 2020 and Fig. 6.1 of this thesis). However the effect of observational parameters, e.g. beam size or channel width, and then how best to model the data has only been explored using simple analytic models (e.g. Chapter 2). In particular the ability to measure a SMBH mass depends on spectrally resolving the SMBH signature which is subject to the physical parameters of the galaxy (e.g. inclination) and the parameters of the observations (e.g. channel width, beam size etc.).

In this chapter we undertake to determine the effects of physical and instrument parameters on the SMBH mass derived. We do this by making use of mock observations, using a hydrodynamic simulation of a low-mass spiral galaxy. The simulation has a known SMBH mass, radial velocity and surface brightness profile which we can compare best-fitting values with. Our aim is explore the range of biases present in existing measurements using this method, and guide future observational campaigns. This work will focus on the modelling techniques used by the WISDOM project and test the pipeline in development. We will detail the observational parameters varied in Section 4.2. In Section 4.2.1 we will briefly introduce the simulation used and the specifics of the galaxy chosen from it, and present the simulated observations. Then we will detail the modelling performed on the simulated data cubes in Section 4.2.3. In Section 4.3 we will present and discuss the results of each observational parameter variation and conclude in Section 4.4.

4.2 SIMULATION AND METHODS

Within the WISDOM project we have developed a 3D forward modeling process to allow us to estimate SMBH masses from observational data. A model data cube is created, which can be compared directly with the observed data cube. The model parameters are then incrementally varied towards best-fitting values by a Markov Chain Monte Carlo (MCMC) method. The model data cubes are created by the publicly available KINEMATIC MOLECULAR SIMULATION (KINMS)‖ mm-wave observation simulation tool of Davis et al. (2013a).

KINMS requires as inputs the cube's observational parameters (e.g. channel width and beam size), a vector of the velocity profile of the gas as a function of radius (also a vector of this radius), the thickness of the disc, the inclination of the disc, the position angle of the velocity profile, the velocity dispersion of the gas, the total integrated flux of the cube and the surface brightness profile of the gas as either a function of radius or a 3-vector of positions. KINMS uses this information and applies observational effects (e.g. beam smearing) to create the model data cube.

When creating a model cube the observational parameters are matched to those of the observed data cube. In most WISDOM analysis the inclination, position angle, velocity dispersion and total integrated flux are variables fitted by the MCMC, initially approximated by eye. The disc thickness can be set to zero, i.e. assume a thin disc or if this is not appropriate it will also be fitted by the MCMC. The velocity profile of a galaxy is the quadratic sum of rotation caused by the gravitational field of the luminous matter ($V_{\rm gal}$) and that of the SMBH as:

$$V_{\rm rot} = \sqrt{V_{\rm gal}^2 + \frac{GM_{\rm BH}}{r}}. \tag{4.1}$$

Where G is the gravitational constant, $M_{\rm BH}$ is the SMBH mass and r is the radius vector. The surface brightness profile can be input into KINMS one of two ways, depending on the complexity of the gas distribution. If symmetric and relatively smooth, a simple parametrisation is sufficient (e.g. an exponential disc or Gaussian). Here a single vector of surface brightness values is input with a complimentary vector of radial positions. However for more complicated distributions, in particular non-symmetric or truncated discs or those with lots of substructure the simplification of a smooth gas distribution is inappropriate. In these cases it is better to input a 3-dimensional vector of positions at which clouds will be simulated. These can be drawn, for instance, from the clean components made during interferometric imaging (see Smith et al. 2019 for full details).

As mentioned in Section 4.1 we are investigating the influence of both the observational parameters and the modelling on the accuracy of the SMBH mass found. Using KINMS and its observation simulating capabilities mock observational data cubes can be created from a simulated galaxy. With the aim of advising future observing campaigns the parameters we vary are those that affect the ability to detect changes in the line-of-sight velocity close to the SMBH. Observationally the beam size, channel width and signal-to-noise ratio (SNR) are parameters that directly affect whether the SMBH signature will be detected and can be chosen appropriately especially if their influence is known. A galaxy's inclination will also affect the line-of-sight velocities observed and therefore whether the SMBH signature is detectable. We will therefore create mock data cubes each with a different one of these observational parameters varied to ascertain their affect on the SMBH mass recovery. Once the data has been obtained the model needs to be carefully chosen, in particular we will investigate how assumptions about the functional form of the surface brightness profile affect the accuracy of the recovered the SMBH mass. By modelling with two different styles of surface brightness profile we will investigate whether a smoother surface brightness profile or using the thin disc approximation severely impacts the accuracy of the SMBH mass recovered.

4.2.1 SIMULATION

The simulated galaxy used is a single snapshot from the work of Torrey et al. (2017), who produced three isolated galaxies of varying initial mass. The simulations are performed with the N-body hydrodynamics code GIZMO (Hopkins, 2015), which used a meshless-finite-mass method to solve the hydrodynamic equations of motion (Torrey et al., 2017). Further to gravity and hydrodynamics the code uses the Feedback In Realistic Environments (FIRE) sub-grid models to follow galaxy evolution processes which are unresolved by the simulation (Hopkins et al., 2014). See Torrey et al. (2017), Hopkins et al. (2014) and references therein for a full description of the simulation and FIRE feedback model, here we give a brief description.

The FIRE model includes radiative gas cooling, in assumed thermal equilibrium down to 10 K, and star formation associated feedback. No black hole feedback is included but a SMBH is included in the galaxy as a collisionless particle. Star formation is allowed for locally self-gravitating clouds, with the star formation rate given by $\dot{\rho}_* = \rho_{\rm mol}/t_{\rm ff}$ where $\rho_{\rm mol}$ is the volume density of molecular gas (fraction of dense, cold gas following Krumholz & Gnedin 2011) and $t_{\rm ff}$ is the free-fall time. Young stars contribute to feedback via thermal heating by photoionization, supernova, stellar winds and radiation pressure, with STARBURST99 (Leitherer et al., 2010) used to set the volume affected by each stellar particle. The initial conditions for the galaxy used in this chapter are summarised in Table 4.1, including the adaptive gravitational softening length and the mass resolution. The galaxy has a total mass of $M_{\rm tot} = 1.39 \times 10^{11}\,{\rm M}_\odot$ and a stellar mass of $M_* = 5.84 \times 10^9\,{\rm M}_\odot$. The gaseous disc is initialized with an exponential surface density profile with scale-length $R_{\rm d} = 1.7$ kpc. The snapshot used in this work was chosen to be after the relaxation time of

Table 4.1. The initial condition properties used for the simulated galaxy, $M_{\rm tot}$ is the total mass of each system and m_p is the baryon particle mass. ε is the minimum (Plummer equivalent) force-softening length implemented for each particle type.

Property	Gas Disc	Halo	Stellar Disk
$M_{\rm tot}$ ($\times 10^9$ M$_\odot$)	1.11	132	4.45
$m_{\rm p}$ ($\times 10^3$ M$_\odot$)	1.0	80	3.0
ε (pc)	1	10	2

the disc.

4.2.2 CREATING SIMULATED DATA

To create simulated data cubes we require the spatial, kinematic and flux information about the gas disc particles which would contain CO molecules, in one snapshot of the simulation.

To do so we select gas particles from the simulated galaxy which have a gas density of > 20 particles cm^{-3}. While this threshold would not correspond to a fully molecular medium in the real universe, this material is still considered dense given the sub-grid model used by the simulation. Adjusting this threshold would not affect our results. We also only select particles in the inner 0.7° (~ 200 kpc), i.e. are part of galaxy.

The particle positions are rotated by the chosen inclination and these positions, fluxes and velocities are input into KINMS using the INCLOUDS, FLUX_CLOUDS and VLOS_CLOUDS keywords. We set the total flux to 200 Jy km s^{-1} and the beam and pixel size, and channel width are all set as part of the observational parameter variation. The cube always has 600 channels, a minimum 1200 km s^{-1} bandwidth, and 64×64 spatial pixels, a minimum cube size of $4\farcs8 \times 4\farcs8$. The pixel size is always set as a third of the beam size, this ensures the beam is Nyquist sampled. KINMS creates a noiseless cube with this information. We then add noise, the noise level is one of our observational parameters and the noise is convolved with the beam before it is added to the cube to better reflect the correlated nature of noise in an interferometer.

The parameters varied and their ranges are listed in Table 4.2. All the ranges are physically motivated, or set by ALMAs' observing capabilities. The canonical value is that taken when the parameter is not being varied and are chosen as representative of the high resolution observations obtained by ALMA. An inclination of 0° is exactly face-on and therefore has no rotational velocity components in the direction of observation, therefore the minimum inclination we use is 5°. A galaxy exactly edge on has an inclination of 90° this is the angle with the largest line-of-sight velocity components however as inclinations

Table 4.2. Table of observational parameters varied when making mock data cubes of the simulation, listing the canonical value for each i.e. the value taken when not being varied. Also the range of values tested.

Parameter	Canonical Value	Range
Inclination (°)	60	5-88
Beam size ($''$)	0.15	0.015-1.5
Channel width ($\mathrm{km\,s^{-1}}$)	10	2-90
Signal-to-Noise ratio	7.5	75-0.4
Disc-thickness ($''$)	off	0-5/off

cannot be higher than 90° we opted for 88° as the largest simulated inclination. The theoretical mean inclination of galaxies on the sky is 60°, hence that is the canonical value. The beam size range was selected as the possible range of observations that current interferometers, in particular ALMA, could observe, with the smallest beam set by the resolution of the simulation (≈ 1 pc). The channel width lower bound is set by the minimum channel width typically used for extragalactic observations with ALMA ($2\,\mathrm{km\,s^{-1}}$). The SNR is defined as

$$SNR = \frac{\sum_{n=0}^{n_{\rm chans}} (F_{\rm peak,n}/rms)}{n_{\rm chans}}, \tag{4.2}$$

where $F_{\rm peak,n}$ is the peak flux of each channel, rms is the noise level added to the cube and $n_{\rm chans}$ is the number of channels which contain signal. The SNR is varied from ≈ 75 to ≈ 0.4 to probe how faint a CO detection can still be used to obtain a SMBH mass. In this work the simulated galaxy is projected to a distance of 16.5 Mpc i.e. the Virgo Cluster (Mei et al., 2007) where $1''$ corresponds to a physical distance of ≈ 80 pc. The position angle is always set to 90°.

Moment maps of the canonical data cube are shown in Fig. 4.1, Table 4.2 lists the canonical properties. The moment maps are made using the smooth masking technique (e.g. Dame, 2011), where a mask was produced by taking a copy of the data cube and smoothing it, first spatially with a Gaussian equal to the FWHM of the beam and then in velocity with a Gaussian of FWHM equal to 4 channels. The mask is then the pixels in the smoothed cube which have a value above some threshold. We note the mask is only applied when making the moment maps and not in any further analysis of the cubes.

4.2.3 METHOD OF MCMC ANALYSIS

We follow the same analysis used by the WISDOM project papers on the simulated data cubes. Model data cubes are created using KINMS and directly compared to the simulated data cube using a MCMC method as implemented in KINMS_MCMC** (Davis 2014;

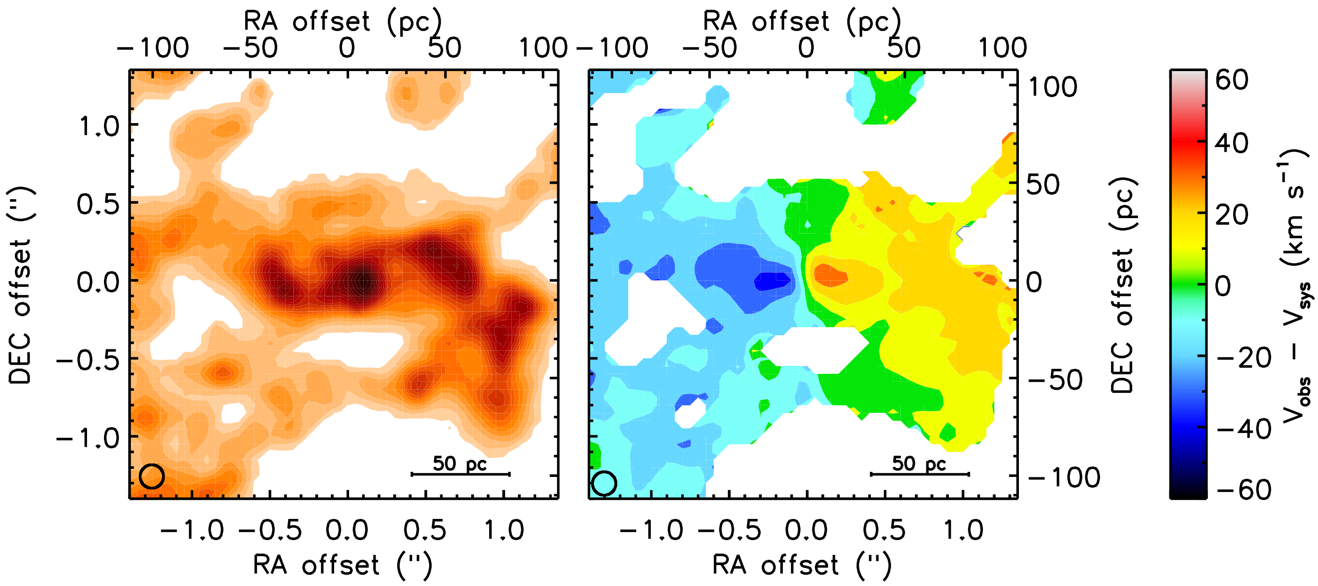

Figure 4.1. *Left hand panel:* Moment zero, integrated intensity and *right hand panel:* moment one, the intensity weighted mean velocity of the centre of the canonical simulated galaxy, where $V_{\rm sys} = 0\,{\rm km\,s^{-1}}$. The ellipse in the bottom-left of each panel is the beam, $0\farcs15 \times 0\farcs15$.

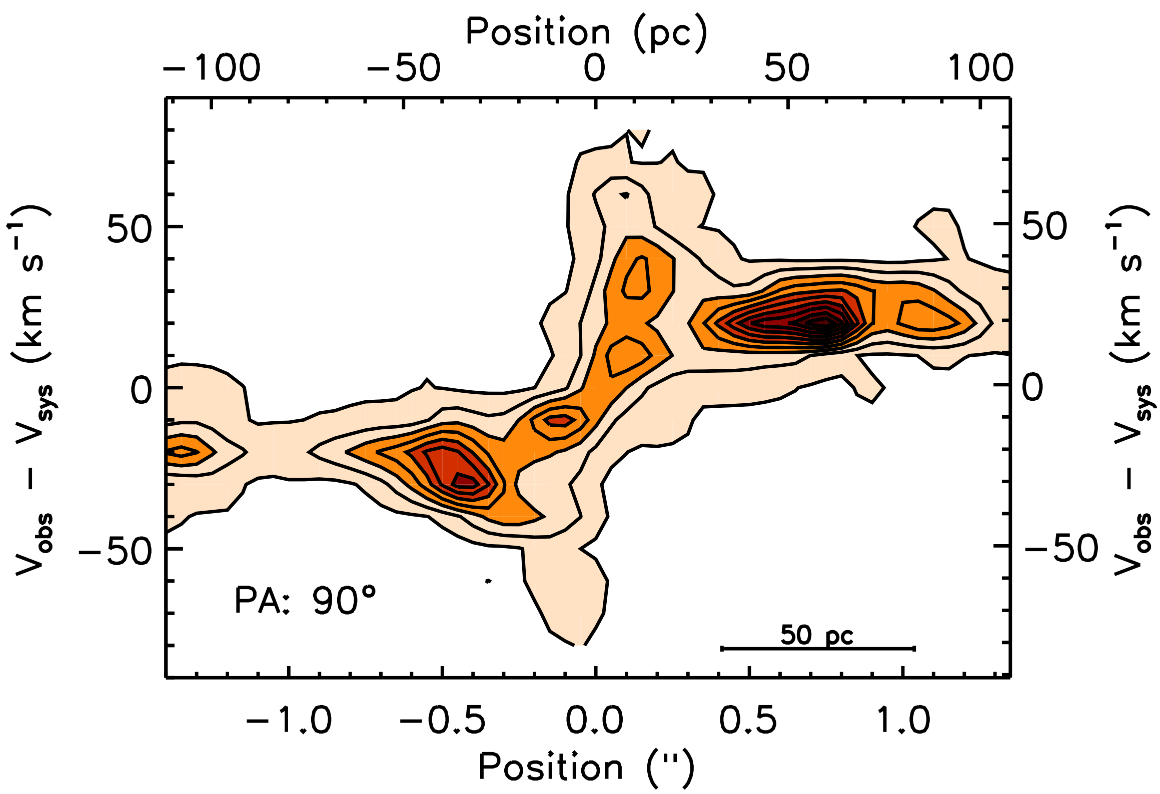

Figure 4.2. Position Velocity Diagram, using a 3 pixel wide strip along the major-axis of the canonical simulated galaxy, position angle of 90°and $V_{\rm sys} = 0\,{\rm km\,s^{-1}}$. The Keplerian motion of gas around the BH is clearly detected in this object when using the canonical observation parameters (see Table 4.2).

Table 4.3. MCMC variables

Parameter	Search range
log (SMBH mass/ $M_\odot$)	5 – 9
Position angle (°)	80 – 100
Inclination (°)	i-10 – i+10 within 0 – 90
Velocity dispersion (km s^{-1})	0 – 12
Nuisance parameters	
Integrated intensity (Jy km s^{-1})	10 – 500
Centre X offset ($''$)	-0.5 – 0.5
Centre Y offset ($''$)	-0.5 – 0.5
Centre velocity offset (km s^{-1})	-10 – 10

Davis et al. 2017). KINMS_MCMC easily interfaces with KINMS to create the model cubes and then compare them with the data cube using likelihood maximisation, incrementally driving the model parameters towards best-fitting values. Whereas with real observations a model of the luminous mass would be made from optical/near-infrared images and then a rotational velocity curve made from that here, we can use the known rotational velocity curve from the original simulation. This contains rotation under the influence of both the gas and stars in the galaxy, as can be seen in Fig. 2 of Torrey et al. (2017) the dark matter halo is negligible at the radii we probe.

The $M_{\rm BH}$ is a variable in the MCMC, with a flat prior in log-space. All other priors are flat in linear-space, see Table 4.3 for the variables and their search ranges.

Each MCMC is run as a single chain, with 100,000 iterations in the final, converged run. Due to the noisy, large nature of the datasets used they have additional uncertainty associated with them (Andrae, 2010). The χ^2 distribution has a variance $2(N-P)$ where N is the number of constraints and P is the number of inferred model parameters. Where N is large (e.g. here $N \approx 10^5$) this variance approximates to $\approx 2N$. van den Bosch & van de Ven (2009) note that the traditional approach using $\Delta\chi^2 = 1$ yields unrealistic uncertainties which are too small due to systematic effects. They introduce a rescaling of the confidence interval to $\Delta\chi^2 = \sqrt{2N}$. Smith et al. (2019) and Chapter 3 in this thesis (North et al., 2019) also used this rescaling and found it yields more physically reasonable uncertainties, and we use this procedure again here in this chapter.

4.3 RESULTS AND DISCUSSION

As discussed above, we fit the mock observations of each galaxy in three different ways:

1. Using the exact positions of each of the gas particles (removing the impact of the fitted surface brightness profile from our fitting, leaving only uncertainties caused by the velocity structure).

2. Using an exponential disc as the input gas surface brightness profile, as has been done in various existing SMBH mass measurements of this type.

3. Using a model of the gas disc created using the SKYSAMPLER tool of Smith et al. (2019). This is a middle ground between 1 and 2 above, and allows us (in a way that can be reproduced in purely observed systems) to take into account the non axisymmetric structures present within the gas disc.

In the following we will compare how each observational parameter affected the accuracy and uncertainties of the best-fitting SMBH mass. The best-fitting values of the other fitted variables will be discussed where appropriate.

4.3.1 INCLINATION

The inclination of a galaxy on the sky affects how large the component of its rotational velocity is into our line-of-sight with low inclination (face-on) objects having a smaller component than high inclination (edge-on). From simple arguments (see Chapter 2 and e.g. Davis 2014) we expect that in more edge-on systems (where more of their circular velocity is projected into our line-of-sight) the presence of any SMBH signature will be maximised. Thus we should obtain more accurate SMBH mass and smaller uncertainties, and can potentially detect smaller SMBH masses (see Chapter 2 especially Fig. 2.2). In Fig. 4.3 we show the SMBH mass retrieved from our fitting procedure for realisations of the simulation with different inclination angles. We find that the low inclinations ($\lesssim 20^\circ$) have large uncertainties and the best-fit value can vary by up to an order of magnitude. In particular using the exponential disc surface brightness profile, rather than particle positions, increases the uncertainties.

For inclinations between 25° and 85° the best-fit found is consistent with the true values within 3-sigma uncertainties. A slight underestimate of the true SMBH mass is present at intermediate inclinations, due to an overestimate in the inclination found by the exponential disc and SKYSAMPLER models. In particular the exponential disc overestimates the inclination and is inconsistent with the true value at inclinations of $40-55^\circ$, probably because aligning the smoother profile with the mock data is more difficult than when using one with the correct substructure. The integrated flux and position angle also have large uncertainties but no systematic offset.

In the 25° and 85° range the MCMC chains converge quickly and the parameters are well constrained. This indicates that at these inclinations we can robustly measure the SMBH mass, however it should be noted that for inclinations below 55° the uncertainty in the inclination is the dominant fitting uncertainty. The strong covariance between that and SMBH mass means that this can be problematic, for instance Smith et al. (2019) decided to fit the inclination independently then fix it when fitting with the MCMC.

For inclinations above 20° using the original particles as the surface brightness profile appears to find the correct inclination for the galaxy. This is expected as having the identical gas distribution allows the MCMC to align the data and model exactly.

Fig. 4.3 follows the expectations from the figure of merit arguments in Chapter 2 and Fig. 2.2, however what the figure of merit doesn't account for in SMBH recovery is creating the surface brightness profile. At very high inclination ($> 80°$) SKYSAMPLER models have increased uncertainties, probably due to the lack of information on the gas distribution due to the edge-on view of the galaxy.

When fitting with an exponential disc surface brightness profile having to fit the disc scale length adds in an extra free parameter which increases the uncertainties in the fitting. Also the disc scale length is covariant with inclination and therefore SMBH mass, meaning the accuracy of the disc scale length fit will directly impact the accuracy of the SMBH mass. At low inclination larger errors reflect the uncertainty in this parameter. At very high inclination ($> 80°$) the disc scale length jumps to $\approx 3.5''$ (from $\approx 0.9''$) as the galaxy becomes too edge on to properly constrain this variable.

In conclusion, for inclinations $\gtrsim 30°$ SMBH masses can be reliably estimated, especially if the surface brightness profile of the emission can be well reproduced by the modelling method.

4.3.2 BEAM SIZE

The beam size of the observations affects how well the SMBH signature is spatially resolved, as mentioned before Davis (2014) showed that resolving $2 \times R_{\rm SOI}$ is required, we are not re-testing this. The $R_{\rm SOI}$ can be estimated by finding the the local minimum in the rotation curve i.e. the PVD (Fig. 4.2). By visual inspection, we estimate this occurs at a radius of $\approx 0''.5$ ($\approx 40\,$pc). The top panel of Fig. 4.4 shows the variation of best-fitting SMBH mass with beam size. Up to a beam size of $\approx 0''.5$ the best-fitting SMBH mass value found and uncertainties are reasonable. Above $\approx 0''.5$ the uncertainties increase and the best-fitting value begins to be over estimate the SMBH mass which is expected as beam size is larger than $R_{\rm SOI}$. SKYSAMPLER appears to find better best-fitting models than the exponential disc, with smaller uncertainties for beam sizes below $1''$. The model needs to

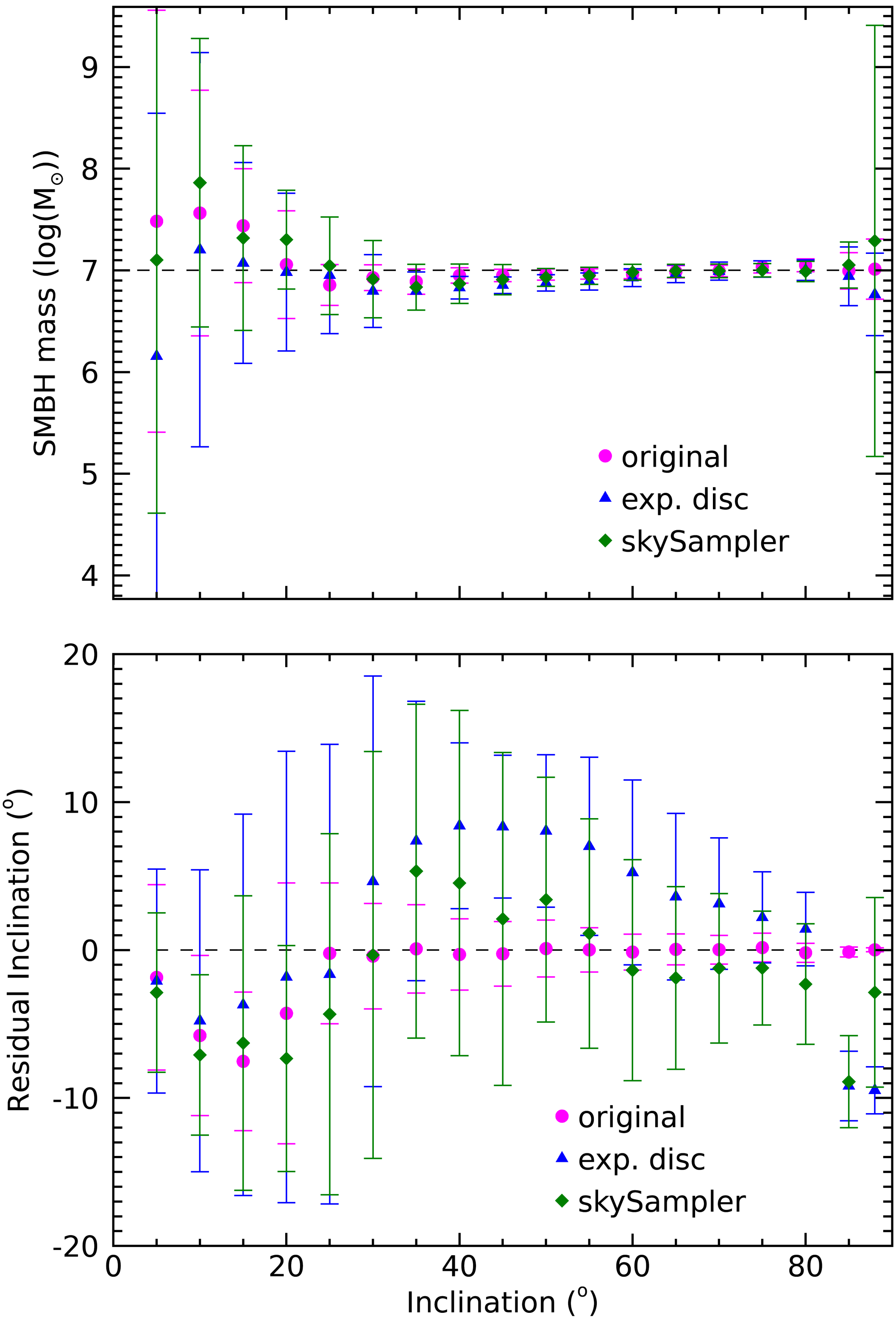

Figure 4.3. *Top panel:* Best fitting SMBH mass, compared with the known value (black dashed line) as a function of the simulated inclination. *Bottom panel:* Residual of best-fitting inclination minus simulated inclination as a function of the simulated inclination. All error bars show the 3σ uncertainties.

be appropriate for the amount of information on the surface brightness profile available.

The bottom panel of Fig. 4.4 shows the disc scale length for the exponential disc models. This has a sharp increase at $\approx 0\farcs5$ indicating this is the largest beam size that should be used on this galaxy. Beyond this scale the emission of the galaxy is smeared by the large beam and the uncertainty in the surface brightness profile dominates, and again this beam size is larger than $R_{\rm SOI}$.

4.3.3 CHANNEL WIDTH

The channel width dictates how well we can spectrally resolve, and therefore disentangle, the different components of rotation within the disc. Whilst the smallest channel width tested was set as the highest spectral resolution typically obtained in extragalactic observations with ALMA, the velocity dispersion of the gas also limits how well you can resolve the underlying rotation. In particular, spectral resolution is important in the inner disc so the Keplerian rotation due to the SMBH can be distinguished from the rotation due to the stellar potential. Narrower channels are therefore able to detect lower SMBH masses as shown in Chapter 2 and Fig. 2.2 which implies that for a SMBH of $M = 10^7\,{\rm M_\odot}$ a maximum channel width of $\approx 15\,{\rm km\,s^{-1}}$ is required. However, as also discussed in Chapter 2 decreasing the channel width increases the noise per channel, which can lead to some flux dropping below the noise limit and therefore not being detected.

Fig. 4.5 shows the variation in SMBH mass recovered from our fitting procedure with realisations of different channel widths. It shows that channel widths $\leq 30\,{\rm km\,s^{-1}}$ provided accurate best-fits to within 3σ uncertainties. For large channel widths ($> 40\,{\rm km\,s^{-1}}$) the uncertainties at least quadruple in size, to almost an order of magnitude. The galactic emission covers $\sim 130\,{\rm km\,s^{-1}}$, or 3 channels at $40\,{\rm km\,s^{-1}}$, which indicates why the uncertainties increase sharply at channel widths greater than this. With only 3 channels the MCMC has little or no velocity information about the area directly affected by the SMBH and therefore can obtain a good fit with a large range of SMBH masses. Interestingly channel widths of above $15\,{\rm km\,s^{-1}}$ (the apparent limit from the figure of merit; Chapter 2) are still able to recover the SMBH mass with reasonable uncertainties. This implies some leeway in the channel width used.

The effect of channel width on the accuracy of the SMBH mass is small, provided the channel width is narrow enough to spectrally resolve the different velocities of the central region of the disc from the outer region in both blue and redshift. Using an exponential disc surface brightness profile does increase the uncertainties on the SMBH mass, compared to using a 3-dimensional vector of positions.

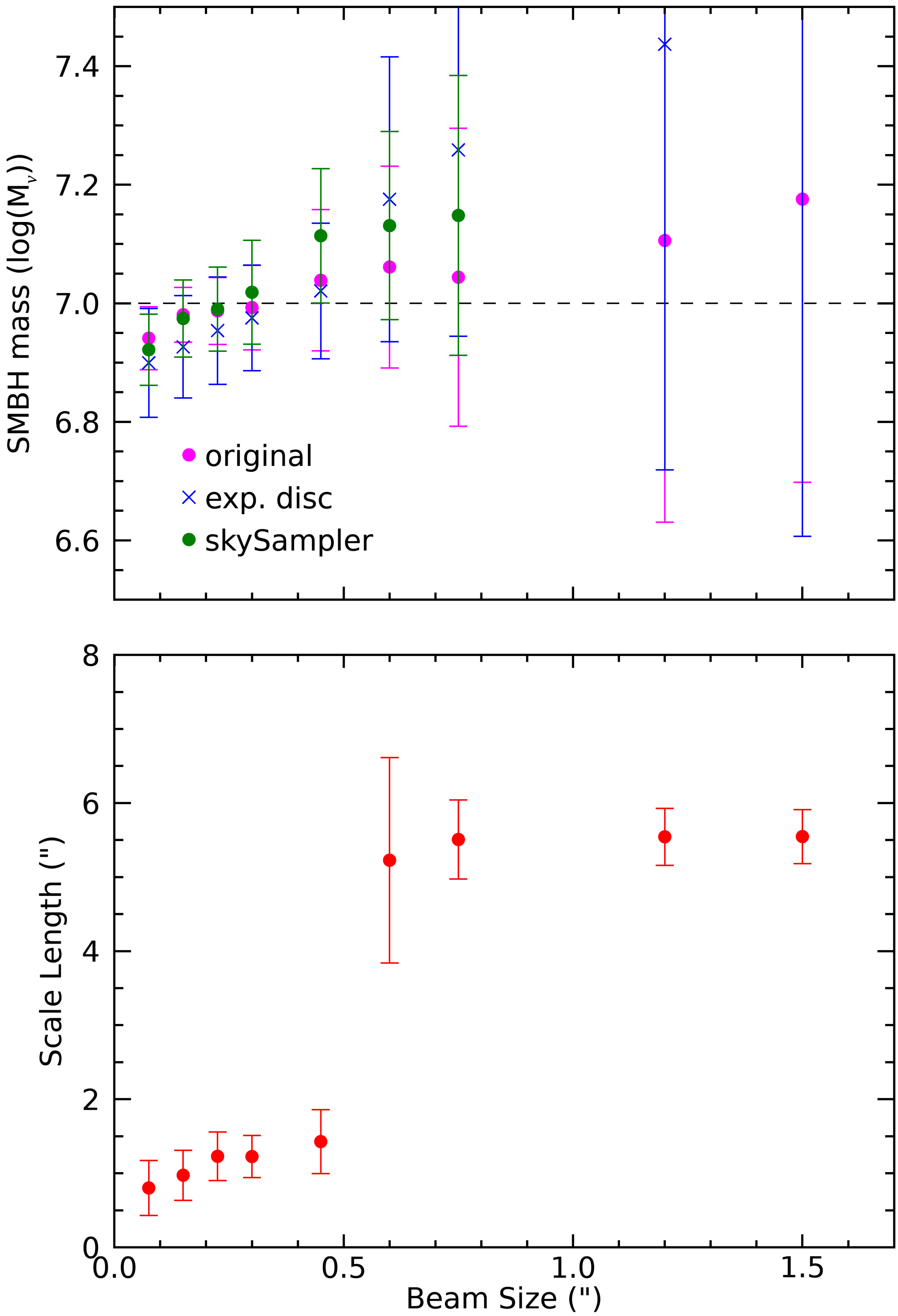

Figure 4.4. *Top panel:* Best fit SMBH mass, compared with the known value (black dashed line) as a function of the simulated beam size. *Bottom panel:* Exponential disc scale length as a function of the simulated beam size. All error bars show the 3σ uncertainties.

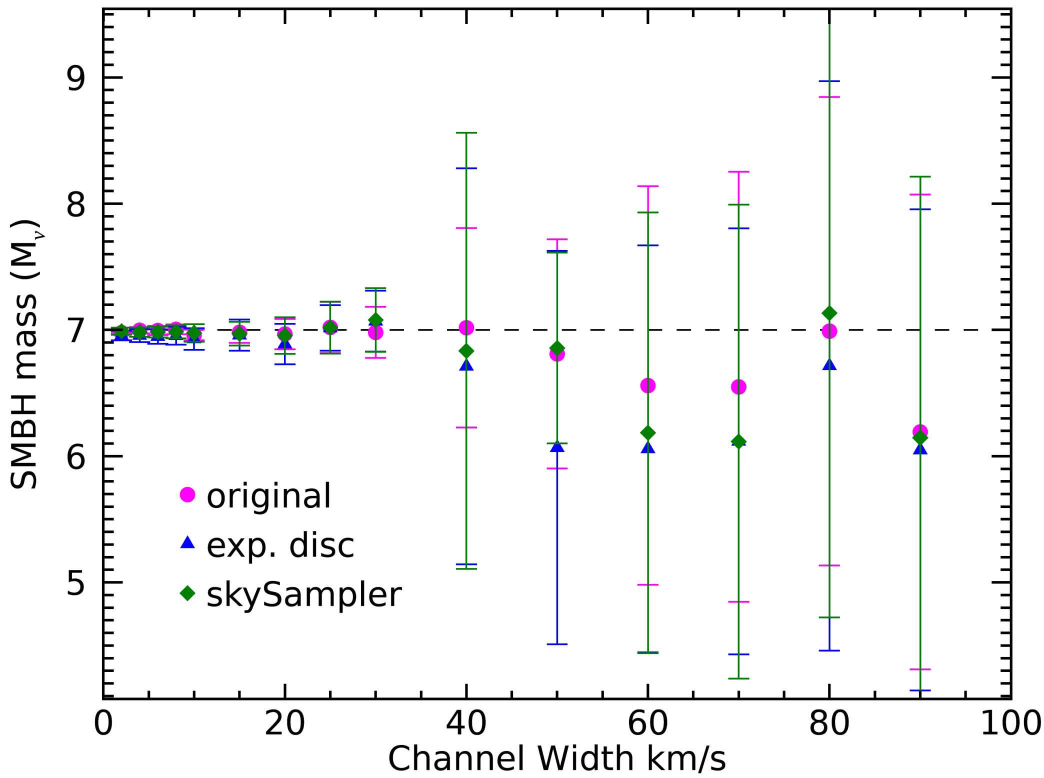

Figure 4.5. Best fit SMBH mass, compared with the known value (black dashed line) for the channel width variation.

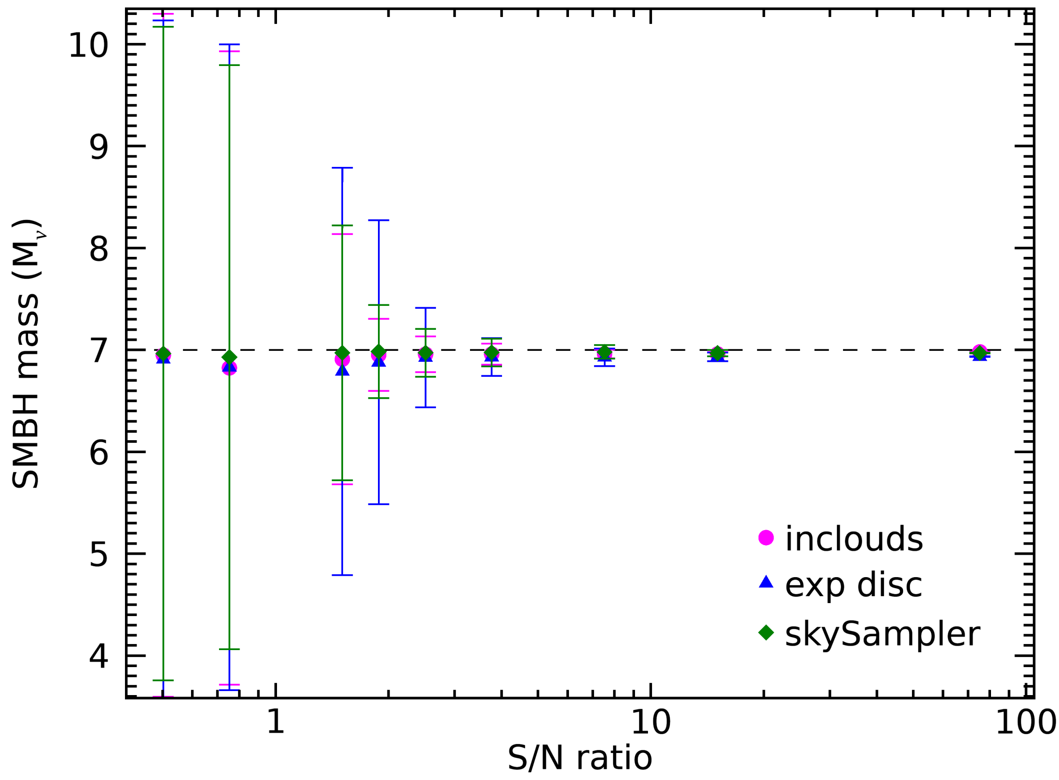

Figure 4.6. Best fit SMBH mass, compared with the known value (black dashed line) for the signal-to-noise ratio width variation.

4.3.4 SIGNAL TO NOISE RATIO

The noise added to the simulated data cubes before fitting was also varied to ascertain what limiting SNR is required to obtain an accurate SMBH mass. It was found that down to a SNR of 3 the uncertainties are reasonable, at $\lessapprox 0.5$ dex. Again the exponential disc appears to be the least accurate with larger uncertainties than the other models.

As expected from the common use of SNR$\gtrapprox 3$ for a robust measurement, this work also found that all models below this limit have large (> 1 dex) uncertainties and would not be considered accurate measurements. This confirms the use of SNR≥ 5, as typically enforced, is suitable for accurate SMBH mass measurements. The selection of targets, currently, uses single dish or Atacama Compact Array (ACA) observations to predict the flux that will be received, this is important for setting the noise requirements of higher resolution observations. The highest resolution used must also be considered carefully as resolving out a lot of flux is also problematic for making a measurement, for instance by underestimating the molecular gas mass and therefore its gravitational influence.

4.3.5 SURFACE BRIGHTNESS MODELLING

In the real universe molecular discs are not geometrically thin, but are extended in the vertical direction. For instance the vertical scale height of the milky way molecular material is $\approx 100\,\mathrm{pc}$ (e.g. Roman-Duval et al., 2016). Ignoring this could, in principle, affect the SMBH mass we derive, as any line of sight would no longer probe material at a single radius. I tested this by removing the thin disc assumption within KINMS, and refitting the canonical data. The use of the thin disc assumption (KINMS input diskthick=0) on this galaxy does not change the best-fitting SMBH mass value significantly (causing variations $< 1\%$ in the estimated SMBH mass, well below the uncertainty level). Therefore unless the disc is obviously thick using the thin disc approximation will not change the best-fitting model significantly.

We do not find a significant difference between the surface brightness profiles used, but do see larger uncertainties in the exponential disc models which is expected as these models have more free variables to fit. As seen in Fig. 4.1 the surface brightness profile of the simulated galaxy is complex and therefore this is encouraging for future work as the tools we have developed recreate the surface brightness profile well enough to accurately measure the SMBH mass.

4.3.6 REPEATED FITTING

As mentioned above a fit to each variation of observational parameter, with each surface brightness profile was only performed once. It is also important to test how repeatable the fit is, what the spread of best-fitting values is, and repeating the fit also gives a good understanding of the uncertainties. The fit to the canonical data cube with the original particle positions was therefore repeated 10 times.

These repeats show that whilst individual MCMC runs do vary in the best-fitting values found the variability of these is very small. It was found that the SMBH mass has a mean over 10 repeats of $9.1 \times 10^6\,\mathrm{M}_\odot$ with a standard deviation of $5.4 \times 10^3\,\mathrm{M}_\odot$ indicating the MCMC finds a very similar, accurate fit each time it is run from the true value in the simulation.

In the future it would be informative to test repeat fits with randomised initial values, as opposed to the true values currently used, to investigate how the MCMC handles this and check whether it struggles to find the χ^2 minimum.

4.4 CONCLUSIONS

The measurement of SMBH masses with molecular gas kinematics from high-resolution ^{12}CO observations is now becoming popular. Here we test the method's reliability by taking a simulated galaxy of known parameters and creating mock data cubes with that gas distribution and velocity. We vary the galaxy's inclination on the sky, the beam size, channel width and SNR of the observations. We also test different ways of modelling the surface brightness profile, and using the thin disk approximation or fitting the disc thickness. The observational parameters varied can advise future observers in their target selection, the recommendations that can be made from this work are as follows:

- Galaxy inclinations of $\approx 40-80°$, we found these have a large enough component of the rotational velocity into the line of sight and good information on the gas distribution to create an accurate model.
- Channel widths of $\leq 20\,\mathrm{km\,s^{-1}}$ or at least 5 channels across the line width is required to spectrally resolve the SMBHs gravitational influence.
- As is the common standard for observations a SNR of ≥ 3 is also an appropriate detection limit for SMBH mass measurements.
- Inputting a 3-dimensional vector of positions for the surface brightness profile (e.g. from SKYSAMPLER[††] fitting of the clean components) as opposed to a simplified parametrisation reduces the uncertainties. This mostly stems from having fewer variables to fit in the MCMC.

This work shows again that the molecular gas method is both easy to implement and accurate in result, it is a powerful tool for the measurement of SMBH masses.

CHAPTER 5

MULTISCALE FEEDBACK IN THE BRIGHTEST CLUSTER GALAXY NGC 0708: EVIDENCE FOR A MOLECULAR OUTFLOW

If we assume we've arrived: we stop searching, we stop developing

Jocelyn Bell Burnell

This chapter presents evidence for AGN feedback on the molecular gas in NGC 0708. This work has been submitted to MNRAS for publication.

5.1 INTRODUCTION

The lack of molecular gas in early-type galaxies (ETGs; ellipticals and S0s) has been a point of debate for some decades (e.g. Faber & Jackson 1976; Lees et al. 1991; Young et al. 2011; Davis et al. 2019). Observations show that whilst ETGs have internal sources of gas, for instance stellar mass-loss, they have lower gas fractions than late-type galaxies (e.g. Lees et al., 1991). This is especially true of brightest cluster galaxies (BCGs), where mergers and intra-cluster medium (ICM) cooling should bring large amounts of molecular gas into the galaxy, but their observed molecular gas reservoirs are an order of magnitude smaller than expected (e.g. Lees et al. 1991; Fabian 1994; De Lucia & Blaizot 2007).

The ICM and the baryonic halo of massive galaxies is composed mostly of hot ($T \sim 10^7$ K) optically-thin gas, that cools by emitting bremsstrahlung radiation (predominantly in the X-ray band; Fabian 1994). The rate of bremsstrahlung cooling depends on the square of the gas density and therefore the centre of the galaxy (and the galaxy cluster in the case of a BCG) cools fastest. This cooler gas flows inwards at subsonic speeds, increasing the density and hence the cooling rate, thus creating a run-away process (Fabian, 1994). When the cooling time is shorter than the age of the universe, a cooling flow can form (Fabian et al., 1984). The gas then cools and inhomogeneities allow clouds of cooled gas to drop out of the flow. These are deposited in the cluster core and will continue to flow onto the BCG/central galaxy, increasing its gas content (Fabian et al., 1984). The clouds have internal radial temperature gradients, with temperatures of < 100 K in their cores, therefore forming molecules that can lead to star formation (Ferland et al., 1994). Edge et al. (1992) and Fabian (1994) reported that the criterion for a cooling flow is satisfied in 70–80 percent of clusters, suggesting that most should be growing their central galaxy. However, Fabian (1994) also noted that at the mass inflow rates of observed cooling flows, 10–1000 $M_\odot$ yr^{-1}, central galaxies should be much bluer and brighter than actually observed. Searches for this cooled gas have persistently returned lower gas masses and fewer young stars than required by cooling flow observations (e.g. Johnstone et al. 1987; Heckman et al. 1989; McNamara & O'Connell 1989; Crawford et al. 1999; Donahue et al. 2000; Hoffer et al. 2012). A solution to the 'cooling flow problem', how gas leaves the hot phase but does not condense on to the central galaxy, has hence been sought ever since.

High-angular resolution X-ray observations paved the way for answers, showing that despite appearing relaxed at low resolution, the centres of cooling flow clusters are in fact very dynamic. Active galactic nuclei (AGN) with powerful jets are found in essentially all cooling flow cluster central galaxies (Sun, 2009), and they are the principal power source driving the ICM dynamics (e.g. Bîrzan et al. 2004, 2012; McNamara et al. 2005; Rafferty et al. 2006; McNamara & Nulsen 2007, 2012; Gaspari et al. 2013; Hlavacek-Larrondo et al. 2015). AGN jets appear to be able to inflate large bubbles in the hot ICM, that rise buoyantly and disrupt the cooling flow. Heat from the AGN is also distributed in the ICM through turbulent mixing and cocoon shocks (e.g. Gaspari et al. 2013). AGN jets have the mechanical power to balance the ICM's energy losses due to cooling, motivating the theory that mechanical (i.e. radio-mode) feedback is the principal regulator of ICM cooling, thus preventing a run away process (see reviews from e.g. McNamara & Nulsen 2007, 2012). Simulations also point to AGN feedback being vital for the regulation of a galaxies gas reservoir and therefore its star formation rate. Models including radio-mode feedback find better agreement with e.g. the galaxy luminosity function (e.g. Bower et al. 2006, 2008; Croton et al. 2006; McCarthy et al. 2008; Davé et al. 2012).

The advent of high resolution radio/sub-mm interferometry has begun to add to the growing picture of feedback controlled galaxy evolution. In multiple cooling flow clusters significant ($\approx 10^9$-$10^{10}\,M_\odot$) amounts of molecular gas have been detected in filaments coincident with buoyant bubbles seen in X-rays rising through the ICM (e.g. McNamara et al. 2014; Russell et al. 2014, 2016, 2017b,a; Vantyghem et al. 2016, 2018). It is not currently well understood if this cold gas was lifted by the bubble directly, has recently cooled from low entropy gas lifted by the bubble, or is stimulated to cool by the passing of the bubble. However the coupling factors required for direct lifting of cold gas are uncomfortably high (e.g. McNamara et al., 2014). Many of these observed filaments also have star formation associated with them (e.g. Vantyghem et al. 2018).

A variety of works have used simulations to look at the formation of this multiphase ICM to ascertain how it is regulated. Gaspari et al. (2012), Sharma et al. (2012), Prasad et al. (2015) and Li et al. (2015) all see cycles within their simulations where dense, cold gas filaments condense out of the ICM and precipitate on the central galaxy. This causes star formation and fuels the central SMBH to become an AGN. The AGN and supernova winds increase heating within the ICM, returning it to a high entropy state, and stopping to cooling and hence the fuel supply. When the heating stops, cooling resumes again. They find that cold gas filaments form when the instantaneous ratio of the thermal instability and free-fall timescales is $\lesssim 10$ (e.g. Gaspari et al. 2012; Sharma et al. 2012, Li et al. 2015). McNamara et al. (2016) propose an alternative model, where the molecular gas condenses from low entropy gas lifted by the buoyant bubbles. The gas becomes thermally unstable because it has reached an altitude where its cooling time is shorter than the time required to fall to its equilibrium location in the galaxy.

In all cases described above, the AGN is crucial in driving the evolution of the gaseous material in brightest cluster galaxies on the scale of 10's to 100's of kilo-parsecs. However, AGN are also known to act at small (kpc and sub-kpc) scales, both in normal galaxies, and in some BCGs. For instance, high resolution radio observations have revealed several normal non-interacting galaxies with (sub-)kiloparsec scale molecular gas outflows (e.g. Alatalo et al. 2011; Aalto et al. 2012; Morganti et al. 2015; Fernández-Ontiveros et al. 2020). In these systems even low-luminosity AGN can drive mass outflow rates of $\approx$ 10-$100\,M_\odot\,yr^{-1}$. By analysis of the observed characteristics of the outflows the most likely scenario is the AGN radio jet directly impacting the ISM in many of these cases.

Tremblay et al. (2012a,b, 2016) found multiwavelength evidence of both large- and small-scale mechanical feedback in the BCG of Abell 2597. They reported an extensive kpc-scale X-ray cavity network, with multiple rising buoyant bubbles, the largest of which coincides in both linear extent and position angle with the radio jet (Tremblay et al., 2012a). *Hubble Space Telescope (HST)* and *Herschel* observations reveal ongoing star formation co-spatial with knots in the X-ray emission (Tremblay et al., 2012b). ALMA ^{12}CO(2–1) observations further added to this picture, uncovering cold, clumpy accretion onto the central SMBH (by revealing absorption features in the AGN continuum caused by clouds moving inwards towards the SMBH; Tremblay et al. 2016).

Here I report on molecular gas observations of NGC 0708, the BCG in the Abell 262 galaxy cluster, itself part of the Perseus-Pisces galaxy supercluster. NGC 0708 lies 58.3 ± 5.4 Mpc away (estimated using infrared surface brightness fluctuations; Jensen et al. 2003). It is a giant elliptical galaxy with a weak dust lane (Ebneter & Balick, 1985; Wegner et al., 1996) and an effective radius of $33''$ (≈ 9.3 kpc; Wegner et al. 2012). See Fig. 5.1 for a *HST* image of NGC 0708. Abell 262 was identified as having an X-ray emitting ICM by Jones & Forman (1984), and Stewart et al. (1984) measured the cooling time to be 1.3×10^9 yr, smaller than the age of the universe so that the cluster is expected to form a cooling flow. The 20-cm observations of Parma et al. (1986) revealed a double-lobed, 'S'-shaped jet and led to the classification of NGC 0708 as a weak Fanaroff–Riley Class I radio source (Blanton et al., 2004). The top panel of Fig. 5.1 also has 330 MHz continuum observations overlaid (green contours), to show the shape and orientation of the large-scale jet. Analysis of *Chandra* observations revealed a hole or bubble within the ICM, co-spatial with the eastern lobe of the jet (Blanton et al., 2004). Clarke et al. (2009) found additional cavities at differing position angles within the X-ray gas, indicating multiple episodes of AGN activity from a (likely precessing) SMBH jet. They concluded that the total AGN emission should be capable of counteracting the cooling flow over several outbursts. Using their multi-frequency observations of NGC 0708, Clarke et al. (2009) also calculated the spectral index (α) from 235 to 610 MHz, finding the spectrum to be shallow in the core ($\alpha = -0.5$), typical of new particles in a jet. Clarke et al. (2009) also estimated a lower limit on the average outburst repetition timescale in Abell 262 to be $\tau_{\rm rep} \geq 28$ Myr.

NGC 0708 was thus observed to have large-scale feedback affecting the hot gas. In this work, I show that the cold interstellar medium (ISM) is also being affected on small scales. In Section 5.2, I present new Atacama Large Millimeter/submillimeter Array (ALMA) and enhanced Multi-Element Radio Linked Interferometer Network (e-MERLIN) observations. I discuss the origin of the signatures I see and present my analysis in Section 5.3. In Section 5.4 I discuss the results and compare NGC 0708 to other galaxies with molecular outflows. I conclude in Section 5.5.

I use the 'coupling factor' to compare the kinetic power required to drive the outflow to the various possible sources of energy in this system. This allows us to ascertain which feedback mechanisms are capable of driving the outflow I observe.

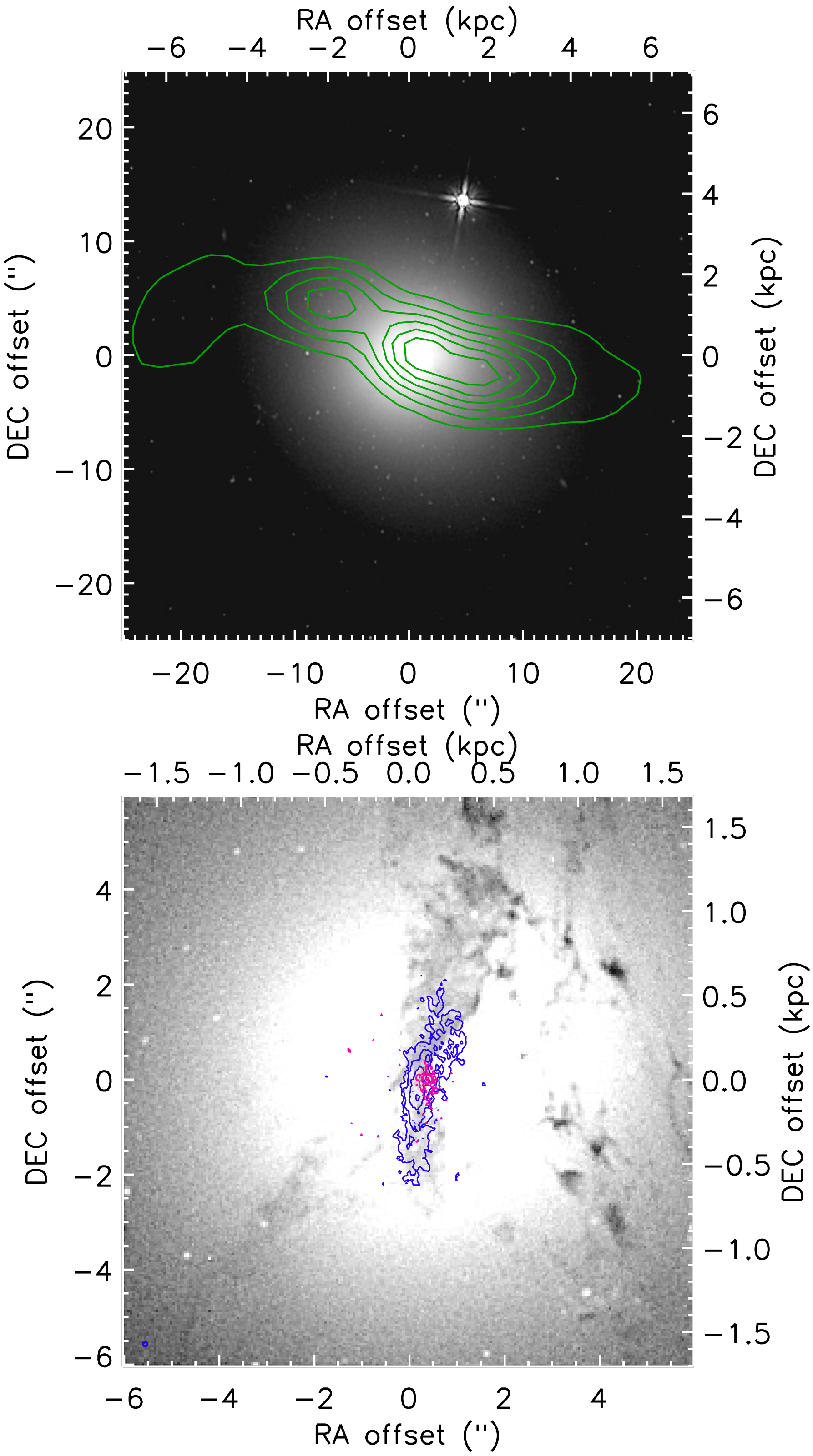

Figure 5.1. *Top panel:* Large scale ($50'' \times 50''$ or $14 \times 14\,\mathrm{kpc}^2$) *HST* Wide Field Camera 3 F110W image of NGC 0708, with 330 MHz continuum Very Large Array (VLA) contours overlaid in green. *Bottom panel:* Small scale ($12'' \times 12''$ or $3.2 \times 3.2\,\mathrm{kpc}^2$) *HST* combined Advanced Camera for Surveys and Wide Field Camera F435W image of NGC 0708, with CO(2–1) integrated intensity contours overlaid in blue and 236 GHz continuum contours overlaid in magenta. The synthesised beam ($\approx 0\farcs088$ or ≈ 25 pc) is shown in the bottom-left corner.

5.2 OBSERVATIONS

NGC 0708 and Abell 262 have been observed many times with in the CO wavebands by the Institut de Radioastronomie Millimétrique (IRAM) 30-m telescope, firstly by Edge (2001) who publish 3 observations, two at 113.45 GHz, $21\farcs2$ beamsize and one at 226.9 GHz with $10\farcs6$ beamsize. Edge (2001) calculate a molecular gas mass of $(9 \pm 1.3) \times 10^8\,\mathrm{M}_\odot$ and a beam temperature ratio of CO(2–1)/CO(1–0)=0.25. Salomé & Combes (2003) only detected CO(1–0) and calculated a lower molecular gas mass of $(2.3 \pm 0.3) \times 10^8\,\mathrm{M}_\odot$ due to identifying a line with a smaller width. Finally Ocaña Flaquer et al. (2010) also only detected CO(1–0) and calculate a mass of $(5.25 \pm 0.88) \times 10^8\,\mathrm{M}_\odot$.

NGC 0708 was observed three times as part of the mm-Wave Interferometric Survey of Dark Object Masses (WISDOM) project, aiming to measure its central SMBH mass. Previous work (e.g. Woo & Urry 2002; Donato et al. 2004) suggested an SMBH mass $M_{\mathrm{BH}} \approx 2.9 \times 10^8\,\mathrm{M}_\odot$. Olivares et al. (2019) published our initial low resolution CO(2–1) observations from ALMA in a study of filaments in cool core clusters. The observations at $0\farcs95 \times 0\farcs61$ ($268 \times 172\,\mathrm{pc}^2$) show no filaments but a slightly warped rotating kilo-parsec scale disc of molecular gas. Here we study this source in detail by including both new high-resolution ALMA data, and lower resolution compact array observations from WISDOM.

5.2.1 ALMA OBSERVATIONS

As part of the WISDOM project, ALMA observed the ^{12}CO(2–1) line in NGC 0708 three times, first under programme 2015.1.00598.S at moderate angular resolution ($0\farcs52$ or ≈ 146 pc) on June 27th 2016 (published in Olivares et al. 2019), and then under programme 2017.1.00391.S at $0\farcs25$ (≈ 70 pc) resolution on November 12th 2017 and $0\farcs03$ (≈ 8.5 pc) resolution on September 19th 2018. The science target integration times for these were 11, 19 and 37 min, respectively. The baselines ranged from 15 m to 14 km, achieving sensitivity up to a largest angular scale of $7''$ (≈ 2 kpc) to cover the extent of the dust feature. For all observations a 1870 MHz ($\approx 2500\,\mathrm{km\,s^{-1}}$) correlator window was centred at 226.8 GHz (the redshifted ^{12}CO(2–1) line frequency) with a raw channel width of ≈ 976.5 kHz ($\approx 1.87\,\mathrm{km\,s^{-1}}$). To detect continuum emission, three additional low spectral resolution correlator windows were included, each with a bandwidth of ≈ 2 GHz.

The raw data were calibrated using the standard ALMA pipeline, as provided by the European ALMA Regional Centre staff. The calibrators used for all observations were J0237+2848 for flux and bandpass calibration and J0205+3212 for phase calibration. The three observation tracks were combined and imaged using the COMMON ASTRONOMY SOFTWARE APPLICATIONS (CASA; McMullin et al. 2007). Continuum emission from the AGN was detected, measured over the full line-free bandwidth, and then subtracted from the data in the *uv*–plane using the CASA task UVCONTSUB. Both the line and continuum cubes were cleaned and imaged using the CASA task TCLEAN and Briggs weighting with a robust parameter of 0.5. They were then primary beam corrected. The imaging achieved a synthesised beam size of full-width at half-maximum (FWHM) $0\farcs088 \times 0\farcs083$ ($\approx 25 \times 23\,\mathrm{pc}^2$) for the ^{12}CO(2–1) line and $0\farcs088 \times 0\farcs087$ ($\approx 25 \times 25\,\mathrm{pc}^2$) for the continuum. To produce the final three-dimensional ^{12}CO(2–1) RA-Dec.-velocity data cube, the data were binned to $10\,\mathrm{km\,s^{-1}}$ channels and $0\farcs035 \times 0\farcs035$ pixels (≈ 3 pixels across the synthesised beam major axis ensures Nyquist sampling). This ^{12}CO(2–1) cube has a root mean square (rms) noise of $0.41\,\mathrm{mJy\,beam^{-1}}$ in each $10\,\mathrm{km\,s^{-1}}$ channel.

Line emission

The moment maps, shown in Fig. 5.2, were created using the smooth-mask technique (e.g. Dame, 2011). The mask was generated by taking a copy of the cleaned, primary beam-corrected cube and smoothing it, first spatially using a Gaussian of FWHM equal to that of the synthesised beam, and then spectrally using a Gaussian of FWHM of 4 channels. The mask selects pixels with an amplitude in the smoothed cube greater than 1.1 times the rms noise of the un-smoothed cube. The mask is then applied to the un-smoothed cube to create the moment maps. Having said that, all quantitative analyses reported in this chapter were performed using the un-smoothed, un-masked cube.

The zeroth (integrated intensity) and first (intensity-weighted mean line-of-sight velocity) moment maps reveal a rotating but warped molecular gas disc (see left and central panel Fig. 5.2). The moment zero is also shown in the bottom panel of Fig. 5.1 (blue contours), overplotted on a *HST* image, revealing that the molecular gas is coincident with dust features. The second moment (intensity weighted line-of-sight velocity dispersion; right panel Fig. 5.2) shows evidence of disturbance, with an off-centre peak significantly away ($\approx 0\farcs4$ or $\approx 113\,\mathrm{pc}$) from the AGN position (that can also be independently measured from the 236 GHz continuum emission presented here; see Section 5.2.1). A major-axis position-velocity diagram (PVD; Fig. 5.3) was created by taking a 3-pixel wide pseudo-slit across the kinematic major axis of the cube, at a position angle of 349°. This position angle was estimated by eye and agrees with that found by Pandya et al. (2017) for the ionised-gas disc traced by [O III]. On the approaching side, the PVD has a sharp increase in velocity at a radius of $\approx 0\farcs4$ ($\approx 113\,\mathrm{pc}$), co-spatial with the aforementioned increase in velocity dispersion (see the right panel of Fig. 5.2 and the blue ellipse in Fig. 5.3).

The global spectrum, shown in Fig. 5.4, was created by binning up the data to $20\,\mathrm{km\,s^{-1}}$ channels and then integrating over the whole molecular gas disc, i.e. a $6'' \times 6''$

($1.7 \times 1.7\,\mathrm{kpc}^2$) area of the cube. This spectrum clearly shows the characteristic double-horned profile of a rotating disc, but with hints of an additional blue-shifted wing (highlighted by the the magenta ellipse).

236 GHz continuum emission

As mentioned in Section 5.2.1, NGC 0708 also has 236 GHz continuum emission, detected by ALMA in the three low-resolution spectral windows and the line-free channels of the high-resolution spectral window. The emission is resolved and has an extension to the South, clearly revealed in the left panel of Fig. 5.5, showing the 236 GHz continuum emission (magenta contours) overlaid on the CO(2–1) velocity dispersion map. This highlights both the approximate coincidence between the extension of the continuum emission and the peak of the velocity dispersion, and the offset of that peak from the AGN position (i.e. the centre of the continuum emission). The magenta arrows in the left panel of Fig. 5.5 show the direction of the large-scale 330-MHz jet, to highlight the difference of orientation between that and the 236 GHz emission. The total 236 GHz continuum flux is 32.3 ± 0.2 mJy (1σ statistical uncertainty).

5.2.2 E-MERLIN 5 GHZ CONTINUUM EMISSION

The extension of the 236 GHz continuum emission in NGC 0708 is perpendicular to the large-scale jet (as traced by 330 MHz emission; see Figs. 5.1 and 5.5) and prompted us to obtain additional 5 GHz continuum data, to ascertain if the 236 GHz continuum is from a small (potentially restarted) jet. NGC 0708 was thus observed twice with e-MERLIN, the data providing sensitivity to 5 GHz emission distributed on the same angular scales as the 236 GHz data presented in this chapter. The e-MERLIN data were processed through the standard e-MERLIN CASA pipeline (eMCP*) by the e-MERLIN facility staff. The calibrators used were 0152+3616 for phase, 0319+4130 for pointing, 1331+3030 for flux and 1407+2827 for bandpass calibration. The total on-source integration time was 14.5 hours.

I additionally performed self-calibration to increase the sensitivity. The self-calibration involved 2 cycles, the first considering phase only, averaging over 240 s intervals, the second with phase and amplitude. I imaged the data in CASA using the TCLEAN task, with a Briggs weighting robust parameter of 0.5 to balance sensitivity and resolution. This yielded a synthesised beam size of $0\farcs07 \times 0\farcs03$ ($\approx 20 \times 8\,\mathrm{pc}^2$) and a rms noise of $0.12\,\mathrm{mJy\,beam}^{-1}$.

I detect a 5 GHz point source at the expected position of the SMBH in NGC 0708. I confirmed this source is spatially unresolved using the CASA task IMFIT, that fits a Gaussian to the image, deconvolved from the synthesised beam. The integrated flux at 5 GHz

*https://github.com/e-merlin/eMERLIN_CASA_pipeline

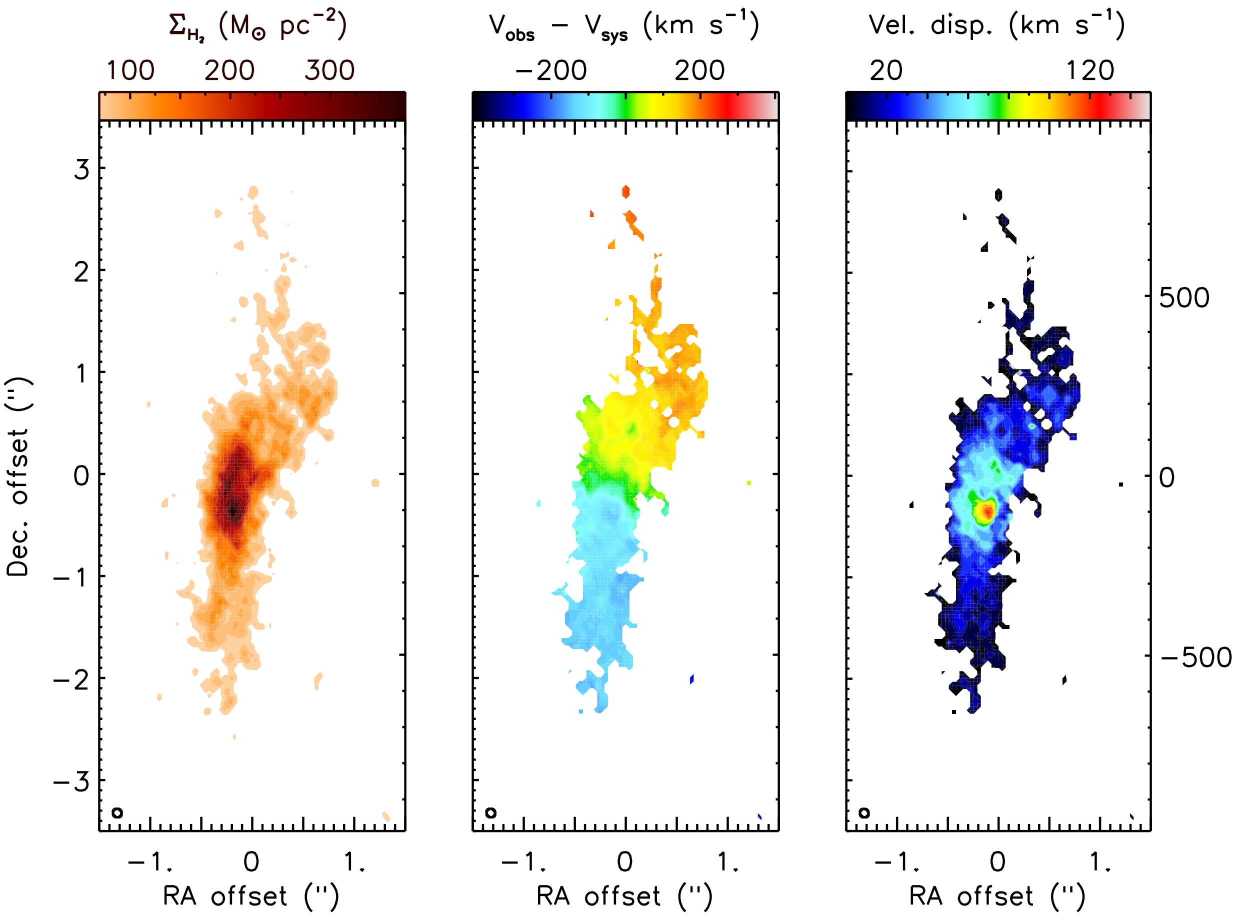

Figure 5.2. ^{12}CO(2–1) moment maps of NGC 0708. *Left panel:* moment zero (integrated intensity) map, assuming a line ratio CO(2–1)/CO(1–0)=1 and a CO-to-H$_2$ conversion factor $\alpha_{\rm CO} = 4.6\,{\rm M}_\odot$ (K km s^{-1})$^{-1}$ pc^{-2}. *Central panel:* moment one (intensity-weighted mean line-of-sight velocity) map, assuming a systemic velocity $V_{\rm sys} = 4750$ km s^{-1}. *Right panel:* moment two (intensity-weighted line-of-sight velocity dispersion) map. Note the off-centre velocity dispersion peak. The ellipse in the bottom-left corner of each panel shows the synthesised beam ($0\farcs088 \times 0\farcs083$ or $\approx 25 \times 23$ pc^2). RA and Dec. offsets are relative to the centre of the continuum emission, located at RA $= 01^{\rm h}52^{\rm m}46\fs48$ and Dec. $= +36^\circ09'06\farcs6$.

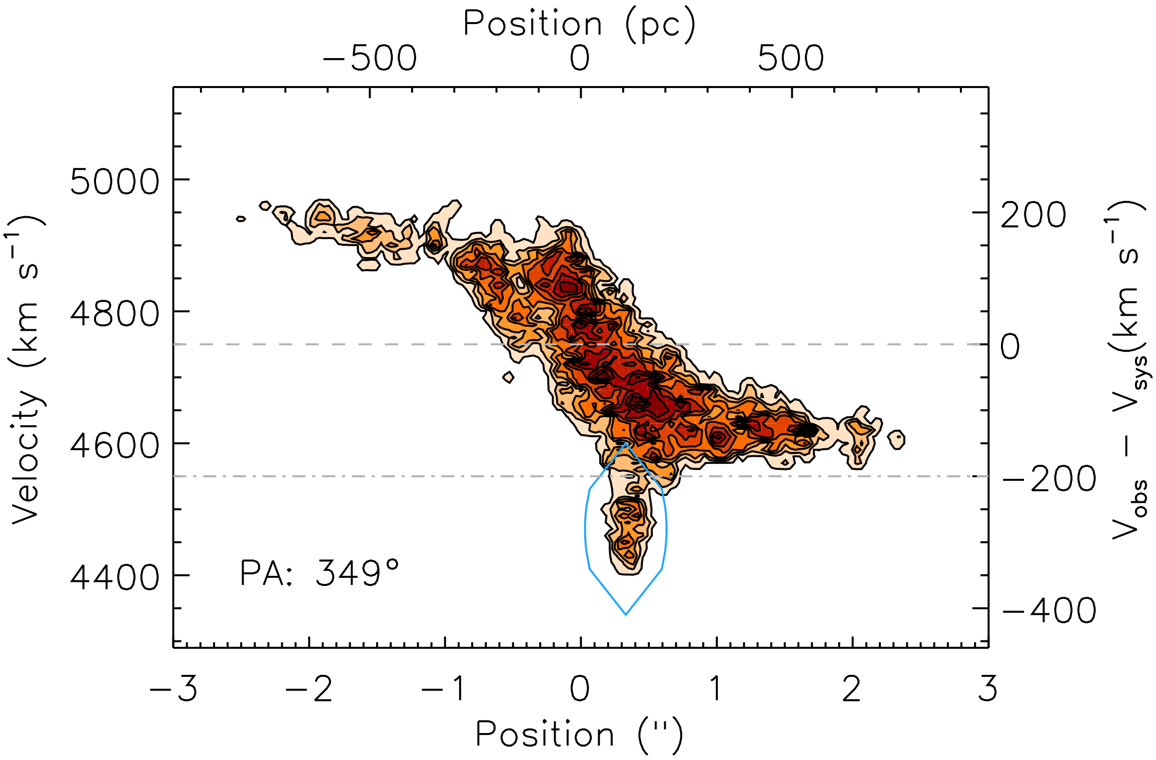

Figure 5.3. ^{12}CO(2–1) kinematic major-axis position-velocity digram of NGC 0708, taken at a position angle of 349°. The grey dashed line denotes the systemic velocity, $V_{\rm sys} = 4750\,{\rm km\,s^{-1}}$. The grey dot-dashed line denotes the velocity cut used to isolate the blue-shifted feature ($V_{\rm obs} = 4550\,{\rm km\,s^{-1}}$; see Section 5.3.1) The cyan polygon highlights the blue-shifted feature.

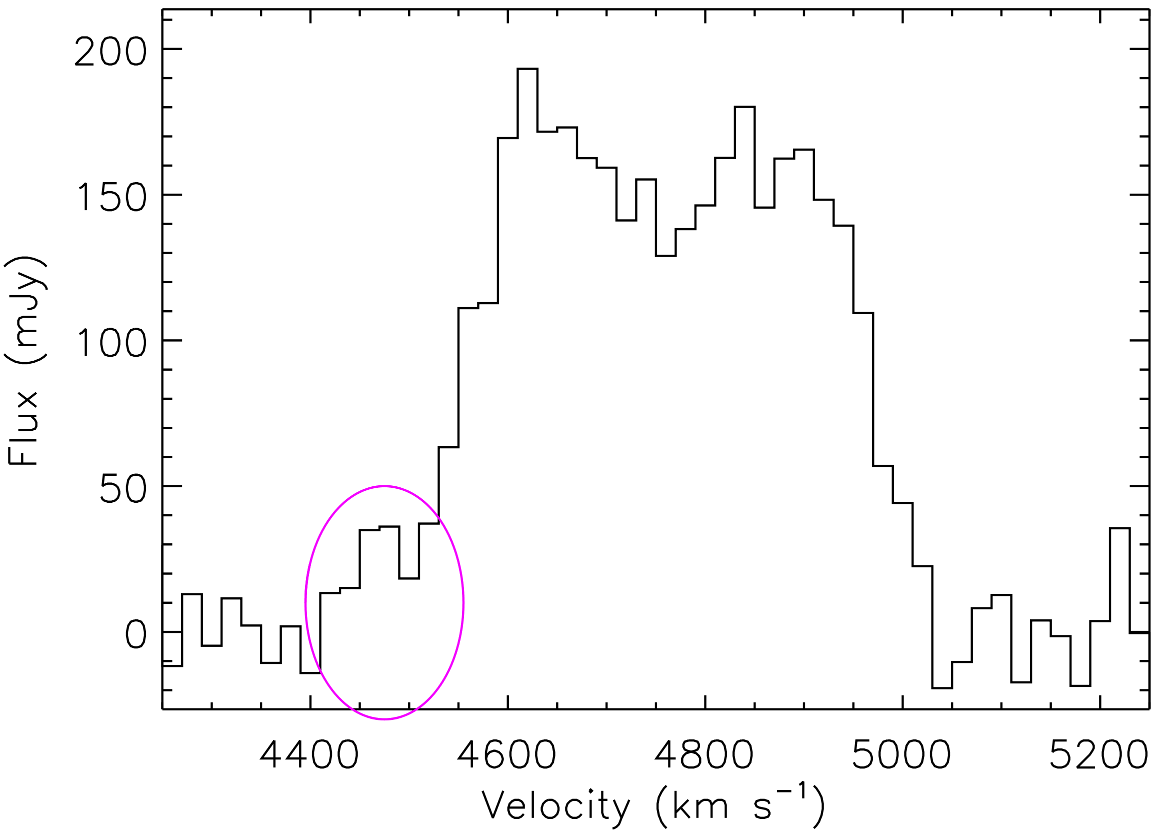

Figure 5.4. ^{12}CO(2–1) integrated spectrum of NGC 0708 binned to 20 km s^{-1} channels, showing the characteristic double-horned shaped of a rotating disc. The blue-shifted wing is highlighted by the magenta ellipse.

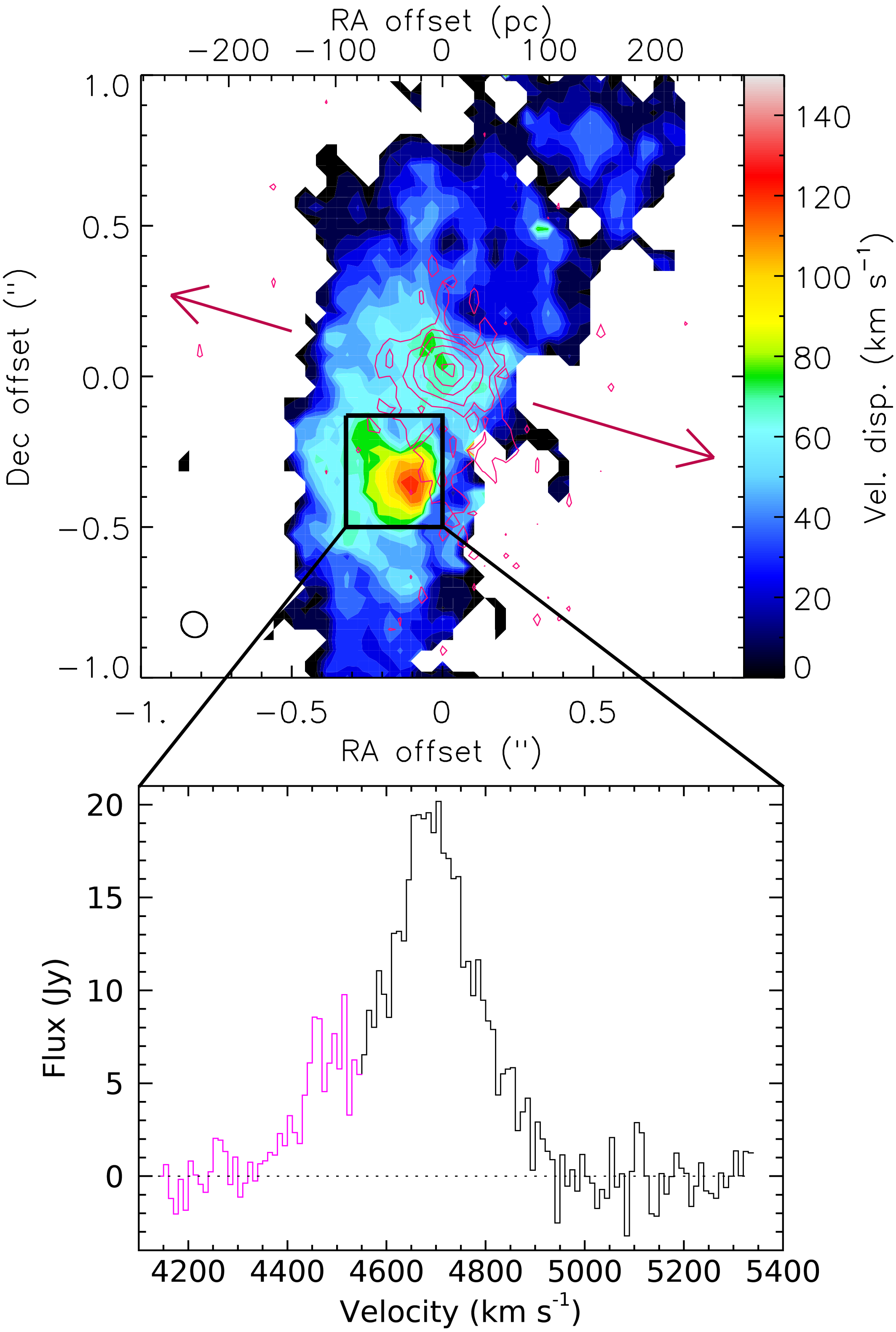

Figure 5.5. *Top panel:* ^{12}CO(2–1) Moment 2 map of NGC 0708, with 236 GHz continuum emission isophotes overlaid in magenta. The magenta arrows indicate the direction of the large-scale jet traced by 330 MHz emission. The extension of the 236 GHz continuum emission matches well the position of the velocity dispersion peak. *Bottom panel:* ^{12}CO(2–1) spectrum integrated over the spatial area of the outflow (indicated by a black box in the left panel), with gas satisfying the outflow velocity criterion ($V_{\rm obs} < 4550$ km s^{-1}) indicated in magenta.

is 5.25 ± 0.21 mJy (1σ statistical uncertainty). This is ≈ 5 times smaller than that measured by Clarke et al. (2009) at 5 GHz with the VLA on $\approx 4''$ (≈ 1.1 kpc) scales and $6-8$ times smaller than single-dish 5 GHz measurements ($\approx 2\farcm6$ or ≈ 44 kpc scales, Andernach et al. 1980; $\approx 10'$ or ≈ 170 kpc scales, Gregory et al. 1996). The disparity between these measurements and that presented in this chapter suggests that significant 5 GHz emission is associated with the large-scale radio jet, that I resolve out here. There is no obvious small-scale (restarted) jet visible, at least at 5 GHz, suggesting that either such a feature is not present, or its 5 GHz flux is very low (and its 236–5 GHz spectral index is very flat or inverted).

5.3 RESULTS

Our ALMA data enable us to spatially and kinematically separate distinct components of the molecular gas distribution, and thereby investigate the unusual blue-shifted feature observed in NGC 0708. The velocity dispersion map (right panel of Fig. 5.2) and PVD (Fig. 5.3) indeed clearly indicate two kinematically-distinct components, a regularly rotating disc and the blue-shifted feature.

The total ^{12}CO(2–1) flux detected in NGC 0708 is 68.4 ± 0.1 Jy km s^{-1} (1σ statistical uncertainty). It should be noted that there is also a 10 percent systematic flux calibration uncertainty, that would dominate the statistical uncertainty but is not propagated through the following numbers. I assume a typical Milky Way-like CO-to-H_2 conversion factor $\alpha_{\rm CO} = 4.6\,{\rm M_\odot}\,({\rm K\,km\,s^{-1}})^{-1}\,{\rm pc^{-2}}$ and use the line ratio $L'_{\rm CO(2-1)}/L'_{\rm CO(1-0)} = 0.25$ measured by Edge (2001). The total flux therefore corresponds to a total molecular gas mass $M_{\rm tot} = (3.86 \pm 0.01) \times 10^8\,{\rm M_\odot}$. The velocity field and PVD indicate most of the gas is in regular rotation in the gravitational potential of the galaxy. However, the blue-shifted feature detected, in particular in the PVD (Fig. 5.3), cannot arise from regularly-rotating material. The origin of this material is ambiguous, as both inflows and outflows can produce similar features. I must therefore turn to other wavelengths to elucidate its source. Here I begin the discussion of what could cause the anomalous emission observed and then continue the discussion in Section 5.4 having performed some analysis of the emission.

Inflows are often associated with gas cooling onto galaxies and with mergers. Gas cooling on to isolated or satellite galaxies tends to be slow and to occur primarily along the disc plane (see e.g. the simulations by Agertz et al. 2009 and Stewart et al. 2011). It would then most prominently appear in the moment 1 map as gas in the outer disc that is not following the expected rotation pattern. However, I see in NGC 0708 a well-collimated velocity signature, indicating that a significant component of the velocity is along the line of sight, i.e. *out* of the plane of the disc. The blue-shifted feature is also very close to the centre of the galaxy, implying that this kind of gas inflow is unlikely.

Mergers tend to be distinguishable most readily in optical images, by the warped morphology of the galaxy and tidal tails of gas and stars, as gas inflowing on to the more massive galaxy tends to form tidal tails extending over many kiloparsecs. In contrast, *HST* imaging of NGC 0708 (Fig. 5.1) shows no sign of a very recent merger, with no tidal tail and only a mildly-warped dust disc. The PVD feature detected by ALMA is well collimated and extends radially to ≈ 100 pc. Such a small, localized feature is unlikely to arise from a tidal tail. Therefore, although I cannot rule it out definitely, the collimation, size and position of the blue-shifted feature indicate that secular or merger driven inflow is an unlikely explanation.

This, however, leaves the most likely possibility. NGC0708 is a brightest cluster galaxy which is expected to be fuelled by a cooling flow. Molecular gas clumps and filaments are expected to be precipitating out of the hot medium and raining down onto the galaxy. In large samples of observed BCGs these in-falling systems are common, with multiple typically being found around each BCG (e.g. Olivares et al., 2019). These in-falling filements typically contain a large fraction of the total molecular gas mass. To assess the credibility of this explanation I will compare to the Olivares et al. (2019) sample later on.

The other option for the origin of the blue-shifted feature is an outflow. Outflows can be caused by massive star-, supernova- and/or AGN-driven winds as well as by jets directly impacting onto the ISM gas. Supernova- and AGN-driven winds tend to be large scale and are expected to be roughly isotropic, depending on the gas structure around the star-forming region or AGN. To lead to the feature shown in Fig. 5.3, the wind would have to be very localised, or currently only interacting with a single (or at most a few) giant molecular cloud(s), an unlikely scenario. The feature is also offset from the AGN position as traced in 236 and 5 GHz continuum emission ($\approx 0\farcs4$ or ≈ 113 pc; see the left-hand panel of Fig. 5.5), making it unlikely to be a wind-driven outflow from the central AGN.

The off-centre position of the feature could also indicate a binary black hole system, with a dual AGN. However neither radio nor X-ray observations detect accretion onto a second SMBH at this position, setting a stringent upper limit on the accretion power available to drive an outflow. Radio and X-ray data only detect a single point source at the photometric centre of the galaxy, where the continuum emission presented in this chapter is also detected (see Section 5.2.1 and 5.2.2).

AGN jets, on the other hand, are well collimated, strongly directional and can do work significantly away from the centres of galaxies, corresponding closely to the characteristics of the feature I observe. As mentioned previously, an AGN driven jet is detected in NGC 0708 at 330 MHz, but it is too large and not at the correct orientation to drive the putative outflow associated with the blue-shifted feature. Whilst I do not detect a jet on the correct spatial scales at 5 GHz, there is a hint of one at higher frequencies (the Southern extension to the 236.6 GHz emission discussed in Section 5.2.1; see also Fig. 5.5), and the repeating precessing jets detected by Clarke et al. (2009) in this object suggest the jet-driven explanation is plausible. The blue-shifted feature is also very similar to the jet-driven molecular gas outflow found in the Seyfert 2 galaxy IC 5063 by Morganti et al. (2015), who observed a similarly jagged PVD with large deviations from the rotational velocity at one specific off-centre position. Fernández-Ontiveros et al. (2020) also discovered a molecular gas outflow in the Seyfert 2 galaxy ESO 420 G13, by detecting a velocity dispersion peak 440 pc from the galaxy centre, similar to the one detected here (see the right-hand panel of Fig. 5.2).

Once I have calculated the properties of the blue-shifted feature I will continue the discussion of whether it is an inflow or outflow and what is causing it.

5.3.1 BLUE-SHIFTED FEATURE PROPERTIES

I now determine the properties of the blue-shifted feature, as I wish to compare it to Morganti et al. (2015) and Cicone et al. (2014) I will follow a lot of their analysis. I begin by isolating the gas in the outflow from that in the main gas disc. I constrain its spatial extent to that of the velocity dispersion peak seen in Fig. 5.2, adopting the region $-0\farcs32 <$ RA offset $< 0''$ and $-0\farcs52 <$ Dec. offset $< -0\farcs13$ (see the black box in Fig. 5.5) relative to the centre of the continuum point source (RA $= 01^{\rm h}52^{\rm m}46\fs48$, Dec. $= +36^{\circ}09'06\farcs6$). In velocity, I impose $V_{\rm obs} < 4550\ {\rm km\,s^{-1}}$, indicated in the PVD (Fig. 5.3) by a grey dot-dashed line.

Our observations only reveal a blue-shifted outflow, while I would typically expect outflows to be symmetrical. However, I do not know the launch velocity of the outflow, and hence the red-shifted side of the outflow may be lost amongst the emission from the bulk of the rotating disc. I thus only consider the gas I can robustly conclude is contained within the blue-shifted outflow, but I caution that the actual outflow mass, mass outflow rate and other derived quantities may be underestimated, likely by a factor of ≈ 2.

The right-hand panel of Fig. 5.5 shows the ^{12}CO(2–1) spectrum of the adopted outflow spatial region, with the channels satisfying the adopted velocity criterion (i.e. the blue-shifted wing) highlighted in magenta. The spectrum of this region has a ^{12}CO(2–1) integrated flux of 4.86 ± 0.11 Jy km s^{-1}, while the flux associated with the outflow only (magenta channels in the integrated spectrum in the right panel of Fig. 5.5) is 0.92 ± 0.05 Jy km s^{-1} (both 1σ statistical uncertainty).

The opacity and density of the gas in the outflow is unknown, so I will conduct the analysis with three representative values of $\alpha_{\rm CO}$ (following Morganti et al. 2015): a typical local/Milky Way value ($\alpha_{\rm CO,\,galactic} = 4.6\,{\rm M_\odot\,(K\,km\,s^{-1})^{-1}\,pc^{-2}}$, as assumed for the bulk of the gas), a value appropriate for the disturbed gas typically found in ultra-luminous infrared galaxies (ULIRGs; $\alpha_{\rm CO,\,ULIRG} = 0.8\,{\rm M_\odot\,(K\,km\,s^{-1})^{-1}\,pc^{-2}}$) and a value appropriate for optically thin gas ($\alpha_{\rm CO,\,thin} = 0.34\,{\rm M_\odot\,(K\,km\,s^{-1})^{-1}\,pc^{-2}}$; see discussions of $\alpha_{\rm CO}$ in Bolatto et al. 2013 and Geach et al. 2014). I further assume a line ratio $L^{'}_{\rm CO(2-1)}/L^{'}_{\rm CO(1-0)} = 1$ (e.g. Solomon & Vanden Bout 2005). I will also compare different assumptions about the outflow geometry, leading to upper and lower limits on the mass outflow rate, but will not at the moment make assumptions about the cause of the outflow.

Lutz et al. (2020) compare three different outflow histories. The first and simplest assumption is that of a constant mass outflow rate $\dot{M}_{\rm OF}$, i.e.

$$\left(\frac{\dot{M}_{\rm OF,\,const}}{\rm M_\odot\,yr^{-1}}\right) = \left(\frac{V_{\rm ave}}{\rm m\,yr^{-1}}\right)\left(\frac{M_{\rm OF}}{\rm M_\odot}\right)\left(\frac{R_{\rm OF}}{\rm m}\right)^{-1}, \tag{5.1}$$

where $M_{\rm OF}$ is the total outflow mass (see Table 5.1), $R_{\rm OF} = 0\farcs4 \pm 0\farcs1$ (113 ± 28 pc or $\approx (3.48 \pm 0.87) \times 10^8$ m) is the galactocentric radius of the outflow, and $V_{\rm ave}$ is the average velocity of the outflow, taken as the median velocity of the outflow signature. For NGC 0708, I estimate $V_{\rm ave} = 300 \pm 10\,{\rm km\,s^{-1}}$ or $\approx (9.47 \pm 0.22) \times 10^{12}\,{\rm m\,yr^{-1}}$ from the integrated outflow spectrum (right panel of Fig. 5.5).

Secondly, I assume a constant average volume mass density in the spherical or multi-conical region affected by the outflow, requiring a decaying mass outflow rate (as used by Cicone et al. 2014). This leads to a mass outflow rate three times the constant mass outflow rate, i.e.

$$\left(\frac{\dot{M}_{\rm OF,\,Cicone}}{\rm M_\odot\,yr^{-1}}\right) = 3\left(\frac{V_{\rm ave}}{\rm m\,yr^{-1}}\right)\left(\frac{M_{\rm OF}}{\rm M_\odot}\right)\left(\frac{R_{\rm OF}}{\rm m}\right)^{-1}. \tag{5.2}$$

Finally I assume the outflow is a thin shell, where the thickness of the shell ($\Delta R_{\rm out}$) replaces the total radius from the centre, i.e.

$$\left(\frac{\dot{M}_{\rm OF,\,thin\,shell}}{\rm M_\odot\,yr^{-1}}\right) = \left(\frac{V_{\rm ave}}{\rm m\,yr^{-1}}\right)\left(\frac{M_{\rm OF}}{\rm M_\odot}\right)\left(\frac{\Delta R_{\rm OF}}{\rm m}\right)^{-1}. \tag{5.3}$$

I adopt $\Delta R_{\rm out} = 0\farcs3 \pm 0\farcs1$ (85 ± 28 pc or $\approx (2.61 \pm 0.87) \times 10^8$ m) for NGC 0708 based on Fig. 5.3, measuring the thickness of the blue-shifted feature. I note that this feature is barely resolved spatially, so $\Delta R_{\rm out}$ is likely a slight overestimate.

The mass outflow rates from these three assumed geometries are compared in Table 5.1, along with the kinetic power of each geometry as described below.

To investigate the power source behind this outflow, I can compare its kinetic power to that of other processes within the galaxy, for instance star formation or the AGN. To calculate the kinetic power of the outflow ($P_{\rm kin,OF}$), I use Equation 7 of Holt et al. (2006) rescaled to CO(2–1) from [O III] by Morganti et al. (2015, see their Eq. 1). Following both papers, I assume the relatively large line width of the outflowing gas reflects turbulent motion over the whole outflow, so that the FWHM of the CO line represents the turbulent component of the outflow:

$$\left(\frac{P_{\rm kin,\,OF,\,Holt}}{\rm erg\,s^{-1}}\right) = 3.17\times10^{35}\left(\frac{\dot{M}_{\rm OF}}{\rm M_{\odot}\,yr^{-1}}\right)\left[\left(\frac{V_{\rm ave}}{\rm km\,s^{-1}}\right)^{2}+0.18\left(\frac{V_{\rm turb}}{\rm km\,s^{-1}}\right)^{2}\right], \quad (5.4)$$

where I again adopt $V_{\rm ave}\approx300\pm10\,{\rm km\,s^{-1}}$ and $V_{\rm turb}\approx$ FWHM $\approx 100\pm10\,{\rm km\,s^{-1}}$ from the integrated outflow spectrum (right panel of Fig. 5.5). This equation is applied using the three mass outflow rates considered above and the results are listed in Table 5.1.

Equation 5.4 includes terms concerning both the radial and turbulent components of gas motion, but in later sections I will compare my estimates with those of Cicone et al. (2014), who only include the radial motion:

$$\left(\frac{P_{\rm kin,\,OF,\,Cicone}}{\rm erg\,s^{-1}}\right) = 3.17\times10^{35}\left(\frac{\dot{M}_{\rm OF}}{\rm M_{\odot}\,yr^{-1}}\right)\left(\frac{V_{\rm ave}^{2}}{\rm km\,s^{-1}}\right). \quad (5.5)$$

I use this equation with the mass outflow rate from Equation 5.2 only when comparing with the measurements of Cicone et al. (2014) in Section 5.4.3.

The linear momentum rate of the outflow is $\dot{p}_{\rm OF} = V_{\rm ave}\dot{M}_{\rm OF}$ (Cicone et al., 2014). Again I use this equation with the mass outflow rate from Equation 5.2 only when comparing with the measurements of Cicone et al. (2014) in Section 5.4.3.

Table 5.1 lists the outflow mass, mass outflow rate, kinetic power and momentum rate derived for each assumed $\alpha_{\rm CO}$ and each outflow history using the above equations. The inclusion of the turbulent velocity in Equation 5.4 increases the kinetic power by only ≈ 2 percent.

I have argued that an AGN jet is the most likely origin of the outflow, so the thin outflowing shell model discussed above is likely the most physically accurate, as direct impact from a collimated jet would move a thin shell of material. In addition, whilst the observations presented here cannot exclude other models, the small physical size and offset of the velocity dispersion peak (see the right panel of Fig. 5.2) may indicate a thin shell is forming. I will therefore adopt the thin shell model for discussion in this chapter, in particular to compare the NGC 0708 outflow with those observed in other galaxies (Section 5.4.2). Under the thin shell assumption, the depletion time (i.e. the time taken for the

Table 5.1. Derived outflow properties

		$\alpha_{\rm CO,\,thin}$ (1)	$\alpha_{\rm CO,\,ULIRG}$ (2)	$\alpha_{\rm CO,\,galactic}$ (3)
Outflow mass	$M_{\rm OF}$ ($10^5\,{\rm M_\odot}$)	3.82 ± 0.02	8.99 ± 0.05	51.71 ± 0.30
Mass outflow rate	$\dot{M}_{\rm OF,\,const}$ (${\rm M_\odot\,yr^{-1}}$)	1.039 ± 0.268	2.44 ± 0.63	14.06 ± 3.62
	$\dot{M}_{\rm OF,\,thin\,shell}$ (${\rm M_\odot\,yr^{-1}}$)	1.38 ± 0.47	3.26 ± 1.11	18.74 ± 6.35
	$\dot{M}_{\rm OF,\,Cicone}$ (${\rm M_\odot\,yr^{-1}}$)	3.12 ± 0.80	7.33 ± 1.88	42.17 ± 10.81
Kinetic power	$P_{\rm kin,\,OF,\,Holt,\,const}$ ($10^{40}\,{\rm erg\,s^{-1}}$)	3.02 ± 0.81	7.11 ± 1.91	40.91 ± 10.97
	$P_{\rm kin,\,OF,\,Holt,\,thin\,shell}$ ($10^{40}\,{\rm erg\,s^{-1}}$)	4.03 ± 1.40	9.49 ± 3.29	54.54 ± 18.93
	$P_{\rm kin,\,OF,\,Holt,\,Cicone}$ ($10^{41}\,{\rm erg\,s^{-1}}$)	0.91 ± 0.24	2.13 ± 0.57	12.27 ± 3.28
	$P_{\rm kin,\,OF,\,Cicone}$ ($10^{41}\,{\rm erg\,s^{-1}}$)	0.89 ± 0.30	2.09 ± 0.70	12.03 ± 4.04
Momentum rate	$\dot{p}_{\rm OF}$ ($10^{34}\,{\rm g\,cm\,s^{-2}}$)	0.59 ± 0.15	1.40 ± 0.36	8.02 ± 2.07

Note: Outflow mass, mass outflow rate, kinetic power and momentum rate for each of (1) optically-thin $\alpha_{\rm CO}$, (2) optically-thick ULIRG $\alpha_{\rm CO}$ and (3) local/Milky Way $\alpha_{\rm CO}$. Uncertainties are quoted at 1σ.

outflow to remove all the molecular gas from the galaxy assuming it continues at its current rate) is $\tau_{\rm dep,\,OF} \equiv M_{\rm tot}/\dot{M}_{\rm OF,\,thin\,shell} = (2.061 \pm 0.699) \times 10^7$ yr (note the $\alpha_{\rm CO}$ is the same for both the total mass and the mass outflow rate).

5.3.2 SMBH MASS

The original goal of the observations presented here was to estimate the mass of the SMBH in NGC 0708. As shown in Figs. 5.1 and 5.2, the gas in the galaxy is warped and disturbed (especially in the outer regions), and it does not lie in the equatorial plane, making this difficult.

Despite this, the kinematics of the gas in the very centre of NGC 0708 (around the AGN/continuum source seen; see Figs. 5.2 and 5.5) seem fairly regular. Given the short dynamical times in this region, it is possible that this gas is sufficiently relaxed to allow us to constrain the central potential reasonably accurately.

From the red-shifted side of the PVD, that appears fairly undisturbed by the outflow (see Fig. 5.3), we can make a crude estimate of the total mass enclosed within the innermost radius probed. At $\approx 0\farcs088$ (one synthesised beam major axis from the galaxy centre) the projected rotational velocity is $\approx 180\,{\rm km\,s^{-1}}$, yielding an enclosed mass $\approx 2.2 \times 10^8\,{\rm M_\odot}$ (assuming pure rotation, i.e. $M_{\rm enc} = v^2(r)r/G$, where $v(r)$ is the rotational velocity at radius r and G is the gravitational constant). The total molecular gas mass within this radius is $\approx 5.16 \times 10^6\,{\rm M_\odot}$, and from the *HST* F110W image we can estimate a stellar mass within the same radius of $\approx 3 \times 10^6\,\mathrm{M}_\odot$ (assuming a very conservative F110W-band mass-to-light ratio of 2; e.g. see Fig. 11 of Balogh et al. 2001). This suggests a total dark-mass of $2.12 \times 10^8\,\mathrm{M}_\odot$ at the centre of NGC 0708.

While this rough estimate is very uncertain due to the unknown degree of kinematic disturbance in the gas (and approximate stellar mass-to-light ratio, absence of dust correction and standard CO-to-H_2 conversion factor), it is consistent with the SMBH mass estimated from the $M_{\mathrm{BH}} - \sigma$ relation by Woo & Urry (2002) and Donato et al. (2004) based on central stellar velocity dispersions. Woo & Urry (2002) use $\sigma = 241\,\mathrm{km\,s^{-1}}$to obtain $M_{\mathrm{BH}} = 2.88 \times 10^8\,\mathrm{M}_\odot$.

The Eddington luminosity of a black hole of this mass is $L_{\mathrm{Edd}} \approx 2.67 \times 10^{46}\,\mathrm{erg\,s^{-1}}$. In comparison, Clarke et al. (2009) estimated the total AGN kinetic luminosity to be $L_{\mathrm{AGN,kin}} = 6.2 \times 10^{42}\,\mathrm{erg\,s^{-1}}$. As a percentage of the Eddington luminosity this suggests the SMBH in NGC 0708 is currently only accreting at ≈ 0.023 percent of the Eddington rate.

5.4 DISCUSSION

I began in Section 5.3 the discussion of what movement of gas could cause the blue-shifted feature seen in the line emission. The options appear to stand at cooling flow precipitation, AGN-wind outflow or jet-powered outflow. I will now dicuss and compare these options.

I begin with inflow, as mentioned previously Abell 262 is a well known cooling flow and therefore expected to host precipitation filaments. Following Olivares et al. (2019) I compare the molecular gas fraction contained in the in-falling filament with the cooling rate of the hot intra-cluster medium, assuming $\alpha_{\mathrm{CO,galactic}}$. This is done in Fig. 5.6, which shows the data presented in Olivares et al. (2019, blue points) and the data for NGC 0708 as an orange star. NGC 0708 shows clear evidence for a single filament, containing a very small amount of the molecular gas in the system and appears as an outlier to the Olivares et al. (2019) sample. This implies the putative inflow seen in NGC 0708 is different from the majority of cooling flow molecular gas filaments. It should be noted however, that Abell 262 does have the lowest observed cooling rate in the sample observed and that these kind of detections require high sensitivity and high spatial resolution. It is possible that the singular low mass inflowing filament I observe in NGC 0708 is typical of a cluster with such a low cooling rate.

In order to match the observed velocity structure of this blue-shifted feature (which extends over $\gtrsim 200\,\mathrm{km\,s^{-1}}$ while having a physical extension perpendicular to our line of

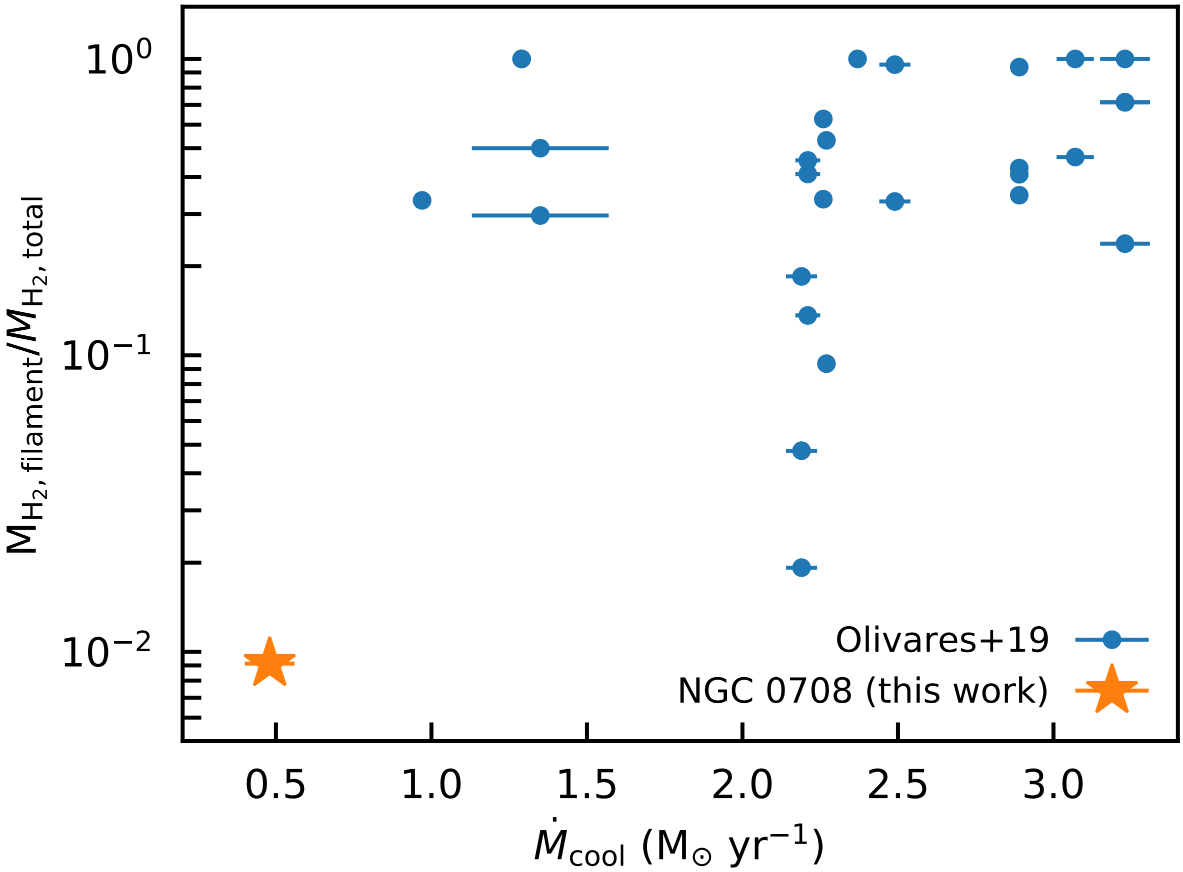

Figure 5.6. Fraction of the total H_2 mass contained within inflowing molecular filaments from Olivares et al. (2019), plotted as a function of the cooling rate of the hot intra-cluster medium in each galaxy cluster. NGC 0708 is shown as an orange star. This system has the lower cooling rate than other cluster objects, and also contains a much lower fraction of its cold molecular gas in potentially inflowing filaments.

sight of $\lesssim 66\,\mathrm{pc}$) it is clear that any such clump must have its own internal velocity structure. This is because (for any realistic potential) purely ballistic infall would require an extremely long column of gas, all perfectly aligned with our line of sight, in which molecular gas would not survive. Gaspari et al. (2018) performed simulations of the multiphase condensation cascade present in cooling flow clusters, and showed that their simulated condensing clumps can indeed have significant internal velocity gradients, which match those seen in observations of other cooling flow clusters. The blue-shifted feature I detect in NGC 0708 is well within the scatter of the observational data, and deviates from the expectation of the simulations at only a 1σ level.

Further evidence is present that could support a cooling-flow interpretation for this feature. For instance, the optical image of NGC 0708 shown in Figure 5.1 show that the dust in this system on larger scales is disturbed, and thus there may be other filaments in this system, which are not (yet) traced by molecular gas (although dust is expected to be destroyed on very short timescales in the hot ICM, so its presence here would require fast dust formation mechanisms; Clemens et al. 2010). Furthermore, the high velocity dispersion of the molecular gas disc of NGC 0708 could be caused by clumps, such as the one detected here, condensing out of the hot-ICM and raining down on the disc (I note, however, that this is not the only possible interpretation of this high dispersion; see below).

Overall I conclude that the blue-shifted material observed in NGC 0708 could be a low mass clump of material condensing out of the hot ICM and falling onto the core of this galaxy.

The other option for this anomalous emission is gas outflowing for the centre of NGC 0708, driven either by supernova- or AGN-driven winds or directly by the AGN jet. I will now perform a quantitative analysis of these options and compare what is observed in NGC 0708 to other molecular outflows.

5.4.1 KINETIC POWER COMPARISON

As mentioned in Section 5.3, the processes that could power a molecular gas outflow are an AGN- or supernova-driven wind and/or direct impact from an AGN jet. Whilst I concluded that a jet was the most likely cause of the outflow in NGC 0708, it is instructive to quantitatively compare the kinetic power of each process with that of the outflow. As I have previously commented, the geometry of the outflow in NGC 0708 is telling, and in what follows I consider this information alongside a quantitative analysis.

Supernova-driven winds are not expected to produce strongly collimated outflows and the off-nucleus position of the outflow in NGC 0708 would imply a very localised starburst event. The total star formation rate (SFR) of NGC 0708 was estimated by Davis et al. (2016) using its 22 μm luminosity and the calibration of Calzetti et al. (2007), yielding an upper limit of $0.15\,M_\odot\,yr^{-1}$. This is inconsistent with a starburst event. Using Equation 2 of Veilleux et al. (2005), this equates to a star formation kinetic power $< 10^{41}\,erg\,s^{-1}$, that would thus require an unusually large coupling factor with the gas of > 38 percent to explain the outflow (comparing to $P_{\rm kin,OF,Holt,thin\,shell}$ for the different $\alpha_{\rm CO}$). Even if all the supernovae of the entire galaxy went off at the unique right location, them causing this outflow would thus be highly unlikely.

The geometry of the outflow in NGC 0708 is also difficult to explain with a single AGN wind, as again the outflow is observed to be very collimated and off-centre. However, it is possible that this peculiar geometry tells us something about the molecular gas structure near the core (e.g. perhaps only one side of the molecular torus has been blown away due to density inhomogeneities). I can still compare the AGN wind kinetic luminosity with the kinetic power to quantitatively assess the AGN as the power source. As mentioned earlier Clarke et al. (2009) estimate this to be $L_{\rm kin,AGN} = 6.2 \times 10^{42}\,erg\,s^{-1}$, yielding a kinetic power coupling factor of 0.65-8.8 percent (depending on the $\alpha_{\rm CO}$), indicating that if the outflowing gas is optically thin then enough energy would be present to drive this outflow if the geometry were not an issue.

Other works studying large molecular outflows in early-type galaxies (e.g Alatalo et al. 2011; Aalto et al. 2012; Morganti et al. 2015; Fernández-Ontiveros et al. 2020) have suggested direct impact by a jet as the most viable power source. NGC 0708 has had multiple active jet-driving episodes with a ≥ 28 Myr cycle (Clarke et al. 2009). It is therefore plausible that a recent episode of activity, with a new jet, has caused the outflow. To ascertain if jets launched by NGC 0708 have enough energy to power the outflow, we calculate its jet power ($Q_{\rm jet}$). Equation 11 of Wu (2009) converts the radio luminosity at 151 MHz (L_{151}) to $Q_{\rm jet}$ (I follow their analysis and use a normalisation factor $f = 10$). NGC 0708 was observed as part of the 6th Cambridge (6C) survey at 151 MHz at a resolution of $\approx 7\overset{\prime}{.}2 \times 7\overset{\prime}{.}2$ ($\approx 120 \times 120\,{\rm kpc}^2$; Baldwin et al. 1985). The catalogue reports a peak flux of $L_{151} = 0.78 \pm 0.075$ Jy (Hales et al., 1993). The beam of these observations covers the whole of the old, large-scale jet in an unresolved manner, so I am forced to assume that an AGN restart would produce a jet of similar power. This assumption yields $Q_{\rm jet} = (1.32 \pm 0.01) \times 10^{43}\,erg\,s^{-1}$. This would require a coupling factor with the ISM of 0.3-4.1 percent (depending on $\alpha_{\rm CO}$) to cause the outflow identified here. These efficiencies are consistent with those of simulations, yielding jet-ISM energy transfer efficiencies of $0.1 - 0.8$ percent (e.g. Nesvadba et al. 2010; Wagner & Bicknell 2011).

The detection of extended radio emission at 236 GHz but only a point source at 5 GHz is also consistent with a jet scenario. The difference in flux then likely indicates the core has a very flat or even inverted spectral energy distribution. This is indicative of a young jet, where particles have recently been injected into the magnetic field (Clarke et al., 2009). Whilst I cannot prove that the extended 236 GHz emission I detect arises from a restarted young jet, the evidence does suggest that a jet-like mechanism is responsible for the molecular gas morphology and kinematics of NGC 0708, similarly to the scenario presented by Fernández-Ontiveros et al. (2020) for ESO 420-G13.

On the basis of these arguments, I surmise again that the blue-shifted feature seen in the PVD, with its off-centre location, is most likely an outflow caused by a jet originating in the AGN of NGC 0708.

5.4.2 COMPARISON WITH OTHER MOLECULAR OUTFLOWS

I now compare the mass outflow rate and kinetic power of the outflow detected in NGC 0708 to those of other observed outflows to ascertain if they are similar.

The first AGN-driven molecular gas outflow found in a non-interacting galaxy was in the early-type galaxy NGC 1266 (Alatalo et al., 2011), with an outflow mass of $\approx 2.4 \times 10^7$ M$_\odot$ and a mass outflow rate of ≈ 13 M$_\odot$ yr^{-1}. Alatalo et al. (2011) also found an AGN jet to be the only viable source of energy for the outflow (with a jet kinetic power of $\approx 6.1 \times 10^{42}$ erg s^{-1}), requiring a coupling factor of ≈ 2 percent. The outflow in NGC 1266 is multiphase (Davis et al. 2012) and is seen in both red- and blue-shifted molecular emission. It has an average radial extent of ≈ 460 pc (Alatalo et al., 2015), the larger size indicating the outflow is perhaps older than that in NGC 0708. The similarity of the coupling factors between the jet and ISM indicates this may be standard for jet-ISM interactions. With new observations of the outflow using dense gas tracers, Alatalo et al. (2015) noted the original assumption of optically-thin gas was incorrect. They thus recalculated the outflow mass and mass outflow rate using a more appropriate $\alpha_{\rm CO}$ (that for ULIRGs), and obtained a mass of 2×10^8 M$_\odot$ and a mass outflow rate of ≈ 110 M$_\odot$ yr^{-1}. This much larger mass outflow rate, especially when compared to that of NGC 0708, shows how comparable jet powers can yield differing mass outflow rates, probably depending on the age of the jet and the geometry of the ISM.

In the far-infrared excess galaxy NGC 1377, Aalto et al. (2012) also identified a molecular outflow in both blue- and red-shifted gas, of total molecular gas mass $> 1 \times 10^7$ M$_\odot$, much larger than that of NGC 0708 (but less than that in NGC 1266). NGC 1377 has a mass outflow rate > 8 M$_\odot$ yr^{-1}, larger than even the upper limit (assuming $\alpha_{\rm CO,\,galactic}$) of NGC 0708, whilst the outflow speed is smaller ($V_{\rm out} = 140$ km s^{-1} for NGC 1377 compared to $V_{\rm ave} = 300$ km s^{-1} for NGC 0708). Aalto et al. (2012) concluded the outflow is young and that it is most likely boosted by radiation pressure from the nucleus.

Morganti et al. (2015) found a molecular outflow in the Seyfert 2 galaxy IC 5063, deriving a mass outflow rate of 12 to 30 $M_{\odot}\,yr^{-1}$, larger than the upper limit in NGC 0708 of $\approx 5\,M_{\odot}\,yr^{-1}$ (assuming $\alpha_{\rm CO,\,galactic}$). The kinematic major-axis PVD of IC 5063 looks very similar to that of NGC 0708 (Fig. 5.3), although it shows both red- and blue-shifted gas whereas I can only discern blue-shifted gas. This may be due to a different viewing angle in NGC 0708.

Another offset, asymmetric outflow was found by Fernández-Ontiveros et al. (2020) in the Seyfert 2 galaxy ESO 420-G13. They derived a mass outflow rate of 14 $M_{\odot}\,yr^{-1}$ and a kinetic power of 1.1×10^{41} erg s^{-1}. The kinetic power and geometry of the outflow, 440 pc from the centre, are again consistent with a jet, requiring a coupling factor of $\approx$ 2.7 percent. The mass outflow rate and kinetic power are slightly larger than the upper limits I find in NGC 0708, probably due to ESO 420-G13 having a much more spatially-extended outflow. The asymmetric offset outflowing funnel in ESO 420-G13 illustrates that jet-driven outflows can have such morphologies, depending on the jet-cloud configuration. The close agreement between the morphology, mass outflow rate and kinetic power of ESO 420-G13 and NGC 0708 suggests they have similar configurations.

Given the abundance of detected jet-powered molecular outflows, simulations of such systems have also been conducted and can provide additional insights. Wagner & Bicknell (2011) performed a suite of simulations of jet-ISM interaction in galaxies, finding that jets with powers from 10^{43} to 10^{46} erg s^{-1} can disrupt star formation by dispersing the dense gas in the galaxy core. The large-scale 330 MHz jet in NGC 0708 has a kinetic power ($Q_{\rm jet} \sim 10^{43}$ erg s^{-1}) within the Wagner & Bicknell (2011) range for powering an outflow that disrupts the ISM.

Mukherjee et al. (2018) performed two simulations of the IC 5063 jet-ISM interaction, with jet powers of 10^{44} and 10^{45} erg s^{-1}, respectively. The minimum power of 10^{44} erg s^{-1} is required to reproduce the observed velocity dispersion of ≈ 400 km s^{-1} in an IC 5063-like ISM, while the larger power results in a larger velocity dispersion in a shorter time. Mukherjee et al. (2018) also found that a clumpy, inhomogeneous ISM is able to reproduce the asymmetric and jagged PVD of IC 5063. The similar PVD of NGC 0708 may therefore indicate a clumpy gas distribution (seen in the left panel of Fig. 5.2).

5.4.3 COMPARISON WITH ULIRG OUTFLOWS

The number of molecular outflows in galaxies similar to NGC 0708 is small, but there is a large number of well-studied outflows in ULIRGs. Here I compare to the compilation of Cicone et al. (2014) to place NGC 0708 in the wider picture of outflows, and further the above discussion of power sources. In their discussion, they investigated the relations between mass outflow rate, SFR and AGN luminosity, and compared the gas depletion timescales, kinetic powers and momentum rates of the outflows of nineteen galaxies. Their sample includes seven new observations of local ULIRGs and twelve from the literature. Within these twelve are five that are 'starburst dominated' (with spectra dominated by H II regions) and do not follow the same correlations as those of the other ULIRGs. In the following I will therefore refer to starbursts and ULIRGs as the two populations in the Cicone et al. (2014) analysis.

In the rest of this section I will also follow the Cicone et al. (2014) analysis but add NGC 0708 to the comparison. As shown in Table 5.1, I have calculated its outflow properties using the Cicone et al. (2014) equations, assuming that the outflowing gas uniformly fills the spherical or multi-conical region affected by the outflow and that $\alpha_{\rm CO} = \alpha_{\rm CO,\,ULIRG} = 0.8\,{\rm M}_\odot\,({\rm K~km\,s^{-1}})^{-1}\,{\rm pc}^{-2}$. Although these assumptions are different from those of my preferred case (discussed above), they allow us to compare the observations presented in this chapter directly with those of Cicone et al. (2014).

Relation between mass outflow rate, SFR and AGN luminosity

Cicone et al. (2014) find that starbursts have SFRs roughly equal to their mass outflow rates, indicating that supernova-driven winds are the power source of those outflows. In contrast, ULIRGs have mass outflow rates higher than their SFRs, indicating they need more energy than that supplied by supernovae to power their outflows. NGC 0708 also has a mass outflow rate higher than its star formation rate ($\dot{M}_{\rm OF,\,Cicone,\,ULIRG} \approx 2\,{\rm M}_\odot\,{\rm yr}^{-1}$ versus SFR $< 0.15\,{\rm M}_\odot\,{\rm yr}^{-1}$, where the SFR is from Davis et al. 2016), again pointing to something other than supernovae as the origin of the outflow.

The mass loading factor of a galaxy ($\dot{M}$/SFR) quantifies which process is using most gas within a galaxy, and therefore how star forming or quenching a galaxy is evolving to be. Cicone et al. (2014) found a tentative positive correlation between the mass loading factors and AGN fractions ($L_{\rm AGN}/L_{\rm Bol}$, where $L_{\rm AGN}$ is the AGN bolometric luminosity and $L_{\rm Bol}$ is the total bolometric luminosity of the galaxy; see the bottom panel of Fig. 8 in Cicone et al. 2014). This suggests that the mass outflow rate can be augmented by the presence of an AGN.

This conclusion that an AGN can augment the mass outflow rate is further supported by the correlation Cicone et al. (2014) found between the mass outflow rates and AGN luminosities. I show this relation in the top panel of Fig. 5.7, where the black dashed line is Equation 2 of Cicone et al. (2014), their starburst and ULRIG samples are shown as respectively cyan stars and blue diamonds, and NGC0708 indicated as a magenta pentagon with error bar (I assume the AGN kinetic power estimate, $L_{\mathrm{kin,AGN}}$, from Clarke et al. 2009 is L_{AGN} for NGC 0708). NGC 0708, along with two ULIRGs, is slightly below this relation; it has a slightly low mass outflow rate for its AGN luminosity. This may be indicative of a larger population, whereby this relation is an upper limit.

Gas depletion timescales

The gas depletion time of an outflow ($\tau_{\mathrm{dep,OF}} \equiv M_{\mathrm{tot}}/\dot{M}_{\mathrm{OF}}$) is the time taken for the outflow to deplete the entire gas reservoir of its host galaxy, assuming the outflow continues at its current rate. When considered as a function of AGN luminosity, Cicone et al. (2014) identified a negative correlation, whereby shorter depletion timescales are present in galaxies with higher AGN luminosities. I show this relation in the bottom panel of Fig. 5.7. NGC 0708 follows this trend, with a depletion timescale similar to the average for its AGN luminosity, i.e. tens of millions of years.

Outflow kinetic powers

In Section 5.4.1 I compared the kinetic power of the NGC 0708 outflow to various potential power sources, to ascertain which ones were physically possible. I now further this discussion by considering how the inferred coupling factors compare to theoretical predictions, as in Cicone et al. (2014). Theoretical models and cosmological simulations predict a coupling efficiency of ≈ 5 percent between an AGN luminosity-driven outflow and the AGN power (measured by the AGN bolometric luminosity, L_{AGN}), for AGN accretion close to the Eddington limit (dashed line in Fig. 5.8). NGC 0708 requires a coupling factor of 0.84 percent, indicating sub-Eddington accretion. As can be seen from Fig. 5.8, this is consistent with low-luminosity AGN ULIRGs. Cicone et al. (2014) also noted that for some of their low-luminosity AGNs, previous papers suggested the radio jet as the power source rather than an AGN-driven wind. This agrees with my finding in NGC 0708. As expected, Cicone et al. (2014) found the starburst galaxies to be above the 5 percent limit, indicating their outflows are powered not by the AGN but by a different energy source, most likely supernova ejecta and radiation pressure from young stars. The outflow powers of starburst galaxies are consistent with supernova-driven winds and coupling efficiencies of a few percent to a few tens of percent (Cicone et al., 2014).

Outflow momentum rates

I can also use the momentum rate of an outflow to constrain its origin. Models of AGN wind-driven outflows predict momentum rates of $\approx 20 L_{\mathrm{AGN}}/c$, where c is the speed of

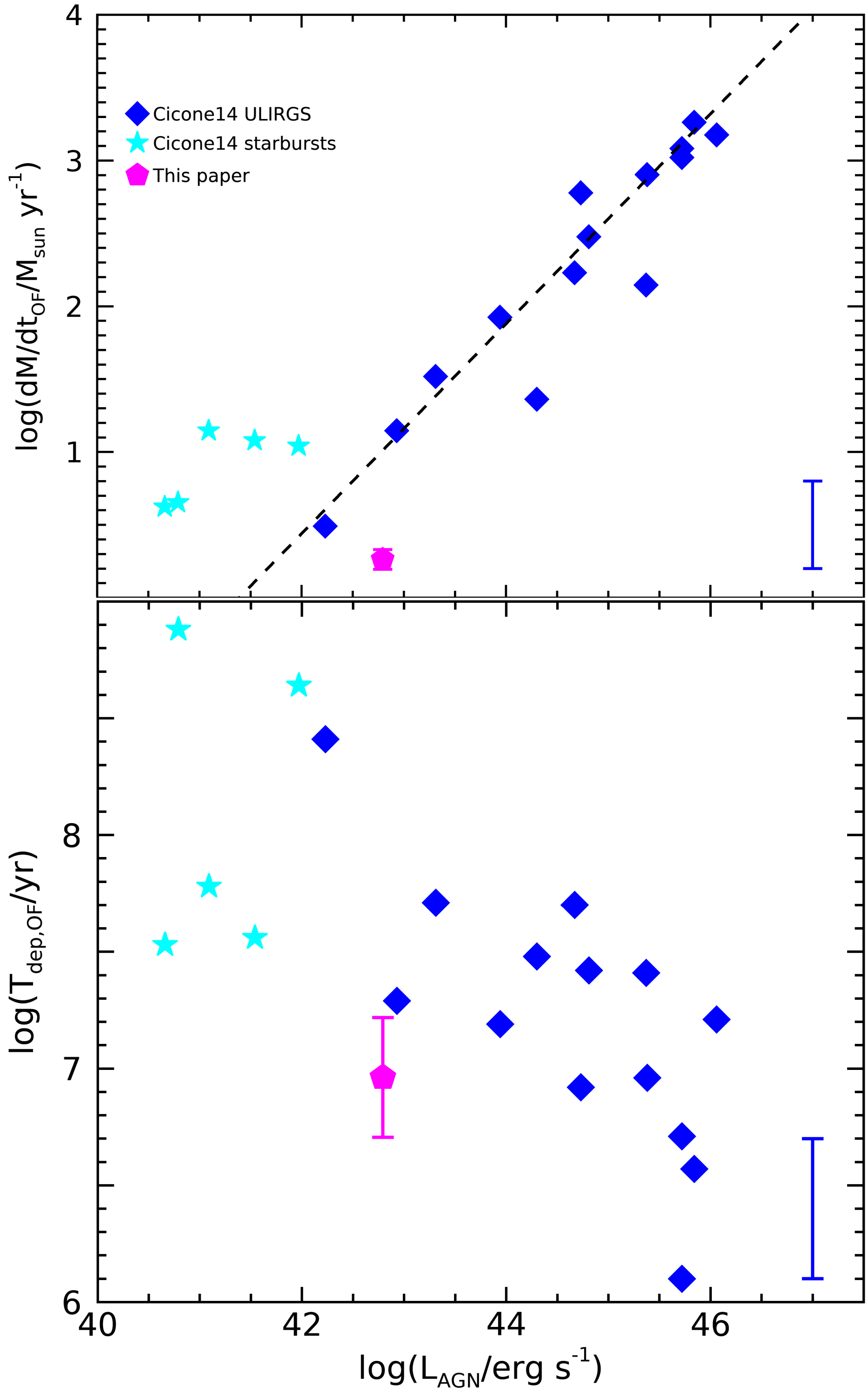

Figure 5.7. *Top panel:* Mass outflow rate as a function of AGN luminosity for the Cicone et al. (2014) ULIRGs (blue diamonds) and starbursts (cyan stars). NGC 0708 is indicated with the magenta pentagon with error bar. The black dashed line is the correlation found by Cicone et al. (2014, their equation 2). *Bottom panel:* Outflow depletion time as a function of AGN luminosity. Symbols are as in the top panel. A representative error bar for the whole Cicone et al. (2014) sample is shown in the bottom-right corner of each panel.

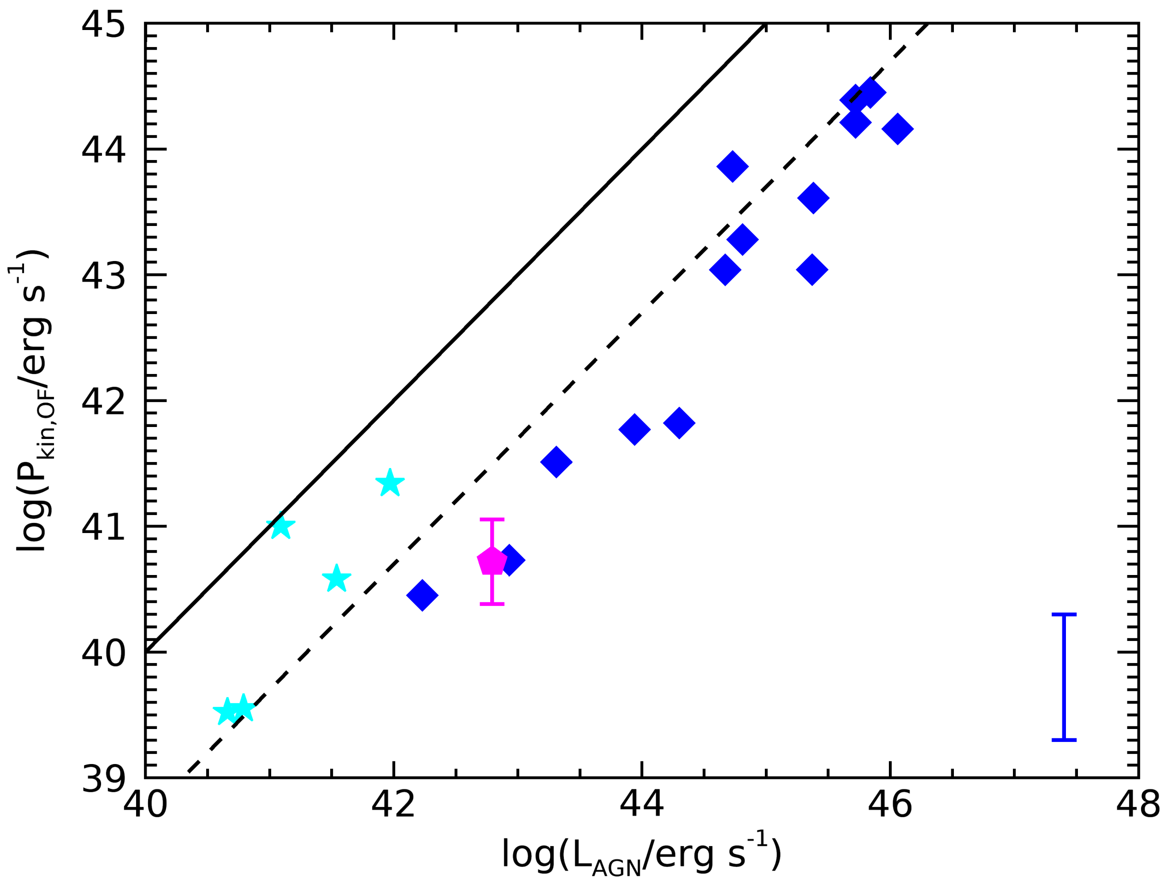

Figure 5.8. Outflow kinetic power as a function of AGN luminosity. Symbols are as in Fig. 5.7. The black solid line shows $P_{\mathrm{kin,\,OF}}/L_{\mathrm{kin,\,AGN}} = 1$ and the black dashed line $P_{\mathrm{kin,\,OF}}/L_{\mathrm{kin,\,AGN}} = 0.05$.

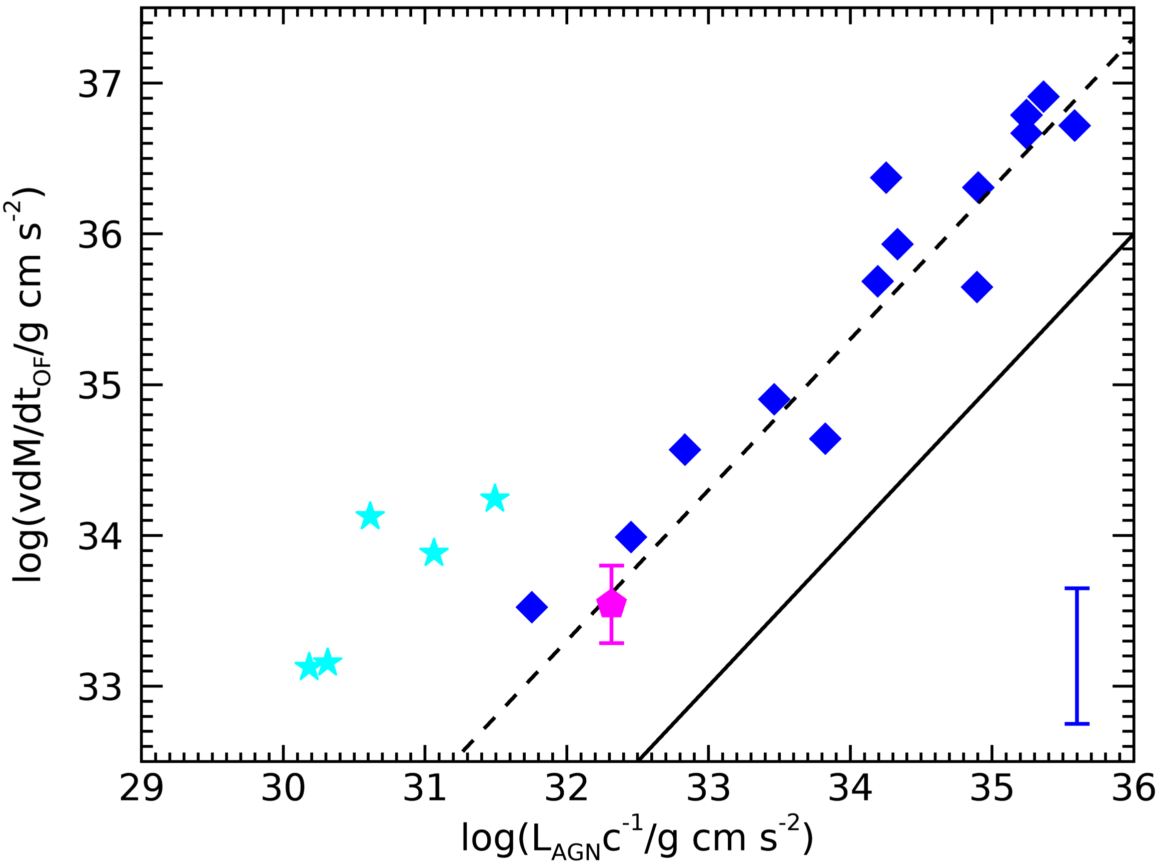

Figure 5.9. Outflow momentum rate ($V_{\rm ave,OF}\dot{M}_{\rm OF}$) as a function of AGN wind momentum rate ($L_{\rm AGN}/c$). Symbols are as in Fig. 5.7. The black solid line shows the one-to-one relation and the black dashed line a ratio of 20.

light. As above the momentum rate of an outflow can be estimated by $\dot{p}_{\rm OF} = V_{\rm ave}\dot{M}_{\rm OF}$. Cicone et al. (2014) found that the ratio between the outflow and AGN wind momentum rate ranges from ≈ 10 to ≈ 50 in the ULIRGs they studied, with most AGN-dominated galaxies consistent within the uncertainties with a ratio ≈ 20 (see Fig. 5.9). This supports the hypothesis that the ISM is impacted by a shock wave arising from a fast and highly ionised wind from the nuclear region. Our work finds the momentum rate ratio in NGC 0708 to be ≈ 17, consistent with those found by Cicone et al. (2014) and again indicating that the AGN wind has sufficient momentum to drive the outflow. However, as previously stated, the geometry of NGC 0708 does not support this mechanism, similarly to the outflow in ESO 420 G13 (Fernández-Ontiveros et al., 2020). This momentum rate calculation also assumes the outflowing clouds uniformly populate a spherical region affected by the outflow. The momentum rate of the outflow would be reduced if the geometry of the system were different.

The outflow of NGC 0708 is likely to be important for its evolution. The depletion time we estimate ($\tau_{\rm dep,OF} \approx 20\,{\rm Myr}$) is approximately equal to the AGN outburst repetition timescale ($\tau_{\rm rep} \geq 28\,$Myr; Clarke et al. 2009), indicating that a single AGN episode (and outflow) has the potential to quench at least the centre NGC 0708 (provided little/no inflow). However, Stewart et al. (1984) calculated that the cooling flow in the ICM of Abell 262 brings in $\approx 28\,{\rm M_\odot\,yr^{-1}}$ of cool gas, so the maximum mass outflow rate ($\dot{M}_{\rm OF,\,thin\,shell,\,galactic}$) found in this work is only $\lessapprox 17$ percent the cooling flow and would not offset it.

5.5 CONCLUSIONS

In this work I have presented ^{12}CO(2–1) line-imaging observations, along with 236 and 5 GHz continuum imaging, of the early-type NGC 0708, the BCG in the galaxy cluster Abell 262. The data show a blue-shifted feature of total molecular gas mass $(2.25\pm0.01)\times 10^5\,{\rm M_\odot}$ calculated assuming a CO-to-H_2 conversion factor $\alpha_{\rm CO} = 0.8\,{\rm M_\odot}\,({\rm K\ km\,s^{-1}})^{-1}\,{\rm pc^{-2}}$ and a CO(2–1)/CO(1–0) line ratio of 0.25. I have discussed the options for this anomalous emission, concluding it could be either cooling flow precipitation and inflow or a jet powered outflow. To aide this I made comparisons between the observations made here and previously observed phenomena, again concluding it agrees well with both options. A jet-driven scenario is also consistent with the observed episodic nature of the AGN in NGC 0708, suggesting if this is the case then the outflow I am currently observing is young. Future work to conclusively decide could include probing shock tracers in NGC 0708, to verify if a jet is impacting the gas, and if so at what location. It would also be helpful to map the ionised gas (e.g. with integral field unit spectroscopy), to see if it is also being impacted and removed from the galaxy centre.

Overall the molecular gas data presented here is evidence for small-scale regulation of the gas reservoir in NGC 0708 by the AGN. Coupled with previous evidence of large-scale disruption of cooling flows, this jet-driven feedback in NGC 0708 thus adds to the arguments suggesting that mechanical feedback is paramount to galaxy evolution.

NGC 0708 is now the second known case of a cluster/BCG with evidence of two different spatial scales of AGN feedback, suggesting that AGN in BCGs are important to regulate their properties on a range of scales. Higher angular resolution ALMA observations will be crucial to probe this process in greater detail, and to allow us to understand fully AGN fuelling and feedback cycles in these extreme sources.

CHAPTER 6
CONCLUSION

I was asked to act when I couldn't act. I was asked to sing 'Funny Face' when I couldn't sing, and dance with Fred Astaire when I couldn't dance - and do all kinds of things I wasn't prepared for.
Then I tried like mad to cope with it.

Audrey Hepburn

From nebulous clouds, to islands of stars and now dynamic objects galaxy's have gone from apparently static to evolving. The different morphologies, and in particular their colours appear to suggest an evolutionary path. Our understanding is growing as we observe galaxies at different stages of their evolution and can then simulate the physics that transforms them. The realisation that supermassive black holes (SMBHs) play a role in galaxy evolution, whilst still being understood, is one of the major advancements of galaxy evolution in the last few decades.

Agreement between simulations and observations requires AGN feedback, which implies a co-evolution between the AGN power source and their host-galaxies. Further to this the relations observed between SMBH and their host-galaxy are reasonably tight, indicating they do grow and evolve together. This thesis focuses on how interferometric observations of molecular gas are helping shed light on this co-evolution. As part of the WISDOM project this work showcases extragalactic molecular gas observations as dynamically cold tracers of a galaxy's gravitational potential and therefore it's internal kinematics.

6.1 KEY RESULT 1: HIGH RESOLUTION ALMA MOLECULAR GAS OBSERVATIONS GIVE EXCEPTIONAL ACCESS TO THE PROCESSES IN THE CENTRES OF GALAXIES, INCLUDING SMBH MASS MEASUREMENTS

The era of ALMA and other (sub)-millimetre interferometers with long baselines has opened up molecular gas as a high-resolution probe of galaxy evolution, and with the added bonus of kinematics the processing of gas by galaxies can be observed. The WISDOM project has been exploiting this, in particular to measure SMBH masses and more recently to resolve individual giant molecular clouds (GMCs) and then investigate their internal kinematics. We (the WISDOM project) have also begun looking at the distribution and morphology of molecular gas near the centres of galaxies, for instance finding holes in the detected ^{12}CO emission around the SMBH positions.

The molecular gas method for measuring SMBH masses, mainly developed by the WISDOM project, has great potential for expanding the SMBH mass sample beyond nearby, bright ETGs and to high redshifts, as shown by the figure of merit (FOM; Chapter 2 and Davis 2014). Exploiting its full potential requires good target selection and analysis. To aid in this in Chapter 4 I have made use of a galaxy simulated by Torrey et al. (2017) which has a known SMBH mass, circular velocity and surface brightness profile. With the aim of advising future observational campaigns and following from the figure of merit (Chapter 2 and Davis 2014) I made mock observations with varying inclination, beam size, channel width and signal to noise ratio. I also varied the way the surface brightness profile was modelled to ascertain if a smoother, less realistic profile badly affected the SMBH mass recovered. The analysis of the mock data cubes followed the usual WISDOM procedure.

It was found that inclinations between $\approx 40-80^{\circ}$ are most favourable for accurate SMBH mass recovery, with small uncertainties. Below this limit the component of the rotational velocity into the line of sight is small, meaning the modelling doesn't have enough information to constrain the SMBH mass. In this regime fixing other parameters can aide the fitting, e.g. Smith et al. (2019) fixed the inclination using ellipse fitting to *HST* imaging of the dust disc. For very high inclinations ($> 80^{\circ}$) the surface brightness modelling can struggle from a lack of information, increasing the uncertainties.

The beam size variations I modelled in this thesis agreed with the findings of Davis (2014) that resolving at least $2R_{\mathrm{SOI}}$ is required for a robust SMBH measurement and a large increase in the uncertainties is seen when the beam size is greater than R_{SOI} and again at $2R_{\mathrm{SOI}}$.

I found that when making observations a channel width of $\leq 20\,\mathrm{km\,s^{-1}}$ or at least

5 channels across the line width is required. This gives information about the gas velocity both closest to the SMBH and in the stellar dominated potential so they can be compared to infer the SMBH influence. This agrees with the figure of merit predictions that I made in Chapter 2 using typical values for molecular gas observations.

The investigation agreed with typical standards for observations, where SNR≥ 3 is required for a robust measurement. For SNR less than this the uncertainties become very large (approximately an order of magnitude) and the MCMC often doesn't converge.

We (the WISDOM project) used these findings as the basis for the selection criteria used in observational campaigns for targets for SMBH mass measurements. Having investigated SMBH recovery and developed modelling tools we (the WISDOM project) are able to select are more diverse set of targets, for instance dwarf galaxies and flocculent LTGs.

6.2 KEY RESULT 2: ACCURATE SMBH MASS MEASUREMENTS ACROSS THE $M_{\mathrm{BH}} - \sigma_{*}$ RELATION

The figure of merit (Chapter 2 and Davis 2014) also concludes that the molecular gas method can, in principle, be used to measure the SMBH mass of $M_{\mathrm{BH}} \gtrapprox 4 \times 10^{8}\ \mathrm{M}_{\odot}$ at any redshift (with inclination $> 30^{\circ}$). This conclusion has yet to be tested, however recent SMBH mass measurements have pushed both to resolve gas very close to the SMBH and to lower black hole masses.

In Chapter 3 I present high resolution ALMA observations (synthesised beam size $58 \times 38\ \mathrm{pc}^{2}$ or $0\farcs18 \times 0\farcs1$) of the molecular gas disc in NGC 0383. The observations reveal gas in Keplerian rotation around the central SMBH, well resolving the sphere of influence (R_{SOI}). By forward modelling the data cube a SMBH mass of $(4.2 \pm 0.7) \times 10^{9}\ \mathrm{M}_{\odot}$ was measured, consistent with $M_{\mathrm{BH}} - \sigma_{*}$ relation predictions. This is the highest SMBH mass measurement by the molecular gas method to date. The high spatial resolution, combined with a spectral resolution of $10\ \mathrm{km\ s^{-1}}$, allowed me to resolve gas very close to the SMBH ($\approx 140\,000$ Schwarzschild radii) showcasing the power of the molecular gas method. Maser observations (currently the most accurate extragalactic SMBH mass measurement method) probe similarly close to the SMBH, up to $\approx 5 \times 10^{4}$ Schwarzschild radii, indicating molecular gas can probe material on the same scale. This shows that molecular gas data can achieve similar accuracy to maser observations, also that the molecular disc in NGC 0383 extends unbroken down to very close to the SMBH.

The publications I have been involved with as part of the WISDOM project have expanded the SMBH mass sample. Fig. 6.1 (reproduced from Davis et al. 2020) shows the $M_{\mathrm{BH}} - \sigma_{*}$ and $M_{\mathrm{BH}} - M_{\mathrm{bulge}}$ relation from McConnell & Ma (2013, black dashed line) and grey points from the compilation of van den Bosch (2016). Overplotted are the SMBH masses measured by the molecular gas method, including my measurement for NGC 0383 (Chapter 3 and North et al. 2019; Davis et al. 2013b; Onishi et al. 2015; Barth et al. 2016a,b; Davis et al. 2017; Onishi et al. 2017; Davis et al. 2018; Boizelle et al. 2019; Combes et al. 2019; Nagai et al. 2019; Smith et al. 2019; Nguyen et al. 2019; Davis et al. 2020). This highlights how the molecular gas method is pushing to much lower velocity dispersions and bulge masses than previous methods. This expansion of the parameter space to lower mass galaxies is important for learning how SMBHs and host galaxies co-evolve for different morphological types of galaxy and those who are not currently in an AGN phase. In particular the measurement of intermediate mass black holes (IMBH) in dwarf galaxies may aid in the understanding of how SMBHs are formed in the first place (Davis et al. 2020). In this paper we (the authors) were also able to compare the molecular gas method to SMBH masses from stellar kinematics and gaseous tracers (see references in Davis et al. 2020) and found a disagreement. Reanalysis of the stellar kinematics to include the non-negligible contribution of the molecular gas to the gravitational potential bought about agreement between the two methods. This highlights the importance of molecular gas and how comparison between methods can verify each.

The best-fitting relations plotted for the $M_{\mathrm{BH}} - M_{\mathrm{bulge}}$ relation again point to a differing relation between SMBH and host for low mass galaxies, compared to higher mass ETGs. Whereas $M_{\mathrm{BH}} - \sigma_*$ appears to hold even for the IMBHs.

The impact of the molecular gas method and WISDOM project on the research into SMBH-galaxy co-evolution is subtle but now the sample is reaching a statistically significant size I can begin to compare it to the existing data. The top panel of Figure 6.1 shows that the molecular gas data (coloured points) overlaps well with the van den Bosch (2016) sample. I fitted a $M_{\mathrm{BH}} - \sigma_*$ relation to the 22 molecular gas measured SMBH to ascertain if it significantly different from other samples, in particular the van den Bosch (2016) sample of 230 SMBH. A simple linear regression fit to the whole sample leads to

$$\log\left(\frac{M_{\mathrm{BH}}}{\mathrm{M}_\odot}\right) = 8.320.51 + 4.08 \pm 0.35 \log\left(\frac{\sigma_*}{200\,\mathrm{km\,s^{-1}}}\right). \tag{6.1}$$

This new fit has a steeper slope than previous fits and does not agree with the van den Bosch (2016) slope of 5.35 ± 0.23. The change in slope follows the IMBHs, 3 of which are above but within the scatter of the van den Bosch (2016) relation. The constants of the relationships are consistent. The variance of the molecular gas SMBH sample around the $M_{\mathrm{BH}} - \sigma_*$ relation is 0.25 dex, smaller than that found by van den Bosch (2016, 0.49) but probably due to sample size.

As I state in future work (Section 6.4) exploiting the molecular gas method to expand the sample beyond the current morphological and size biases of SMBH mass measurements is important for a better understand of the co-evolution of SMBH and host galaxy. The number of groups working with this method is a testament to its ease of use, and the above analysis shows its importance. Differences in the relations with size and morphology are already seen, however a larger sample is needed to fully explore the causality.

6.3 KEY RESULT 3: MOLECULAR GAS OBSERVATIONS ALSO REVEAL THE ROLE OF SMBH AND AGN IN GALAXY EVOLUTION

The role of AGN in galaxy evolution and morphological transformation was mostly inferred from the addition of AGN feedback into galaxy evolution simulations to make them consistent with observations. Observational evidence for this has begun to appear, with the new era of ALMA and other interferometers with long baselines giving the molecular gas perspective in high resolution.

Radio continuum had already revealed large scale AGN jets, and with X-ray data had shown their impact on the hot gas halos of galaxies and clusters. The new high resolution radio data is probing closer to the SMBH and into the interstellar medium of nearby galaxies. These observations have revealed gas flows in the early-type galaxies NGC 0383 (Chapter 3 and North et al. 2019) and NGC 0524 (Smith et al. 2019), and SMBH accretion in the brightest cluster galaxy in Abell 2597 (Tremblay et al. 2016).

In NGC 0708, the BCG in the galaxy cluster Abell 262 high resolution (synthesised beam size $0\farcs088\times0\farcs083$ or $25 \times 23\,\mathrm{pc}^2$) ALMA observations were made. These observations revealed a blue-shifted feature close ($0\farcs4$) to the central AGN, not compatible with rotation. By discussion of the geometry I discuss whether this is caused by cooling flow precipitation or outflowing gas. I calculate the mass $(2.25 \pm 0.01) \times 10^5\,\mathrm{M}_\odot$ assuming a CO-to-H$_2$ conversion factor $\alpha_{\mathrm{CO}} = 0.8\,\mathrm{M}_\odot\,(\mathrm{K\ km\,s^{-1}})^{-1}\,\mathrm{pc}^{-2}$ and a CO(2–1)/CO(1–0) line ratio of 0.25. I further quantitatively compare the properties of the emission with other cooling flow inflows and jet powered outflows, concluding the both explanations agree well with the observations. As discussed below more observations are required for conclusive evidence on what causes the blue-shifted feature.

This is evidence of small-scale gas regulation by an AGN and is complimentary to the large-scale feedback seen in the intra-cluster medium (ICM) around NGC 0708. As a cooling flow cluster it is important to understand how the cooling gas is stalled or stopped from cooling onto NGC 0708, which would make it more star forming than it is observed

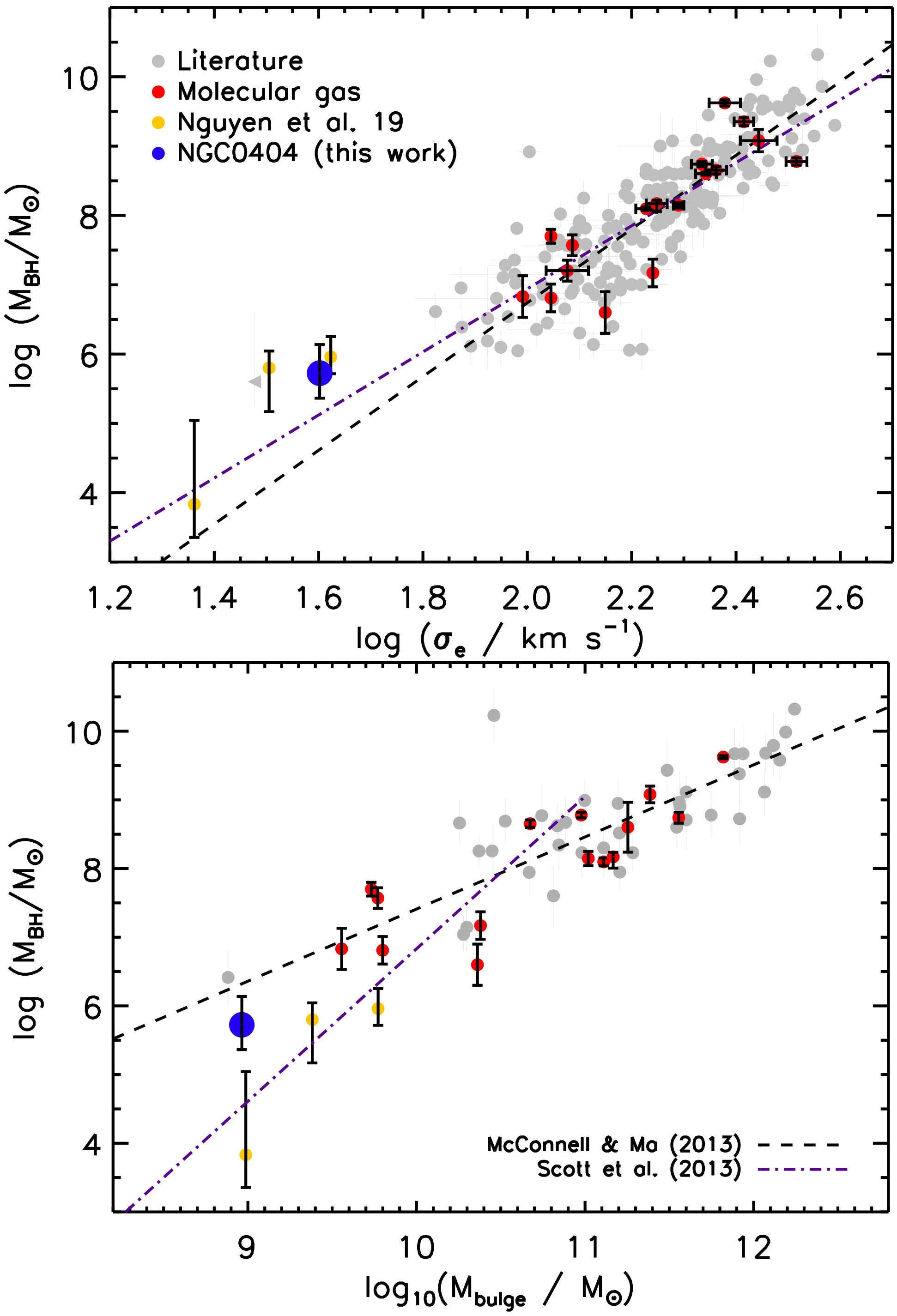

Figure 6.1. Reproduced with permission from Davis et al. 2020: *Top panel:* The $M_{\rm BH}-\sigma_*$ relation (grey points and black dashed line) from the compilation of van den Bosch (2016). The intermediate-mass black hole measured in NGC 0404 by Davis et al. (2020) is the large blue point. Red points are SMBH mass measurements made using the molecular gas method (Davis et al. 2013b; Onishi et al. 2015; Barth et al. 2016a,b; Davis et al. 2017; Onishi et al. 2017; Davis et al. 2018; Boizelle et al. 2019; Combes et al. 2019; Nagai et al. 2019; North et al. 2019; Smith et al. 2019) and in yellow are the SMBHs in low mass galaxies measured in Nguyen et al. (2019). The relation for all galaxies from Greene et al. (2019) is shown as the purple dot-dashed line. *Bottom panel:* $M_{\rm BH}-M_{\rm bulge}$ relations McConnell & Ma (2013, black dashed line) and Scott et al. (2013, purple dot-dahsed line). Coloured points same a left panel.

to be. The detection of an outflow makes NGC 0708 the second known galaxy with both small- and large-scale AGN feedback. Observing this small-scale feedback is important in understanding how gas is regulated in the centres of galaxies which determines their star formation and AGN potential.

New large radio interferometers have begun the era of high resolution extragalactic molecular gas observations which has given us important pieces of evidence for the mechanisms behind galaxy evolution.

6.4 EXPANDING THE WISDOM: ON GOING PROJECTS AND FUTURE WORK

This thesis is the product of work conducted as part of the WISDOM project, the future extensions of it are therefore mostly linked to current plans for the project but also the field of galaxy evolution as a whole.

6.4.1 MATCHING MASER SMBH MASS ACCURACY

In Chapter 3 I presented arguments that the spatial and spectral resolution achieved in NGC 0383 allowed me to resolve gas $\approx 140\,000$ Schwarzschild radii from the SMBH and thus probes the same material as megamasers do. The molecular gas observations did not use the longest baselines available with ALMA. I was involved in a proposal to asses the highest resolution that can be obtained and therefore push to resolving gas closer to the SMBH. This will give even better data to measure the SMBH mass from and give insight into the nature of gas close to the SMBH, and possibly help the explanation of why some galaxies have a hole in their molecular gas (see Chapter 2 for a discussion on the issues around central molecular holes).

6.4.2 FURTHER INVESTIGATION OF THE OUTFLOW IN NGC 0708

As mentioned in Chapter 5, to establish the full extent of the outflow in NGC 0708 the other phases of gas need to be observed. In particular Multi Unit Spectroscopic Explorer (MUSE) or similar observations of the ionised gas would determine if that too was outflowing. Ionised gas observations can also reveal shocked gas and hence where the jet is directly impacting the gas. This would verify the jet-powered outflow claim of Chapter 5. MUSE observations could also spatially resolve the star formation and therefore investigate whether it is being affected by the gas kinematics.

I was involved in a successful Spectromètre Imageur à Transformée de Fourier pour l'Etude en Long et en Large de raies d'Emission (SITELLE) proposal this semester to observe Hα emission in 5 nearby galaxies, including NGC 0708. This will allow us to spatially resolve the star formation rate and therefore, in combination with ALMA molecular gas observations, probe the star formation efficiency. These observations will also shed light on the kinematics of the ionised gas in NGC 0708 and whether they are disturbed.

6.4.3 FURTHER EXPANSION OF THE SMBH MASS SAMPLE

The introduction to SMBH mass measurement and the molecular gas method (Section 1.4 and Chapters 2 and 3) described the current issues with the SMBH mass sample which has a bias toward ETGs. It is important that the molecular gas method is used to offset this and expand the sample of LTG SMBH mass measurements. Proposals with this objective have been submitted and data obtained. As shown in Chapter 4, the development of the SKYSAMPLER tool should aide in LTG molecular gas analysis as they often have more flocculent gas distributions. Thus using this tool on the new observations should rapidly expand the sample.

The findings of Chapter 4 will also aide the target selection for future observation campaigns, in particular the recommendations on inclination can be applied to the existing list of potential targets (for the current target list selection see Chapter 2).

6.4.4 EXPANDING THE ETG GMC CATALOGUE

In Chapter 2 I introduced the other research that can be performed with high resolution molecular gas observations, one being investigating giant molecular cloud (GMC) properties. Of the data published in this thesis NGC 0383 has a smooth molecular gas distribution which makes identifying individual GMCs difficult, despite this the data is to be published as part of the GMC study (Liu et al. in prep.). As NGC 0383 is a massive galaxy the deep potential causes large amounts of shear which may be important in driving the GMC kinematics and in destroying them. As mentioned in Chapter 2 the new Virial parameter formalism in Liu et al. 2020, which includes shear, is important for correctly analysing such massive galaxies. The data on NGC 0708 is more flocculant, and slightly spatially and kinematically disturbed. This makes modelling the overall kinematics difficult and may lead to disturbed GMC kinematics. In general expanding this sample is important to ascertain if the local size-linewidth relations hold elsewhere, especially in places where shear is important which haven't been well studied.

6.4.5 DETERMINING α_{CO} IN ETGS

This thesis partially depends on the conversion of ^{12}CO intensity to mass of molecular hydrogen (M_{H_2}), performed using the X_{CO} or α_{CO} conversion factor. The appropriate value to use for each source has long been debated, and to aid this Sandstrom et al. (2013) pioneered a new method to measure X_{CO} in a resolved manner, using dust to independently determine M_{H_2}. To expand on their work I proposed to use resolved *Herschel* observations, with new ^{12}CO ALMA ones (see Chapter 2) to determine X_{CO} in a resolved manner in ETGs. This will shed light on the conditions within ETGs and allow more accurate molecular gas mass measurements, which in turn will aide the accuracy of the SMBH mass measurements and the other kinematic analysis performed on the observations.

To aide in the determination of α_{CO} observations can be made of dense gas tracers or higher-J CO lines which would inform on the density and optical depth of the gas. As these would also aide in the analysis of the outflow in NGC 0708 they, in particular, are a good next step from this thesis.

6.5 FINAL REMARKS

Overall the era of long baseline radio interferometry has started a new understanding in the evolution of galaxies. In this thesis I focus on observations of molecular gas, their use as a dynamically cold tracer of galaxy kinematics and how that informs us of the processes governing a galaxy and its evolution. Molecular gas observations point to the importance of AGN as regulators of gas reservoirs and hence as the control of both star formation and their own fuel for future accretion.

BIBLIOGRAPHY

Aalto S., Muller S., Sakamoto K., Gallagher J. S., Martín S., Costagliola F., 2012, *A&A*, 546, A68

Agertz O., Teyssier R., Moore B., 2009, *MNRAS*, 397, L64

Alatalo K., et al., 2011, *ApJ*, 735, 88

Alatalo K., et al., 2013, *MNRAS*, 432, 1796

Alatalo K., et al., 2015, *ApJ*, 798, 31

Albareti F. D., et al., 2017, *ApJS*, 233, 25

Andernach H., Waldthausen H., Wielebinski R., 1980, A&AS, 41, 339

Andrae R., 2010, arXiv e-prints, p. arXiv:1009.2755

Baldwin J. E., Boysen R. C., Hales S. E. G., Jennings J. E., Waggett P. C., Warner P. J., Wilson D. M. A., 1985, *MNRAS*, 217, 717

Balogh M. L., Christlein D., Zabludoff A. I., Zaritsky D., 2001, *ApJ*, 557, 117

Barth A. J., Boizelle B. D., Darling J., Baker A. J., Buote D. A., Ho L. C., Walsh J. L., 2016a, *ApJ*, 822, L28

Barth A. J., Darling J., Baker A. J., Boizelle B. D., Buote D. A., Ho L. C., Walsh J. L., 2016b, *ApJ*, 823, 51

Bate N. F., Floyd D. J. E., Webster R. L., Wyithe J. S. B., 2011, *ApJ*, 731, 71

Baum W. A., 1959, *PASP*, 71, 106

Beckmann V., Shrader C. R., 2012, Active Galactic Nuclei

Beifiori A., Sarzi M., Corsini E. M., Dalla Bontà E., Pizzella A., Coccato L., Bertola F., 2009, *ApJ*, 692, 856

Beifiori A., Courteau S., Corsini E. M., Zhu Y., 2012, *MNRAS*, 419, 2497

Bekki K., Couch W. J., Shioya Y., 2002, *ApJ*, 577, 651

Bell E. F., McIntosh D. H., Katz N., Weinberg M. D., 2003, *ApJS*, 149, 289

Bell E. F., et al., 2004, *ApJ*, 608, 752

Bennett A. S., 1962, MmRAS, 68, 163

Benson A. J., Bower R. G., Frenk C. S., Lacey C. G., Baugh C. M., Cole S., 2003, *ApJ*, 599, 38

Bîrzan L., Rafferty D. A., McNamara B. R., Wise M. W., Nulsen P. E. J., 2004, *ApJ*, 607, 800

Bîrzan L., Rafferty D. A., Nulsen P. E. J., McNamara B. R., Röttgering H. J. A., Wise M. W., Mittal R., 2012, *MNRAS*, 427, 3468

Blandford R. D., McKee C. F., 1982, *ApJ*, 255, 419

Blanton E. L., Sarazin C. L., McNamara B. R., Clarke T. E., 2004, *ApJ*, 612, 817

Boizelle B. D., Barth A. J., Walsh J. L., Buote D. A., Baker A. J., Darling J., Ho L. C., 2019, *ApJ*, 881, 10

Bolatto A. D., Leroy A. K., Rosolowsky E., Walter F., Blitz L., 2008, *ApJ*, 686, 948

Bolatto A. D., Wolfire M., Leroy A. K., 2013, *ARAA*, 51, 207

Booth C. M., Schaye J., 2009, *MNRAS*, 398, 53

Bower R. G., Benson A. J., Malbon R., Helly J. C., Frenk C. S., Baugh C. M., Cole S., Lacey C. G., 2006, *MNRAS*, 370, 645

Bower R. G., McCarthy I. G., Benson A. J., 2008, *MNRAS*, 390, 1399

Bower R. G., Benson A. J., Crain R. A., 2012, *MNRAS*, 422, 2816

Braatz J., et al., 2015, in IAU General Assembly. p. 2255730

Bridle A. H., Perley R. A., 1984, *ARAA*, 22, 319

Briggs D. S., 1995, in American Astronomical Society Meeting Abstracts. p. 112.02

Bundy K., et al., 2008, *ApJ*, 681, 931

Calzetti D., et al., 2007, *ApJ*, 666, 870

Cappellari M., 2002, *MNRAS*, 333, 400

Cappellari M., 2008, *MNRAS*, 390, 71

Cappellari M., 2016, *ARAA*, 54, 597

Cappellari M., Verolme E. K., van der Marel R. P., Verdoes Kleijn G. A., Illingworth G. D., Franx M., Carollo C. M., de Zeeuw P. T., 2002, *ApJ*, 578, 787

Cappellari M., et al., 2011, *MNRAS*, 413, 813

Cappellari M., et al., 2013, *MNRAS*, 432, 1709

Cicone C., et al., 2014, *A&A*, 562, A21

Clark C. J. R., et al., 2018, *A&A*, 609, A37

Clarke T. E., Blanton E. L., Sarazin C. L., Anderson L. D., Gopal-Krishna Douglass E. M., Kassim N. E., 2009, *ApJ*, 697, 1481

Clemens M. S., et al., 2010, *A&A*, 518, L50

Cole S., Lacey C. G., Baugh C. M., Frenk C. S., 2000, *MNRAS*, 319, 168

Combes F., 2001, in Funes J. G., Corsini E. M., eds, Astronomical Society of the Pacific Conference Series Vol. 230, Galaxy Disks and Disk Galaxies. pp 213–220 (`arXiv:astro-ph/0008341`)

Combes F., et al., 2019, *A&A*, 623, A79

Conselice C. J., 2003, *ApJS*, 147, 1

Courteau S., et al., 2014, Reviews of Modern Physics, 86, 47

Cox D. P., 2005, *ARAA*, 43, 337

Crawford C. S., Allen S. W., Ebeling H., Edge A. C., Fabian A. C., 1999, *MNRAS*, 306, 857

Crocker A. F., Jeong H., Komugi S., Combes F., Bureau M., Young L. M., Yi S., 2009, *MNRAS*, 393, 1255

Croton D. J., et al., 2006, *MNRAS*, 365, 11

Cutri R. M., et al. 2012, VizieR Online Data Catalog, p. II/311

Dame T. M., 2011, preprint (arXiv:1101.1499),

Davé R., Finlator K., Oppenheimer B. D., 2012, *MNRAS*, 421, 98

Davis T. A., 2014, *MNRAS*, 443, 911

Davis T. A., et al., 2011, *MNRAS*, 414, 968

Davis T. A., et al., 2012, *MNRAS*, 426, 1574

Davis T. A., et al., 2013a, *MNRAS*, 429, 534

Davis T. A., Bureau M., Cappellari M., Sarzi M., Blitz L., 2013b, *Nature*, 494, 328

Davis T. A., Greene J., Ma C.-P., Pand ya V., Blakeslee J. P., McConnell N., Thomas J., 2016, *MNRAS*, 455, 214

Davis T. A., Bureau M., Onishi K., Cappellari M., Iguchi S., Sarzi M., 2017, *MNRAS*, 468, 4675

Davis T. A., et al., 2018, *MNRAS*, 473, 3818

Davis T. A., Greene J. E., Ma C.-P., Blakeslee J. P., Dawson J. M., Pandya V., Veale M., Zabel N., 2019, *MNRAS*, 486, 1404

Davis T. A., et al., 2020, arXiv e-prints, p. arXiv:2007.05536

De Lucia G., Blaizot J., 2007, *MNRAS*, 375, 2

Denney K. D., et al., 2010, *ApJ*, 721, 715

Djorgovski S., Davis M., 1987, *ApJ*, 313, 59

Donahue M., Mack J., Voit G. M., Sparks W., Elston R., Maloney P. R., 2000, *ApJ*, 545, 670

Donato D., Sambruna R. M., Gliozzi M., 2004, *ApJ*, 617, 915

Downes D., Solomon P. M., 1998, *ApJ*, 507, 615

Dressler A., 1980, *ApJ*, 236, 351

Dressler A., Richstone D. O., 1988, *ApJ*, 324, 701

Dressler A., Lynden-Bell D., Burstein D., Davies R. L., Faber S. M., Terlevich R., Wegner G., 1987, *ApJ*, 313, 42

Ebneter K., Balick B., 1985, *AJ*, 90, 183

Edge A. C., 2001, *MNRAS*, 328, 762

Edge D. O., Shakeshaft J. R., McAdam W. B., Baldwin J. E., Archer S., 1959, MmRAS, 68, 37

Edge A. C., Stewart G. C., Fabian A. C., 1992, *MNRAS*, 258, 177

Emsellem E., Monnet G., Bacon R., 1994, *A&A*, 285, 723

Faber S. M., Jackson R. E., 1976, *ApJ*, 204, 668

Fabian A. C., 1994, Annual Review of Astronomy and Astrophysics, 32, 277

Fabian A. C., 2012, *ARAA*, 50, 455

Fabian A. C., Nulsen P. E. J., Canizares C. R., 1984, *Nature*, 310, 733

Ferland G. J., Fabian A. C., Johnstone R. M., 1994, *MNRAS*, 266, 399

Fernández-Ontiveros J. A., et al., 2020, *A&A*, 633, A127

Ferrarese L., Merritt D., 2000, *ApJ*, 539, L9

Ferrarese L., Ford H. C., Jaffe W., 1996, *ApJ*, 470, 444

Freedman W. L., et al., 2001, *ApJ*, 553, 47

Freedman W. L., et al., 2019, *ApJ*, 882, 34

Fukui Y., Kawamura A., 2010, *ARAA*, 48, 547

Gao Y., Solomon P. M., 2004, *ApJ*, 606, 271

Gao F., et al., 2017, *ApJ*, 834, 52

Gaspari M., Ruszkowski M., Sharma P., 2012, *ApJ*, 746, 94

Gaspari M., Brighenti F., Ruszkowski M., 2013, Astronomische Nachrichten, 334, 394

Gaspari M., et al., 2018, *ApJ*, 854, 167

Geach J. E., et al., 2014, *Nature*, 516, 68

Gebhardt K., Thomas J., 2009, *ApJ*, 700, 1690

Gebhardt K., et al., 2000, *ApJ*, 539, L13

Ghez A. M., Salim S., Hornstein S. D., Tanner A., Lu J. R., Morris M., Becklin E. E., Duchêne G., 2005, *ApJ*, 620, 744

Graham A. W., Driver S. P., 2007, *ApJ*, 655, 77

Greene J. E., et al., 2010, *ApJ*, 721, 26

Greene J. E., Strader J., Ho L. C., 2019, arXiv e-prints, p. arXiv:1911.09678

Gregory P. C., Scott W. K., Douglas K., Condon J. J., 1996, *ApJS*, 103, 427

Gültekin K., et al., 2009, *ApJ*, 698, 198

Gunn J. E., Gott J. Richard I., 1972, *ApJ*, 176, 1

Hales S. E. G., Baldwin J. E., Warner P. J., 1993, *MNRAS*, 263, 25

Häring N., Rix H.-W., 2004, *ApJ*, 604, L89

Haynes M. P., Giovanelli R., Chincarini G. L., 1984, *ARAA*, 22, 445

Healey S. E., Romani R. W., Taylor G. B., Sadler E. M., Ricci R., Murphy T., Ulvestad J. S., Winn J. N., 2007, *ApJS*, 171, 61

Heckman T. M., Baum S. A., van Breugel W. J. M., McCarthy P., 1989, *ApJ*, 338, 48

Herrnstein J. R., et al., 1999, *Nature*, 400, 539

Heyer M. H., Brunt C. M., 2004, *ApJ*, 615, L45

Hlavacek-Larrondo J., et al., 2015, *ApJ*, 805, 35

Ho L. C., Filippenko A. V., Sargent W. L. W., 1997, *ApJS*, 112, 315

Ho L. C., Filippenko A. V., Sargent W. L. W., 2003, *ApJ*, 583, 159

Hoffer A. S., Donahue M., Hicks A., Barthelemy R. S., 2012, *ApJS*, 199, 23

Högbom J. A., 1969, in Bulletin of the American Astronomical Society. p. 348

Holt J., Tadhunter C., Morganti R., Bellamy M., González Delgado R. M., Tzioumis A., Inskip K. J., 2006, *MNRAS*, 370, 1633

Hopkins P. F., 2015, *MNRAS*, 450, 53

Hopkins P. F., Kereš D., Oñorbe J., Faucher-Giguère C.-A., Quataert E., Murray N., Bullock J. S., 2014, *MNRAS*, 445, 581

Hubble E. P., 1926, *ApJ*, 64, 321

Hubble E., 1929, Proceedings of the National Academy of Science, 15, 168

Hudson M. J., Lucey J. R., Smith R. J., Schlegel D. J., Davies R. L., 2001, *MNRAS*, 327, 265

Imanishi M., Nakanishi K., Izumi T., Wada K., 2018, *ApJ*, 853, L25

Jensen J. B., Tonry J. L., Barris B. J., Thompson R. I., Liu M. C., Rieke M. J., Ajhar E. A., Blakeslee J. P., 2003, *ApJ*, 583, 712

Jiang X.-J., Wang Z., Gu Q., Wang J., Zhang Z.-Y., 2015, *ApJ*, 799, 92

Johnstone R. M., Fabian A. C., Nulsen P. E. J., 1987, *MNRAS*, 224, 75

Jones C., Forman W., 1984, *ApJ*, 276, 38

Jorgensen I., Franx M., Kjaergaard P., 1995, *MNRAS*, 276, 1341

Kauffmann G., White S. D. M., Heckman T. M., Ménard B., Brinchmann J., Charlot S., Tremonti C., Brinkmann J., 2004, *MNRAS*, 353, 713

King A., Pounds K., 2015, *ARAA*, 53, 115

Knapp G. R., Rupen M. P., 1996, *ApJ*, 460, 271

Kodama T., Bower R. G., Bell E. F., 1999, *MNRAS*, 306, 561

Kormendy J., Bender R., 2012, *ApJS*, 198, 2

Kormendy J., Gebhardt K., 2001, in Wheeler J. C., Martel H., eds, American Institute of Physics Conference Series Vol. 586, 20th Texas Symposium on relativistic astrophysics. pp 363–381 (`arXiv:astro-ph/0105230`), doi:10.1063/1.1419581

Kormendy J., Ho L. C., 2013, *ARAA*, 51, 511

Kormendy J., Kennicutt Robert C. J., 2004, *ARAA*, 42, 603

Kormendy J., Richstone D., 1995, *ARAA*, 33, 581

Krajnović D., McDermid R. M., Cappellari M., Davies R. L., 2009, *MNRAS*, 399, 1839

Krajnović D., Cappellari M., McDermid R. M., 2018, *MNRAS*, 473, 5237

Krumholz M. R., Gnedin N. Y., 2011, *ApJ*, 729, 36

Kuo C. Y., et al., 2011, *ApJ*, 727, 20

Lacey C., Cole S., 1993, *MNRAS*, 262, 627

Lacey C., Silk J., 1991, *ApJ*, 381, 14

Laing R. A., Bridle A. H., 2002, *MNRAS*, 336, 1161

Larson R. B., 1981, *MNRAS*, 194, 809

Laurikainen E., Salo H., Buta R., Knapen J. H., Comerón S., 2010, *MNRAS*, 405, 1089

Lees J. F., Knapp G. R., Rupen M. P., Phillips T. G., 1991, *ApJ*, 379, 177

Leitherer C., Ortiz Otálvaro P. A., Bresolin F., Kudritzki R.-P., Lo Faro B., Pauldrach A. W. A., Pettini M., Rix S. A., 2010, *ApJS*, 189, 309

Leroy A. K., et al., 2013, *AJ*, 146, 19

Li C., White S. D. M., 2009, *MNRAS*, 398, 2177

Li Y., Bryan G. L., Ruszkowski M., Voit G. M., O'Shea B. W., Donahue M., 2015, *ApJ*, 811, 73

Lim J., Leon S., Combes F., Dinh-V-Trung 2000, *ApJ*, 545, L93

Lo K. Y., 2005, *ARAA*, 43, 625

Lutz D., et al., 2020, *A&A*, 633, A134

Ma C.-P., Greene J. E., McConnell N., Janish R., Blakeslee J. P., Thomas J., Murphy J. D., 2014, *ApJ*, 795, 158

MacDonald G. H., Kenderdine S., Neville A. C., 1968, *MNRAS*, 138, 259

Madau P., Dickinson M., 2014, *ARAA*, 52, 415

Magorrian J., et al., 1998, *AJ*, 115, 2285

Makarov D., Prugniel P., Terekhova N., Courtois H., Vauglin I., 2014, *A&A*, 570, A13

Marconi A., Hunt L. K., 2003, *ApJ*, 589, L21

Martig M., Bournaud F., Teyssier R., Dekel A., 2009, *ApJ*, 707, 250

Masters K. L., et al., 2019, *MNRAS*, 487, 1808

McCarthy I. G., Babul A., Bower R. G., Balogh M. L., 2008, *MNRAS*, 386, 1309

McConnell N. J., Ma C.-P., 2013, *ApJ*, 764, 184

McKee C. F., Ostriker J. P., 1977, *ApJ*, 218, 148

McMullin J. P., Waters B., Schiebel D., Young W., Golap K., 2007, in Shaw R. A., Hill F., Bell D. J., eds, Astronomical Society of the Pacific Conference Series Vol. 376, Astronomical Data Analysis Software and Systems XVI. p. 127

McNamara B. R., Nulsen P. E. J., 2007, *ARAA*, 45, 117

McNamara B. R., Nulsen P. E. J., 2012, New Journal of Physics, 14, 055023

McNamara B. R., O'Connell R. W., 1989, *AJ*, 98, 2018

McNamara B. R., Nulsen P. E. J., Wise M. W., Rafferty D. A., Carilli C., Sarazin C. L., Blanton E. L., 2005, *Nature*, 433, 45

McNamara B. R., et al., 2014, *ApJ*, 785, 44

McNamara B. R., Russell H. R., Nulsen P. E. J., Hogan M. T., Fabian A. C., Pulido F., Edge A. C., 2016, *ApJ*, 830, 79

Mei S., et al., 2007, *ApJ*, 655, 144

Miyoshi M., Moran J., Herrnstein J., Greenhill L., Nakai N., Diamond P., Inoue M., 1995, *Nature*, 373, 127

Moore B., Katz N., Lake G., Dressler A., Oemler A., 1996, *Nature*, 379, 613

Morganti R., Oosterloo T., Oonk J. B. R., Frieswijk W., Tadhunter C., 2015, *A&A*, 580, A1

Mukherjee D., Wagner A. Y., Bicknell G. V., Morganti R., Oosterloo T., Nesvadba N., Sutherland R. S., 2018, *MNRAS*, 476, 80

Mullaney J. R., et al., 2012, *ApJ*, 753, L30

Nagai H., et al., 2019, *ApJ*, 883, 193

Nakai N., Inoue M., Miyoshi M., 1993, *Nature*, 361, 45

Nesvadba N. P. H., et al., 2010, *A&A*, 521, A65

Nguyen D. D., et al., 2019, *ApJ*, 872, 104

North E. V., et al., 2019, *MNRAS*, 490, 319

O'Sullivan E., Forbes D. A., Ponman T. J., 2001, *MNRAS*, 328, 461

Ocaña Flaquer B., Leon S., Combes F., Lim J., 2010, *A&A*, 518, A9

Oemler Augustus J., 1974, *ApJ*, 194, 1

Okuda T., Kohno K., Iguchi S., Nakanishi K., 2005, *ApJ*, 620, 673

Olivares V., et al., 2019, *A&A*, 631, A22

Onishi K., Iguchi S., Sheth K., Kohno K., 2015, *ApJ*, 806, 39

Onishi K., Iguchi S., Davis T. A., Bureau M., Cappellari M., Sarzi M., Blitz L., 2017, *MNRAS*, 468, 4663

Onken C. A., Ferrarese L., Merritt D., Peterson B. M., Pogge R. W., Vestergaard M., Wandel A., 2004, *ApJ*, 615, 645

Oosterloo T., et al., 2010, *MNRAS*, 409, 500

Pandya V., et al., 2017, *ApJ*, 837, 40

Parma P., de Ruiter H. R., Fanti C., Fanti R., 1986, A&AS, 64, 135

Paulino-Afonso A., et al., 2019, *A&A*, 630, A57

Peterson B. M., 1993, *PASP*, 105, 247

Peterson B. M., 2008, New A Rev., 52, 240

Peterson B. M., Horne K., 2004, Astronomische Nachrichten, 325, 248

Peterson B. M., et al., 2004, *ApJ*, 613, 682

Pfenniger D., Norman C., 1990, *ApJ*, 363, 391

Prasad D., Sharma P., Babul A., 2015, *ApJ*, 811, 108

Rafferty D. A., McNamara B. R., Nulsen P. E. J., Wise M. W., 2006, *ApJ*, 652, 216

Ramakrishnan V., et al., 2019, *MNRAS*, 487, 444

Rees M. J., Ostriker J. P., 1977, *MNRAS*, 179, 541

Regan M. W., Thornley M. D., Helfer T. T., Sheth K., Wong T., Vogel S. N., Blitz L., Bock D. C. J., 2001, *ApJ*, 561, 218

Reid M. J., Braatz J. A., Condon J. J., Greenhill L. J., Henkel C., Lo K. Y., 2009, *ApJ*, 695, 287

Roman-Duval J., Heyer M., Brunt C. M., Clark P., Klessen R., Shetty R., 2016, *ApJ*, 818, 144

Russell H. R., et al., 2014, *ApJ*, 784, 78

Russell H. R., et al., 2016, *MNRAS*, 458, 3134

Russell H. R., et al., 2017a, *MNRAS*, 472, 4024

Russell H. R., et al., 2017b, *ApJ*, 836, 130

Sage L. J., Wrobel J. M., 1989, *ApJ*, 344, 204

Saintonge A., et al., 2011a, *MNRAS*, 415, 32

Saintonge A., et al., 2011b, *MNRAS*, 415, 61

Saintonge A., et al., 2017, *ApJS*, 233, 22

Salomé P., Combes F., 2003, *A&A*, 412, 657

Sandstrom K. M., et al., 2013, *ApJ*, 777, 5

Sarzi M., Rix H.-W., Shields J. C., Rudnick G., Ho L. C., McIntosh D. H., Filippenko A. V., Sargent W. L. W., 2001, *ApJ*, 550, 65

Scharwächter J., McGregor P. J., Dopita M. A., Beck T. L., 2013, *MNRAS*, 429, 2315

Schechter P., 1976, *ApJ*, 203, 297

Schweizer F., Seitzer P., 1992, *AJ*, 104, 1039

Scott N., Graham A. W., Schombert J., 2013, *ApJ*, 768, 76

Scoville N. Z., Sanders D. B., 1987, H_2 in the Galaxy. p. 21, doi:10.1007/978-94-009-3861-8˙2

Shankar F., Weinberg D. H., Miralda-Escudé J., 2009, *ApJ*, 690, 20

Sharma P., McCourt M., Quataert E., Parrish I. J., 2012, *MNRAS*, 420, 3174

Skrutskie M. F., et al., 2006, *AJ*, 131, 1163

Smith M. D., et al., 2019, *MNRAS*, 485, 4359

Solomon P. M., Vanden Bout P. A., 2005, *ARAA*, 43, 677

Solomon P. M., Rivolo A. R., Barrett J., Yahil A., 1987, *ApJ*, 319, 730

Springel V., Hernquist L., 2003, *MNRAS*, 339, 289

Steinmetz M., Navarro J. F., 2002, New A, 7, 155

Stewart G. C., Fabian A. C., Jones C., Forman W., 1984, *ApJ*, 285, 1

Stewart K. R., Kaufmann T., Bullock J. S., Barton E. J., Maller A. H., Diemand J., Wadsley J., 2011, *ApJ*, 738, 39

Strateva I., et al., 2001, *AJ*, 122, 1861

Sun M., 2009, *ApJ*, 704, 1586

Thomas J., Ma C.-P., McConnell N. J., Greene J. E., Blakeslee J. P., Janish R., 2016, *Nature*, 532, 340

Tiley A. L., Bureau M., Saintonge A., Topal S., Davis T. A., Torii K., 2016, *MNRAS*, 461, 3494

Torrey P., Hopkins P. F., Faucher-Giguère C.-A., Vogelsberger M., Quataert E., Kereš D., Murray N., 2017, *MNRAS*, 467, 2301

Tremblay G. R., et al., 2012a, *MNRAS*, 424, 1026

Tremblay G. R., et al., 2012b, *MNRAS*, 424, 1042

Tremblay G. R., et al., 2016, *Nature*, 534, 218

Treu T., Koopmans L. V. E., 2004, *ApJ*, 611, 739

Tully R. B., Fisher J. R., 1977, *A&A*, 500, 105

Utomo D., Blitz L., Davis T., Rosolowsky E., Bureau M., Cappellari M., Sarzi M., 2015, *ApJ*, 803, 16

Vantyghem A. N., et al., 2016, *ApJ*, 832, 148

Vantyghem A. N., et al., 2018, *ApJ*, 863, 193

Veilleux S., Cecil G., Bland-Hawthorn J., 2005, *ARAA*, 43, 769

Volonteri M., Haardt F., Madau P., 2003, *ApJ*, 582, 559

Wagner A. Y., Bicknell G. V., 2011, *ApJ*, 728, 29

Walsh J. L., Barth A. J., Ho L. C., Sarzi M., 2013, *ApJ*, 770, 86

Wegner G., Colless M., Baggley G., Davies R. L., Bertschinger E., Burstein D., McMahan Robert K. J., Saglia R. P., 1996, *ApJS*, 106, 1

Wegner G. A., Corsini E. M., Thomas J., Saglia R. P., Bender R., Pu S. B., 2012, *AJ*, 144, 78

Wenger M., et al., 2000, A&AS, 143, 9

White S. D. M., Frenk C. S., 1991, *ApJ*, 379, 52

White S. D. M., Rees M. J., 1978, *MNRAS*, 183, 341

Wiklind T., Henkel C., 1989, *A&A*, 225, 1

Wolfire M. G., McKee C. F., Hollenbach D., Tielens A. G. G. M., 2003, *ApJ*, 587, 278

Woo J.-H., Urry C. M., 2002, *ApJ*, 579, 530

Wrobel J. M., Kenney J. D. P., 1992, *ApJ*, 399, 94

Wu Q., 2009, *MNRAS*, 398, 1905

York D. G., et al., 2000, *AJ*, 120, 1579

Young J. S., Scoville N. Z., 1991, *ARAA*, 29, 581

Young L. M., Bureau M., Cappellari M., 2008, *ApJ*, 676, 317

Young L. M., et al., 2011, *MNRAS*, 414, 940

Zabel N., et al., 2019, *MNRAS*, 483, 2251

Zhao W., et al., 2018, *ApJ*, 854, 124

van Velzen S., Falcke H., Schellart P., Nierstenhöfer N., Kampert K.-H., 2012, *A&A*, 544, A18

van den Bosch R. C. E., 2016, *ApJ*, 831, 134

van den Bosch R. C. E., van de Ven G., 2009, *MNRAS*, 398, 1117